

IR spectral and structural changes caused by the conversion of acetanilide into azanion

E .A. Velcheva*, Z. I. Glavcheva, B.A. Stamboliyska

Department of Structural Organic Analysis, Institute of Organic Chemistry with Centre of Phytochemistry, Bulgarian Academy of Sciences, Acad. G. Bonchev St., Block 9, 1113 Sofia, Bulgaria

Received June 26, 2015, Revised September 10, 2015

The structures of acetanilide azanion and of its ^{15}N labelled analogue have been studied by means of both IR spectra and DFT calculation, employing the B3LYP functional and 6-311+G(2df,p) basis set. A good agreement has been found between the theoretical and experimental vibrational characteristic of the particles studied. The conversion of acetanilide molecule into the azanion causes 150 cm^{-1} decrease in the carbonyl stretching frequency, threefold increase in the integrated intensity of the corresponding IR band and other essential spectral changes. According to the calculations, the structural changes in the steric structure caused by this conversion take place *at* and *next* to the azanionic center. The new (azanionic) charge is distributed as follows: -0.304 e^- and -0.346 e^- are delocalized over the phenyl and acetyl groups and -0.349 e^- of its remained localized at the azanionic centre.

Keywords: N-phenylacetamide, anion, DFT

INTRODUCTION

The structure of organic anions is of general interest, as in living organisms part of bioactive molecules are dissociated in the body liquids, so that certain physiological actions are assumed to be due to its solvated anions. However, the highly reactive nature of anionic species has limited their structural characterization. The conversions of neutral molecule into radical-anions, carbanions, azanion, *etc.* are accompanied by essential changes in the vibration spectra. So, these changes are very informative for the structural variations caused by the same conversions [1]. The structure of large series of organic molecules and their anions have been successfully studied recently on the basis of experimental IR spectra combined with DFT computations [2-6]. The title compound is an interesting and convenient object of the molecule \rightarrow anion conversions investigations, as it contains the (-CO-NH-) characteristic group and can be easily converted into a stable azanion.

Acetanilide, (N-phenylacetamide) was the first analgesic and antipyretic synthetic drug and was introduced into medical practice under the name of Antifebrin by Cahn and Hepp in 1886 [7]. The discovery of acetanilide as effective therapeutic agent was leading to the development of many new drugs, structural analogues, with similar or different pharmacological properties [8]. In the body acetanilide is mostly converted to p-hydroxyacetanilide [9], which has replaced

acetanilide in therapy because it is less likely to induce blood disorders.

The early work on infrared (IR) spectra of acetanilide was reviewed by Crooks [10], Mann and Thompson [11], Abbott *et al.* [12]. A detailed empirical assignment of IR and Raman bands of acetanilide was reported about 50 years ago [13]. The complete IR band assignment of the acetanilide molecule was recently performed using ab initio Hartree-Fock (HF) [9] and DFT calculations [14,15]. The carbonyl C=O stretching frequencies and intensities of IR bands in series of substituted acetanilides were found to correlate with both Hammett's substituent constants and certain indices computed within ab initio and DFT methods [16-18]. IR spectra of a series of various carboxamide azanions were studied by Ognyanova and coworkers [19]. The authors reported that the stretching vibration frequencies of the amide C=O shifts downward depending on the substituents. Neither the detailed IR spectra nor structure of acetanilide azanion have been studied theoretically or experimentally. The purpose of the present investigation is to follow the spectral and structural changes, caused by the conversion of acetanilide molecule into the corresponding azanion on the basis of both DFT computations and spectroscopic experiments.

EXPERIMENTAL AND COMPUTATIONS

Acetanilide (Aldrich, 99%) was used without additional purification. We prepared acetanilide- ^{15}N from aniline- ^{15}N (VEB-Berlin-Chemie, 97.2% at. Enrichment) and acetic anhydride. The

* To whom all correspondence should be sent:
E-mail: ev@orgchm.bas.bg

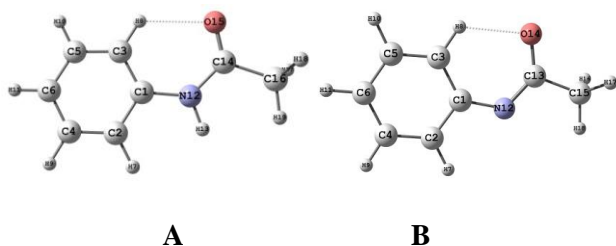
corresponding acetanilide azanion (counter ion Na^+) and its isotope-labeled derivative were prepared by adding dimethyl sulfoxide (DMSO/DMSO- d_6) solutions of acetanilide and acetanilide ^{-15}N to excess of dry sodium methoxide $-d_0$ and $-d_3$, and filtration of the reaction mixture by a syringe filter. The conversion of the parent isotopomeric compounds into azanions under these conditions (solvent, concentrations, counter ion) is practically complete: no bands of the parent compounds can be seen in the spectra after metalation. IR spectra were measured on Bruker Tensor 27 Fourier transform infrared (FTIR) spectrophotometer in a CaF_2 cell of 0.13 mm (0.10 – 0.15 mol l^{-1} DMSO/DMSO- d_6 solutions), at a resolution of 1 cm^{-1} and 64 scans.

The quantum chemical calculations were performed using the Gaussian 09 package [20]. The geometry optimizations of the structures investigated were done without symmetry restrictions, using density functional theory (DFT). We employed B3LYP hybrid functional, which combines Becke's three-parameter nonlocal exchange with the correlation functional of Lee and coworkers [21,22], adopting 6-311+G(2df,p) basis sets. The stationary points found on the molecular potential energy hypersurfaces were characterized using standard harmonic vibrational analysis. The theoretical vibrational spectra were interpreted by means of potential energy distributions (PEDs) using VEDA 4 program [23]. For a better correspondence between experimental and calculated values, we modified the results using the empirical scaling factors [24].

RESULTS AND DISCUSSIONS

Energy analysis

All conformers of acetanilides and its deprotonated form have determined from rotation about Ph-N and N-C bonds. The structures of the most stable conformers are shown in Scheme 1.



Scheme 1. B3LYP/6311+G(2df,p) optimized structures of the most stable conformers of acetanilide molecule A and its azanion B.

Both structures of molecule and azanion correspond to *trans*-type conformers (with respect to the phenyl and methyl groups). According to the B3LYP/6-311+G(2df,p) calculations the *cis* conformers of molecule are less stable than the *trans* form by 11.6 kJmol^{-1} . This result is with agreement with the theoretical study of Ilieva *at al.*[17]. The presence of the same conformer was also established by crystallographic analysis[25,26] and experimental and IR spectral data in solution [16]. According to the theoretical data, the *trans* conformer of the azanion is the more stable by the 21.6 kJmol^{-1} .

The calculated total energies of the studied species are as follow:

$$E_{\text{tot}} = -440.299988561\text{ H for the acetanilide}$$

$$E_{\text{tot}} = -439.7337264\text{ H for the acetanilide azanion}$$

The energy difference $\text{ED} = E(\text{anion}) - E(\text{molecule})$ can be used as an approximate measure of pK_a of a given compound in the gas phase [27]. Georgieva and Velcheva [28] have found that ED values of series of C-H, N-H and O-H acids correlate fairly well (correlation coefficient $R = 0.94$) with the corresponding pK_a values, measured in DMSO. Having in mind $\text{ED} = 1489.06\text{ H}$ and the correlation equation:

$\text{pK}_a(\text{DMSO}) = 0.11507\text{ED} - 150.04\text{ kJ mol}^{-1}$
we estimated a "theoretical" pK_a value of acetanilide at 21.0 in excellent agreement with the experimental value of 21.5 in DMSO [29].

Infrared spectra

Organic anions are not soluble in common spectroscopic solvents and usually react with them. So, polar aprotic solvents, most frequently DMSO, are used to study the IR spectra of organic anionic derivatives [2-6,30].

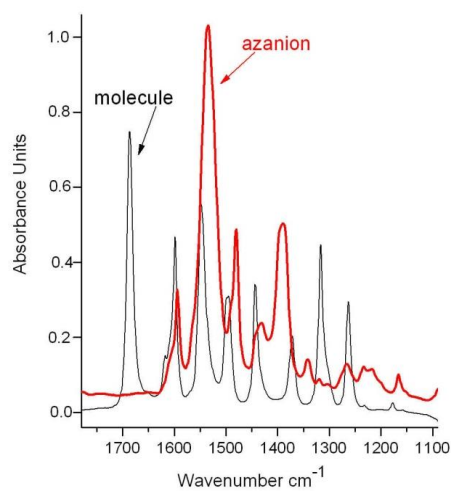


Fig. 1. IR spectra (0.12 mol l^{-1} in DMSO- d_6) of acetanilide molecule and its azanion.

Acetanilide azanion (e.g., acetanilide itself) is highly soluble and very stable in DMSO. To perform a correct comparison of the IR spectra of acetanilide isotopomers with those of their azanions, we shall consider their DMSO solution spectra. As in the preceding subsection, we shall now use theoretical data for the most stable conformers of the species studied. The fragment of the infrared spectrum of acetanilide in DMSO- d_6 solution is shown in Figure. 1.

The numerical values of the experimental IR data are compared with the theoretical ones in Table 1.

Fairly good agreement between the scaled theoretical and measured IR frequencies is observed. The mean deviation between them is 10 cm^{-1} . The largest differences between theoretical and experimental IR data correspond to the N-H stretching vibrations. They form a multiplet in the interval 3300 – 3080 cm^{-1} , because of the formation of strong hydrogen bonds mainly with DMSO solvent. The assignment of the experimental bands to the calculated normal modes in the C–H stretching region (3040–2800 cm^{-1}) is not obvious because there are fewer bands in the experimental spectrum than predicted by the calculations

Table 1. Theoretical (B3LYP/6-311+G(2df,p) and experimental (solvent DMSO- d_6) vibrational frequencies (cm^{-1}) and IR integrated intensities (A in $\text{km}\cdot\text{mol}^{-1}$) of acetanilide

| $\nu_{\text{calc.}}$ | $\nu_{\text{calc.}}^a$ | A_{calc} | Approximative description ^b | $\nu_{\text{exp.}}$ | $A_{\text{exp.}}$ |
|----------------------|------------------------|-------------------|--|---------------------|-------------------|
| 3622 | 3574 | 19.2 | 100 $\nu(\text{N-H})$ | 3301-3070 | |
| 3243 | 3200 | 5.5 | 99 $\nu(\text{Ph-H})$ | | |
| 3189 | 3147 | 15.1 | 91 $\nu(\text{Ph-H})$ | | |
| 3174 | 3133 | 20.1 | 86 $\nu(\text{Ph-H})$ | 3041 | 10.2 |
| 3165 | 3123 | 0.2 | 90 $\nu(\text{Ph-H})$ | | |
| 3146 | 3104 | 12.7 | 100 $\nu(\text{Ph-H})$ | 3010 | 14.1 |
| 3114 | 3072 | 3.6 | 100 $\nu^{\text{as}}(\text{CH}_3)$ | 2977 | 8.8 |
| 3113 | 3072 | 15.7 | 100 $\nu^{\text{as}}(\text{CH}_3)$ | 2934 | 10.5 |
| 3042 | 3002 | 9.5 | 100 $\nu^s(\text{CH}_3)$ | 2855 | 4.2 |
| 1750 | 1715 | 246.7 | 81 $\nu(\text{C=O})$ | 1686 | 127.5 |
| 1643 | 1610 | 43.6 | 53 $\nu^{\text{Ph}}(\text{CC})$, 10 $\delta^{\text{Ph}}(\text{CCH})$ | 1617 | 45.7 |
| 1634 | 1601 | 37.7 | 55 $\nu^{\text{Ph}}(\text{CC})$, 10 $\delta(\text{HNC})$ | 1599 | 34.3 |
| 1555 | 1524 | 292.3 | 42 $\delta(\text{HNC})$, 15 $\nu(\text{N-C})$, 10 $\delta^{\text{Ph}}(\text{CCH})$ | 1547 | 118.6 |
| 1531 | 1501 | 63.7 | 71 $\delta^{\text{Ph}}(\text{CCH})$ | 1495 | 51.3 |
| 1489 | 1460 | 12.5 | 95 $\delta(\text{CH}_3)$ | | |
| 1470 | 1441 | 7.2 | 93 $\delta(\text{CH}_3)$ | | |
| 1468 | 1439 | 125.0 | 58 $\nu(\text{Ph-H})$, 15 $\delta(\text{HNC})$ | 1443 | 50.1 |
| 1400 | 1372 | 34.8 | 88 $\delta(\text{CH}_3)$ | 1372 | 32.1 |
| 1360 | 1333 | 8.3 | 76 $\nu(\text{Ph-H})$ | | |
| 1338 | 1321 | 120.5 | 43 $\nu^{\text{Ph}}(\text{CC})$, 35 $\nu(\text{N-C})$ | 1317 | 60.2 |
| 1265 | 1249 | 92.7 | 17 $\delta(\text{HNC})$, 17 $\nu(\text{Ph-N})$ | 1263 | 35.9 |
| 1236 | 1219 | 37.0 | 18 $\nu(\text{C-CH}_3)$, 17 $\nu(\text{N-C})$, 15 $\nu(\text{Ph-N})$ | | |
| 1206 | 1182 | 19.5 | 90 $\nu(\text{Ph-H})$ | 1177 | 20.4 |
| 1185 | 1169 | 0.9 | 79 $\nu(\text{Ph-H})$ | | |
| 1114 | 1099 | 9.0 | 40 $\nu^{\text{Ph}}(\text{CC})$, 33 $\nu(\text{Ph-H})$ | | |
| 1054 | 1040 | 5.4 | 56 $\nu^{\text{Ph}}(\text{CC})$ | | |
| 1053 | 1039 | 5.8 | 95 $\delta(\text{CH}_3)$ | | |
| 1019 | 1006 | 9.1 | 77 $\delta^{\text{Ph}}(\text{CCC})$ | | |
| 1013 ^c | 1000 | 11.4 | 90 $\delta(\text{CH}_3)$ | | |

^aScaled by 0.985[24]. ^bVibrational modes: ν , stretching; δ , bendings. The numbers before the mode symbols indicate % contribution (10 or more) of a given mode to the corresponding normal vibration, according to the potential energy distribution. ^c Followed by 22 lower-frequency normal vibrations.

Table 2. Theoretical (B3LYP/6-311+G(2df,p) and experimental (solvent DMSO-d₆) vibrational frequencies (cm⁻¹) and IR integrated intensities (a in km mol⁻¹) of acetanilide anion.

| $\nu_{\text{calc.}}$ | $\nu_{\text{calc.}}^{\text{a}}$ | A_{calc} | Approximative description ^b | $\nu_{\text{exp.}}$ | $A_{\text{exp.}}$ |
|----------------------|---------------------------------|-------------------|---|---------------------|-------------------|
| 3221 | 3175 | 4 | 99 $\nu(\text{Ph-H})$ | | |
| 3159 | 3114 | 35 | 100 $\nu(\text{Ph-H})$ | | |
| 3149 | 3104 | 73 | 99 $\nu(\text{Ph-H})$ | 3048 | 18.1 |
| 3119 | 3074 | 53 | 99 $\nu(\text{Ph-H})$ | 3008 | 16.2 |
| 3111 | 3067 | 17 | 99 $\nu(\text{Ph-H})$ | | |
| 3101 | 3057 | 36 | 89 $\nu^{\text{as}}(\text{CH}_3)$ | | |
| 3055 | 3012 | 42 | 100 $\nu^{\text{as}}(\text{CH}_3)$ | 2960 | 17.3 |
| 3008 | 2965 | 80 | 100 $\nu^{\text{s}}(\text{CH}_3)$ | 2915 | 14.5 |
| 1628 | 1603 | 63 | 59 $\nu^{\text{Ph}}(\text{CC})$, 22 $\delta^{\text{Ph}}(\text{CCH})$ | 1594 | 49.1 |
| 1576 | 1552 | 16 | 61 $\nu^{\text{Ph}}(\text{CC})$, 15 $\delta^{\text{Ph}}(\text{CCH})$, 13 $\delta^{\text{Ph}}(\text{CCC})$ | | |
| 1570 | 1545 | 815 | 67 $\nu(\text{C=O})$, 16 $\nu(\text{N-C})$ | 1533 | 388.2 |
| 1508 | 1485 | 212 | 63 $\delta^{\text{Ph}}(\text{CCH})$, 10 $\nu(\text{Ph-N})$ | 1480 | 99.3 |
| 1478 | 1455 | 4 | 88 $\delta(\text{CH}_3)$ | | |
| 1472 | 1449 | 1 | 44 $\delta^{\text{Ph}}(\text{CCH})$, 21 $\nu^{\text{Ph}}(\text{CC})$ | | |
| 1465 | 1443 | 30 | 67 $\delta(\text{CH}_3)$ | 1430 | 51.6 |
| 1398 | 1378 | 696 | 36 $\nu(\text{N-C})$, 23 $\nu(\text{Ph-N})$ | 1385 | 219.7 |
| 1354 | 1335 | 1 | 92 $\delta(\text{CH}_3)$ | 1339 | 37.8 |
| 1339 | 1320 | 57 | 50 $\delta^{\text{Ph}}(\text{CCH})$, 11 $\nu^{\text{Ph}}(\text{CC})$ | | |
| 1299 | 1280 | 59 | 54 $\nu^{\text{Ph}}(\text{CC})$, 10 $\delta^{\text{Ph}}(\text{CCH})$ | 1266 | 30.5 |
| 1238 | 1220 | 3 | 26 $\nu(\text{Ph-N})$, 16 $\nu(\text{N-C})$ | 1216 | 32.7 |
| 1176 | 1159 | 36 | 60 $\delta^{\text{Ph}}(\text{CCH})$ | 1165 | 19.1 |
| 1165 | 1148 | 3 | 78 $\delta^{\text{Ph}}(\text{CCH})$ | 1129 | 2.2 |
| 1087 | 1072 | 9 | 50 $\delta^{\text{Ph}}(\text{CCH})$, 23 $\nu^{\text{Ph}}(\text{CC})$ | | |
| 1048 ^c | 1033 | 1 | 92 $\delta(\text{CH}_3)$, $\delta(\text{OCN})$ | | |

^aScaled by 0.9858 [24]. ^bVibrational modes: ν , stretching; δ , bendings. The numbers before the mode symbols indicate % contribution (10 or more) of a given mode to the corresponding normal vibration, according to the potential energy distribution matrix. ^c Followed by 24 lower-frequency normal vibrations.

The highest frequency experimental bands observed in the IR spectrum (3040–3000 cm⁻¹) are assigned to the aromatic C-H stretches, while the lower frequency bands are attributed to the methyl group motions. The $\nu(\text{C-H})$ bands are of low intensity in both the experimental and theoretical spectra.

DFT calculations reproduce well the IR frequencies measured in DMSO of the Amide-I, Amide-II, Amide-III vibrations. The Amide-I mode ($\nu(\text{CO})$) is predicted to appear at 1715 cm⁻¹ as a very intense band. Experimentally, a very strong band was detected at 1686 cm⁻¹ in DMSO. In KBr pellet this band is downshifted strongly to 1665 cm⁻¹ due to intermolecular hydrogen N–H...C=O bonding in the crystal [14]. The strong IR band observed at 1544 cm⁻¹ was identified as Amide-II (the scissoring deformation $\delta(\text{HNC})$) in accordance with its scaled theoretical value of 1524 cm⁻¹. The stretching $\nu(\text{N-C})$ strongly coupled with CC,

denoted as Amide-III was predicted as a high intensity band at 1321 cm⁻¹ and measured at 1317 cm⁻¹ in the experimental spectra. The theoretical and experimental IR data for the acetanilide azanion are compared in Table 2.

As above we can find there a good agreement between experimental and scaled theoretical frequencies. The mean deviation between them is 9.1 cm⁻¹ within the corresponding interval of 9–25 cm⁻¹, typical for DFT calculations of frequencies for series of anions [2-6]. The frequency isotopic shifts, resulting from the ¹⁵N substitution, are also well reproduced (Table 3).

The conversion of acetanilide into the azanion results in very essential changes in the IR spectrum (Tables 1 and 2; Figure 1), *e.g.*:

- Essential decrease in the carbonyl stretching frequency $\nu(\text{CO})$. There is no longer carbonyl band at the usual place. Its frequency decreases by: predicted 170 cm⁻¹, measured

153 cm⁻¹. The appearance of $\nu(\text{CO})$ bands of acetanilide azanion at 1533 cm⁻¹ corroborated the assignment reported by Ognyanova and coworkers [19] and agree qualitatively with assigned of the very strong band at 1549 cm⁻¹ in IR spectrum of paracetamol dianion [30]. Incorrectly Liu *et al.* [31] assumed that the band at 1594 cm⁻¹ in the IR spectrum of the complex containing deprotonated acetanilide ligand originates from $\nu_{\text{C=O}}$ in analogy to the spectrum of the acetanilides. A -8 cm⁻¹ ¹⁵N isotopic shift has been measured in DMSO for this band; the theory gives a -2 cm⁻¹ value of the same shifts.

- Essential increase in the integrated intensity of the carbonyl band A_{CO} : predicted 3.3fold, measured 3 fold.

- Increase in C-N stretching frequency $\nu(\text{C-N})$: predicted 57 cm⁻¹, measured 68 cm⁻¹. The shift of this the coordinate to higher frequency is obviously due to the significant shortening of the C-N bond, caused by the conversion of the acetanilide molecule into the azanion.

- Essential increase in the corresponding intensity $A_{\text{C-N}}$: predicted 5.8fold, measured 3.6 fold.

- Strong enhancement of the intensity of the aromatic skeletal bands of the phenylene ring 19 (Wilson's notation): predicted 3.3-fold, measured 2-fold.

Table 4. Theoretical (B3LYP/6-311+G(2df,p)) and experimental bond lengths R (Å) and bond angles A (°) in the acetanilide molecule and its azanion.

| | Molecule | | Δ^b | Anion | |
|---|---------------------------|-------------|------------|-------------|------------|
| | Experimental ^a | Theoretical | | Theoretical | Δ^c |
| <i>Bond lengths</i> | | | | | |
| R(C ¹ ,C ²) | 1.394 | 1.397 | 0.003 | 1.421 | 0.024 |
| R(C ² ,C ³) | 1.385 | 1.390 | 0.005 | 1.390 | 0.000 |
| R(C ³ ,C ⁴) | 1.383 | 1.389 | 0.006 | 1.393 | 0.004 |
| R(C ⁴ ,C ⁵) | 1.390 | 1.390 | 0.000 | 1.396 | 0.006 |
| R(C ⁵ ,C ⁶) | 1.378 | 1.385 | 0.007 | 1.384 | -0.001 |
| R(C ¹ ,N ¹²) | 1.409 | 1.409 | 0.000 | 1.376 | -0.033 |
| R(N ¹² ,C ¹⁴) | 1.348 | 1.374 | 0.026 | 1.338 | -0.036 |
| R(C ¹⁴ ,O ¹⁵) | 1.222 | 1.216 | -0.006 | 1.252 | 0.036 |
| R(C ¹⁴ ,C ¹⁶) | 1.505 | 1.516 | 0.011 | 1.534 | 0.018 |
| <i>Bond angles</i> | | | | | |
| A(C ¹ ,C ² ,C ³) | 119.6 | 119.3 | -0.3 | 121.1 | 1.7 |
| A(C ⁴ ,C ³ ,C ²) | 121.2 | 121.4 | 0.2 | 121.8 | 0.5 |
| A(C ⁵ ,C ⁴ ,C ³) | 120.4 | 119.1 | -1.3 | 118.1 | -1.0 |
| A(C ⁶ ,C ⁵ ,C ⁴) | 120.5 | 120.2 | -0.3 | 120.7 | 0.5 |
| A(N ¹² ,C ¹ ,C ⁶) | 116.9 | 117.1 | 0.2 | 116.3 | -0.9 |
| A(C ¹⁴ ,N ¹² ,C ¹) | 127.5 | 129.5 | 2.0 | 122.6 | -6.9 |
| A(N ¹² ,C ¹⁴ ,O ¹⁵) | 123.3 | 124.0 | 0.7 | 130.2 | 6.2 |
| A(C ¹⁶ ,C ¹⁴ ,N ¹²) | 115.5 | 114.6 | -0.9 | 113.4 | -1.3 |

^aSee Ref. [26]. ^bAlgebraic deviations (Å, degrees) between experimental and theoretical values. ^cAlgebraic deviations (Å, degrees) between theoretical values of the anion and molecule.

Table 3. Theoretical (B3LYP/6-311+G(2df,p)) end experimental (in DMSO) vibrational frequencies (cm⁻¹) of acetanilide azanion-¹⁵N and corresponding isotopic shifts.

| Azanion | | Azanion- ¹⁵ N | | $\Delta_{\text{calc.}}$ | $\Delta_{\text{exp.}}$ |
|----------------------|---------------------|--------------------------|---------------------|-------------------------|------------------------|
| $\nu_{\text{calc.}}$ | $\nu_{\text{exp.}}$ | $\nu_{\text{calc.}}$ | $\nu_{\text{exp.}}$ | | |
| 1603 | 1594 | 1602 | 1592 | -1 | -2 |
| 1552 | | 1552 | | 0 | |
| 1545 | 1533 | 1543 | 1525 | -2 | -8 |
| 1485 | 1480 | 1484 | 1478 | -1 | -2 |
| 1455 | | 1455 | | 0 | |
| 1449 | | 1449 | | 0 | |
| 1443 | 1430 | 1442 | 1430 | 0 | 0 |
| 1378 | 1385 | 1362 | 1373 | -16 | -12 |
| 1335 | 1339 | 1332 | 1334 | -2 | -5 |

Structural analysis of the species studied

According to X-ray diffraction experimental data the dihedral angle between the phenyl ring and amide group planes in the monoclinic crystal of acetanilide is 43.4° [26]. According to the calculations in the most stable conformers of the isolated molecule these groups are planar. The same groups in the isolated azanion have been predicted to be again planar. The theoretical and experimental bond lengths and angles in the acetanilide and its azanion are listed in Table 4.

As seen, there is a good agreement between the experimental and the theoretical values. The largest deviation from 0.026 Å is in bond N¹²-C¹⁴ and can be associated with the formation of hydrogen bonds in the solid state. The mean absolute deviations (m.a.d.) between theoretical and experimental bond lengths and angles of acetanilide molecule are 0.006 Å and 0.07, respectively. This result leads us to believe that the theoretical bonds lengths and angle for the acetanilide anion are also reliable. The most significant changes caused by the conversion molecule azanion take place both at the azanionic center and next to it, with agrees the data for other azanions [2,4]. They are strong shortening of the Ph-N and N-C and bonds, strong lengthening of the C=O and C-CH₃ bonds.

The net electronic charges q of the fragments of the species studied are as follows:

| | C ₆ H ₅ | NH/N ⁻ | COCH ₃ |
|---------------------|-------------------------------|-------------------|-------------------|
| q in the molecule | 0.098 | 0.012 | -0.110 |
| q in the azanion | -0.206 | -0.339 | -0.455 |

The charge change values $\Delta q_i = q_i(\text{anion}) - q_i(\text{molecule})$ are usually quite informative in showing the distributions of the new charges in anions [2-4,30]. According to the present calculations, the new (azanionic) charge is distributed as follows: -0.304 e⁻ and -0.346 e⁻ are delocalized over the phenyl and acetyl groups and -0.349 e⁻ of its remained localized at the azanionic centre.

CONCLUSION

The spectral and structural changes, caused by the conversion of the acetanilide molecule into the corresponding azanion have been studied by IR spectra DFT method at B3LYP/6-311+G(2df,p) level.

A comparison of calculated with measured infrared data can be used as a test for the reliability of the structural predictions for various molecules and anions of this and similar types. These predictions can be very useful in cases of molecules and ions for which experimental structural parameters are inaccessible or unknown. IR spectral changes, which take place as a result of the conversion of molecule into azanion, were adequate predicted by same theoretical method.

Acknowledgements: Financial support of National Science Fund, Bulgaria (RNF01/0110) is gratefully acknowledged.

REFERENCES

1. I. N. Juchnovski, I. G. Binev, in: S. Patai, Z. Rappoport (Ed.): The chemistry of functional groups, Suppl. C., Wiley, New York, 1983, p. 107.
2. A. D. Popova, E. A. Velcheva, B. A. Stamboliyska, *J. Mol. Struct.*, **1009**, 23 (2012).
3. E. A. Velcheva, B. A. Stamboliyska, P. J. Boyadjieva, *J. Mol. Struct.*, **963**, 57 (2010).
4. A. D. Popova, M. K. Georgieva, O. I. Petrov, K. V. Petrova, E. A. Velcheva, *Int. J. Quant. Chem.*, **107**, 1752 (2007).
5. S. Stoyanov, J. A. Tsenov, D. Y. Yancheva, *J. Mol. Struct.*, **1009**, 42 (2012).
6. S. Stoyanov, *J. Phys. Chem.*, **114**, 5149 (2010).
7. A. Cahn, P. Hepp, *Centralbl. Klein. Med.*, **7**, 561 (1886).
8. The Merck Index, 8th ed. Rahway, NY, Merck & Co., Inc., 1968, electronic version, 1998.
9. B. B. Brodie, A. E. Axelrod, *J. Pharmacol. Exp. Ther.*, **94**, 22 (1948).
10. D. A. Crooks, *Nature, Lond. A*, **160**, 17 (1947).
11. J. Mann, H. W. Thompson, *Proc. Royal Soc. Lond. A*, **192**, 489 (1948).
12. N. B. Abbott, A. Elliott, *Proc. Royal Soc. Lond. A*, **234**, 247 (1956).
13. V. V. Chalapathi, K. V. Ramiah, *Proc. Indian Acad. Sci. Sec A*, **67**, 184 (1968).
14. J. Binoy, N. B. Prathima, C. M. Krishna, C. Santhosh, I. H. Joe, V. S. Jayakumar, *Laser Phys.*, **16**, 1253 (2006).
15. H. Q. Liang, Y. P. Tao, L. G. Han, Y. X. Han, Y. J. Mo, *Guang Pu Xue Yu Guang Pu Fen Xi*, **32**, 2706 (2012).
16. S. Ilieva, B. Hadjieva, B. Galabov, *J. Mol. Struct.*, **508**, 73 (1999).
17. S. Ilieva, B. Hadjieva, B. Galabov, *J. Org. Chem.*, **67**, 6210 (2002).
18. D. Cheshmedzhieva, V. Dimitrova, B. Hadjieva, S. Ilieva, *J. Mol. Struct.*, **1009**, 69 (2012).
19. V. Ognyanova, J. Petrov, G. N. Andreev, *Spectrosc. Lett.*, **30**, 933 (1997).
20. M. J. Frisch, G. W. Trucks, H. B. Schlegel, G. E. Scuseria, M. A. Robb, J. R. Cheeseman, G. Scalmani, V. Barone, B. Mennucci, G. A. Petersson, H. Nakatsuji, M. Caricato, X. Li, H. P. Hratchian, A. F. Izmaylov, J. Bloino, G. Zheng, J. L. Sonnenberg, M. Hada, M. Ehara, K. Toyota, R. Fukuda, J. Hasegawa, M. Ishida, T. Nakajima, Y. Honda, O. Kitao, H. Nakai, T. Vreven, J. A. Montgomery, Jr., J. E. Peralta, F. Ogliaro, M. Bearpark, J. J. Heyd, E. Brothers, K. N. Kudin, V. N. Staroverov, R. Kobayashi, J. Normand, K. Raghavachari, A. Rendell, J. C. Burant, S. S. Iyengar, J. Tomasi, M. Cossi, N. Rega, J. M. Millam, M. Klene, J. E. Knox, J. B. Cross, V. Bakken, C. Adamo, J. Jaramillo, R. Gomperts, R. E. Stratmann, O. Yazyev, A. J. Austin, R. Cammi, C. Pomelli, J. W. Ochterski, R. L. Martin, K. Morokuma, V. G. Zakrzewski, G. A. Voth, P. Salvador, J. J. Dannenberg, S. Dapprich, A. D. Daniels, Ö. Farkas, J. B. Foresman, J. V. Ortiz, J. Cioslowski, D. J. Fox,

- Gaussian 09, Revision A1, Gaussian Inc., Wallingford CT, 2009.
21. A. D. Becke, *J. Chem. Phys.*, **98**, 5648 (1993).
22. C. Lee, W. Yang, G. R. Parr, *Phys. Rev.*, **B37**, 785 (1998).
23. M. H. Jamroz, *Vibrational Energy Distribution Analysis VEDA 4*, Warsaw, 2004-2010.
24. J. P. Merrick, D. Moran, L. Radom, *J. Phys. Chem.*, **A111**, 11683 (2007).
25. C. J. Brown, *Acta Crystallogr.*, **21**, 442 (1966).
26. H. J. Wasserman, R. R. Ryan, S. P. Layne, *Acta Crystallogr.*, **C41**, 783 (1985).
27. V. M. Vlasov, L. A. Oshkina, *Org. React.*, **28**, 47 (1993).
28. M. K. Georgieva, E. A. Velcheva, *Int. J. Quantum. Chem.*, **106**, 1316 (2006).
29. F. G. Bordwell, G. Z. J. Ji, *Am. Chem. Soc.*, **113**, 8398 (1991).
30. I. G. Binev, P. J. Boyadjieva, Y. I. Binev, *J. Mol. Struct.*, **447**, 235 (1998).
31. X. Liu, S. Zhang, Y. Ding, *J. Mol. Struct.*, **1018**, 185 (2012).

ИЧ СПЕКТРАЛНИ И СТРУКТУРНИ ПРОМЕНИ ПРИЧИНЕНИ ОТ ПРЕВРЪЩАНЕТО НА АЦЕТАНИЛИДА В АЗАНИОН

Е. А. Велчева*, З. И. Главчева, Б. А. Стамболийска

Лаборатория „Структурен органичен анализ”, Институт по органична химия с център по фитохимия, Българска академия на науките, ул. „Акад. Г. Бончев”, бл.9, 113 София

Постъпила на 26 юни 2015 г., Преработена на 10 септември 2015 г.

Структурите на азаниона на ацетанилида и на неговия ^{15}N белязан аналог са изследвани с помощта на ИЧ спектри и ТФП изчисления, използвайки V3LYP функционал и 6-311+G(2df,p) базисен набор. Намерено е добро съответствие между теоретичните и експерименталните вибрационни характеристики на изследваните частици. Превръщането на молекулата ацетанилид в азанион предизвиква 150 cm^{-1} понижение на карбонилната валентна честота, трикратно увеличение на интегралната интензивност на съответната ИЧ ивица и други съществени спектрални промени. Според изчисленията, структурните промени в пространствената структура, причинени от това превръщане, са *при* и *непосредствено до* азанионния център. Новият (азанионен) заряд се разпределя както следва: -0.304 e^- и -0.346 e^- са делокализирани върху фенилната и ацетилната групи и 0.349 e^- от него остават локализирани при азанионния център.

Kinetics of laser-induced photodissociation of oxyhemoglobin and its biomedical applications

A.I. Gisbrecht^{1*}, M.M. Asimov²

¹*Institute of Electronics, Bulgarian Academy of Sciences,
72 Tzarigradsko Chaussee Blvd., Sofia, Bulgaria*

²*Institute of Physics, National Academy of Sciences of Belarus,
68 Nezavisimost Ave., Minsk, Belarus*

Submitted September 9, 2015; Revised October 6, 2015

In this study we investigate the kinetics of oxygen tension (pO_2) in skin tissue under the influence of the transcutaneous laser irradiation. The results of *in vivo* experimental measurements of pO_2 by a method of transcutaneous oxygen monitoring (TcOM) are presented. The results show that under laser irradiation the value of tissue oxygenation increases and after approximately 10 minutes of exposure exceeds its initial level up to 1.6 times. The observed increase in pO_2 indicates the process of photodissociation of oxyhemoglobin (HbO_2) in skin blood vessels, which results in local O_2 increase in the tissue. Such laser-induced enrichment of tissue oxygenation can be used in phototherapy of pathologies, where the elimination of local tissue hypoxia is critical.

Keywords: oxyhemoglobin photo-dissociation; tissue oxygenation; oxygen tension.

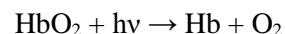
INTRODUCTION

Tissue oxygenation plays a key role in the cell metabolism, energy supply and life activity of an organism. Many diseases such as diabetes, burns, bedsores and wounds are accompanied with an insufficient supply of oxygen to the tissues [1,2]. Also, the deficit of oxygen in cancer tissue is a major problem limiting the efficiency of photodynamic therapy [3,4]. The wound healing process directly depends on the oxygen pressure in skin tissue (Tc PO_2). For example, the additional supply of oxygen leads to an increase in the rate of collagen synthesis and an improvement of the protective functions of the skin. It is currently accepted that the adequate tissue oxygen concentration for normal cell metabolism should exceed 40 mmHg. Injuries, infections, and diseases can reduce this vital tissue oxygen level down to almost zero, which indicates tissue hypoxia. Optimal tissue healing occurs when the pO_2 rises to between 50 and 80 mmHg. Consequently, the value of pO_2 is an objective indicator for evaluating the local state of the tissue and the efficiency of cell metabolism. Controlling this mechanism provides the possibility for biological stimulation with a therapeutic effect.

In clinical practice the commonly used method for elimination of tissue hypoxia is ventilation of the lungs by pure O_2 at normal and hyperbaric pressure. Sustained periods at such pO_2 levels can

only be realized through the use of hyperbaric oxygen therapy [5], but it leads to the risk of oxygen intoxication. Moreover, this approach has not had a broad clinic application for local treatment due to technical difficulties. Thus the problem of local hypoxia elimination in biological tissues remains significant and the methods of influencing the delivery of oxygen to the tissue are of considerable interest. One of these methods is the light radiation in the optical spectral range.

A new approach for the optically induced increase in the local oxygen concentration due to photodissociation of oxyhemoglobin in cutaneous blood vessels has been proposed in [6]. The absorption of light by blood HbO_2 is connected with the following photochemical and photophysical processes. It is known [7] that absorption of a photon with the activation energy leads to the dissociation of a part of the molecules, resulting in the release of molecular oxygen and the formation of deoxyhemoglobin. Photodissociation is one of the simplest chemical reactions when a compound dissociates under the action of radiation.



The quantum efficiency of the photodissociation of oxyhemoglobin is high and reaches 10 % in a wide visible spectral range [7].

The photophysical process is connected with the non-radiative dissipation of the absorbed excitation energy, as the heat generated in this process is transferred to the blood capillaries with a characteristic thermal relaxation time of ~ 0.05 -1.2 msec. Estimates show that in the typical case a local increase in temperature of only 0.1 - 0.5 °C

* To whom all correspondence should be sent:
E-mail: aigiz@abv.bg

may be expected [8]. Such a small rise in the local temperature may produce little improvement in the capillary microcirculation of the blood and can hardly stimulate the cell metabolism [9].

We suppose that in the case of low energy irradiation the most important process is the photodissociation of HbO₂. Experimental proof of the suggested concept has been demonstrated in [10,11]. The observed local decrease in the level of arterial blood saturation during laser irradiation clearly proves the induced photodissociation of HbO₂ in blood capillary vessels. The efficiency of this process depends on the wavelength and the output power of the laser radiation, the blood vessels density in the irradiation area, the optical properties of the skin and the depth of the blood vessels in the tissue.

It is interesting but still unclear what fraction of O₂ molecules released by photodissociation can escape from the heme pocket and diffuse through the cell membranes and capillary walls, thereby increasing the tissue oxygen pressure. However, relevant studies mainly refer to *in vitro* experiments or studies of individual cases [12-15]. No investigations have been carried out as yet into whether an immediate improvement in the oxygen saturation occurs *in vivo*, which would be a key to wound healing.

In this paper, we present an experimental study *in vivo* of the pO₂ rate in skin under the influence of local transcutaneous He-Ne laser (628 nm) irradiation.

METHODS

The transcutaneous oximeter method, based on the principle of measuring the oxygen tension pO₂ in arterial blood, is a method for direct registration of gases that dissolve in the blood plasma. The choice of this method is determined by the fact that the TcOM allows the direct determination of the oxygen pressure in the skin tissue, in units of mmHg. Measurements were carried out using a transcutaneous oxygen monitor "Radiometer" TCM-4 with a Clark-type polarographic sensor with a diameter of 2.5 mm (TcPO₂ electrode) that consists of a platinum cathode and silver anode, electrolyte and an oxygen permeable membrane; a heating section and an electronic system for measuring and controlling the sensor temperature. (Fig.1 a).

The measurements were carried out on three volunteers, in the conditions of an absence of physical and emotional stress, in a seated position and at room temperature. All the procedures performed in the study were in accordance with the

ethical standards. Human studies in the article were approved by the relevant Institutional Review Board. During an individual measurement, all conditions were identical for all the subjects and remained constant throughout the measurement.

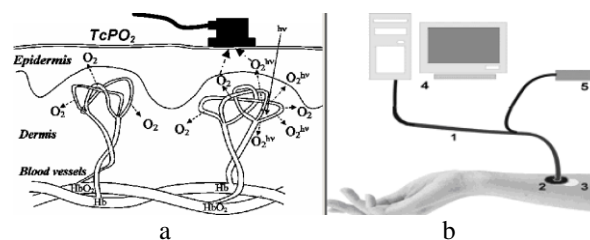


Fig. 1. Model of oxygen diffusion in tissue (a) and measurement (b) of tissue oxygen tensions: 1 - Clark sensor, 2 - electrolytic cell, 3 - irradiating zone, 4 - monitor TCM, 5 - He-Ne laser.

The measurement procedure is as follows. The sensor is placed on the skin of the forearm, an area with high capillary pressure then it is heated to 43°C (Fig. 1 b). Under the influence of temperature, oxygen diffuses from the capillaries into the epidermis and then into the electrolytic cell, where it is measured. The value of oxygen tension, measured transcutaneously (TcPO₂), corresponds to the value of pO₂ measured in the arterial blood plasma. The errors in the determination of TcPO₂ come from the skin thickness, the subcutaneous blood flow and the physiological factors influencing O₂ delivery to the skin surface (decrease in the blood flow, the arterial blood pressure, the vasoconstriction occurrence). Since oxygenation depends on a number of factors, the laser radiation was only used once and the measurements were carried out immediately, in order to obtain direct observation of the effect of radiation.

RESULTS

For local irradiation of cutaneous blood vessels, a He-Ne (632,8 nm) laser was chosen. As shown in the model calculations of the absorption spectra at the tissue depth [6], this wavelength lies in the effective absorption band of HbO₂ and penetrates deep into the skin issue. The laser output is 1 mW, and the beam diameter – 2,5 mm, providing a laser power density of ~ 20 mW/cm². First, after thermostabilization, the initial oxygen pressure in the tissue is measured, then the laser radiation is applied. In Fig.2 the measured values of pO₂ in dependence on the irradiation time are presented. The obtained results are normalized to the initial oxygen pressure value.

As can be seen, the tissue oxygen tension increases for all three patients (although with different rates) and reaches saturation levels after

approximately 10 minutes of exposure. The value of $TcPO_2$ in the irradiation zone depends on the time of exposure and the properties of the tissue that differ considerably for all three cases. It is significant to note that this growth of $TcPO_2$ is due to the additional O_2 in the tissue as a result of the laser-induced photodissociation of HbO_2 . The oxygen released from HbO_2 first increases the pO_2 in the blood plasma and then diffuses into the surrounding tissue. The value of the $TcPO_2$ measured transcutaneously increases about 1.6 times compared with its initial value. Generally, the diffusion occurs in three directions: toward the skin surface, inward to the muscle tissues and some is carried away by the blood flow. If we assume that the same amount of oxygen is carried away in all these directions, we should expect an increase in pO_2 in the arterial blood plasma by about a factor of 4.8.

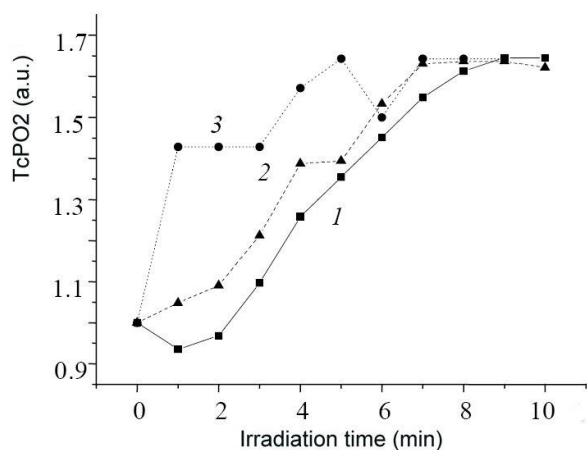


Fig. 2. Kinetics of laser-induced tissue oxygenation.

It is interesting to note that the obtained value of pO_2 realized by laser-induced photodissociation of HbO_2 is comparable with the one typically reachable by the conventional method of hyperbaric oxygen therapy [5].

DISCUSSION

In contrast to other (in vitro) studies, this study was carried out under in vivo conditions, so it is possible to make statements about the feasibility of the measurement effect.

Thus, we demonstrate that after prolonged irradiation (several minutes), a certain fraction of oxygen molecules released due to photodissociation of HbO_2 diffuses in the surrounding tissue and increases the oxygen partial pressure. Since the values of oxygenation depend on a number of factors, the results of this study cannot identify any immediate effect of the radiation on the oxygenation in tissue in vivo. Thus, it would be reasonable if further studies on the immediate

effects on oxygen saturation would take into account additional parameters, such as a variation in the wavelength radiation. The results obtained should correlate with the characteristics of light propagation in blood-filled tissues. The visible light in the blue and green spectral range has a small penetration depth into skin tissue, because of their proximity to the absorption bands of some basic skin chromophores such as HbO_2 and melanin. Red and especially near infrared radiation penetrates much deeper into the soft tissues and plays a dominant role in the absorption of laser radiation by oxyhemoglobin in the deeper layers of tissue blood vessels. Such possibility to increase the free oxygen content in tissues can be applied in clinical practice for treatment of a number of diseases related to problems with the microcirculation and oxygen supply and therefore requires further investigations.

It is very important to note that photodissociation of HbO_2 produces only molecular oxygen as a by-product and not singlet oxygen. Lepeshkevich in [16] uses time-resolved luminescence spectroscopy in the near-infrared region and does not measure detectable quantities of singlet oxygen during the photodissociation of O_2 from myoglobin and hemoglobin.

CONCLUSION

The obtained results demonstrate that the laser-induced photodissociation of oxyhemoglobin, whose main biological function is the transport of molecular oxygen, gives the possibility for an additional oxygen supply and allows the development of optical methods for tissue hypoxia elimination. Monitoring the kinetics of tissue oxygenation gives the possibility to control the normal aerobic cell metabolism.

It is shown that the efficiency of laser-induced oxygenation is comparable with the method of hyperbaric oxygenation, at the same time providing advantages by the local action. Advances in technology can lead to further improvement in the management of patients with wounds.

Acknowledgement: This work is partially supported by the project DFNI B02/9 /2014 of the Bulgarian Science Fund.

REFERENCES

1. D. Leaper, *Int. Wound. J.*, **3**, 4 (2007).
2. H.W.Hopf, M.D.Rollins, *Antioxidants and redox signaling*, **9**, 1183 (2007).
3. H. Lui, R. R. Anderson, *Dermatol. Clin.*, **11**, 1 (1993).
4. H. I. Pass, *J Natl. Cancer Inst.*, **85**, 443 (1993).

5. P. M. Tibbles, J. S. Edelsberg, *N. Engl. J. Med.*, **334**, 1642 (1996).
6. M. M. Asimov, R. M. Asimov, A.N. Rubinov, *J. Appl. Spectrosc.*, **65**, 877 (1998).
7. W. Saffran, Q. Gibson, *J. Biol. Chem.*, **252**, 7955 (1977).
8. J. R. Basford, *Lasers Surg. Med.*, **9**, 1 (1989).
9. D.A. Rogatkin, A.V. Dunaev, *Journal of Medical Research and Development*, **3**, 100 (2014).
10. M. Asimov, R. Asimov, M. Mirshahi, A. Gisbrecht, *Proc. SPIE.*, **4397**, 390 (2001).
11. I. Yabushita, T. Kobayashi, *Spectroscopy*, **24**, 333 (2010).
12. P. Liu, Z. Zhu, *J. Biomed. Optics*, **17**, 125002 (2012).
13. F. Heu, C. Forster, B. Namer, A. Dragu, *Laser Ther.*, **22**, 21 (2013).
14. H. Matsuo, Y. Morimoto, T. Arai, R. Wada, *Lasers Med. Sci.*, **15**, 181 (2000).
15. A. Stratonnikov, N. Ermishova, V. Loshchenov, *Quantum. Electron.*, **32**, 917 (2002).
16. S. Lepeshkevich, A. Stasheuski, *J. Photochem. Photobiol. B.*, **120**, 130 (2013).

КИНЕТИКА НА ЛАЗЕРНО-ИНДУЦИРАНАТА ФОТОДИСОЦИАЦИЯ НА ОКСИХЕМОГЛОБИНА В КРЪВТА ЗА БИОМЕДИЦИНСКИ ПРИЛОЖЕНИЯ

А.И. Гизбрехт¹, М.М. Асимов²

¹Институт по електроника, БАН, София, бул. Цариградско шосе 72.

²Физически Институт на Академия на науките на Беларус.

Постъпила на 9 септември 2015 г., коригирана на 6 октомври 2015 г.

(Резюме)

В тази статия ние изследваме кинетиката на напрежение на кислорода (pO_2) в кожната тъкан под въздействието на транскутанно лазерно облъчване. Експериментални измервания на оксигенацията са направени с помощта на метода на полярографски презкожен мониторинг на кислорода (ТсОМ). Резултатите показват, че при облъчване с He-Ne лазер (632 nm) степента на тъканната оксигенация се увеличава в зависимост от продължителността на облъчването и след около 10 минути достига стационарно ниво, като максималното измерено увеличение е 1,6 пъти. Трябва да отбележим, че кинетиката на растежа на PO_2 е пряко обусловена от допълнителното освобождаване на O_2 в тъканта като резултат на лазерно-индуцираната фотодисоциация на HbO_2 в кръвоносните съдове на кожата, което води до локално увеличаване на O_2 в тъканта. Това лазерно-индуцирано обогатяване на тъканите с кислород може да се използва в фототерапия на патологии, в зони с нарушена микроциркулация на кръв и тъкани в състояние на хипоксия, например в тумори, изгаряния, рани и язви.

Determination of trace amounts of manganese in water samples by flame atomic absorption spectrometry after dispersive liquid-liquid microextraction

A. Mirabi^{1*}, M. R. Jamali², Q. Kazemi¹

¹Department of Chemistry, Qaemshahr Branch, Islamic Azad University, Qaemshahr, Iran

² Department of Chemistry, Payam Noor University, Behshahr, Iran

Received April 20, 2015, Revised December 28, 2015

Dispersive liquid-liquid microextraction was combined with flame atomic absorption spectrometry for the determination of manganese in water samples. 1-(2-Pyridylazo)-2-naphthol (PAN), chloroform and ethanol were used as chelating agent, extraction solvent and disperser solvent, respectively. In this extraction method, a mixture of 500 μL ethanol (disperser solvent) and 100 μL chloroform (extraction solvent) was rapidly injected by syringe into the water sample containing manganese ions and 4×10^{-4} mol L^{-1} 1-(2-pyridylazo)-2-naphthol (PAN) (chelating agent). Thereby, a cloudy solution was formed. After centrifugation (5 min at 4000 rpm), the droplets of the cloud were settled at the bottom of the conical test tube (70 ± 2 μL). The settled phase was separated using a micro-syringe and diluted to 100 μL with ethanol. A microsample introduction system was employed for the nebulization of a micro-volume of the diluted solution into FAAS. Some effective parameters on extraction and complex formation, such as extraction and disperser solvent type and their volume, extraction time, salt effect, pH and concentration of the chelating agent, were optimized. Under the optimum conditions, an enrichment factor (EF) of 50 was obtained from only 5 mL of water sample. The calibration graph was linear in the range of 10–200 ng mL^{-1} with limit of detection (LOD) of 3.0 ng mL^{-1} . The relative standard deviation (R.S.D.) for ten replicate measurements of 50 ng mL^{-1} of manganese was 3.3 %. The method was successfully applied for the extraction and determination of manganese in some natural water samples.

Keywords: Dispersive liquid-liquid microextraction, Preconcentration, Manganese, Water sample, FAAS.

INTRODUCTION

Manganese is a necessity for the proper function of several enzymes and is an essential micro-nutrient for the function of the brain, nervous system and normal bone growth. It is present in large quantities in various steel materials as a hardening agent. It also finds application in pharmaceutical preparations. However, excessive intake can cause lesions, headache, psychotic behavior, drowsiness and other related symptoms and/or diseases. Thus manganese is an important element from the environmental perspective [1]. In general, concentrations of manganese in fresh waters [2] are within the range from 0.02 to 130 ng mL^{-1} . Therefore, the determination of this metal as Mn^{2+} ion often requires a method offering low detection limits. Although atomic spectrometric methods are powerful analytical tools for the determination of trace elements in environmental samples, preconcentration techniques combined with AAS are still necessary [3]. Liquid-liquid extraction (LLE) [4-6], solid phase extraction (SPE) [7-17] and cloud point extraction (CPE) [18-21] have been widely used for the preconcentration of manganese from water samples prior to its determination by flame atomic absorption spectrometry. However, that technique is rather

time-consuming and requires a large amount of sample. Separation and preconcentration based on dispersive liquid-liquid microextraction (DLLME) offer a convenient alternative to more conventional extraction methods [22]. This is a modified solvent extraction method and its acceptor-to-donor phase ratio is greatly reduced comparing with other extraction methods. In this method, the appropriate mixture of extraction solvent and disperser solvent is rapidly injected by syringe into aqueous samples containing the analytes. Thereby, a cloudy solution is formed. In fact, the cloudy state is due to the formation of fine droplets of extraction solvent dispersed in the sample solution. Then, this cloudy solution is centrifuged and the fine droplets are settled at the bottom of a conical test tube. The determination of the analytes in the settled phase can be performed by instrumental analysis. In this extraction method, any component originally present in the solution that interacts with the fine droplets of extraction solvent directly or after previous derivatization reaction can be extracted from the initial solution and concentrated in the small volume of the settled phase. The advantages of DLLME method are simplicity of operation, rapidity, low cost, high recovery and enrichment factor. The dispersive liquid-liquid extraction methodology has been used to separate and preconcentrate organic compounds prior to their

* To whom all correspondence should be sent:

determination with chromatographic methods [23-25]. The DLLME has also been used for the extraction and preconcentration of metal ions after the formation of sparingly water-soluble complexes [26-27].

In the present work we report on the results obtained in a study of the dispersive liquid-liquid microextraction of manganese after the formation of a complex with PAN, with subsequent analysis by flame atomic absorption spectrometry using microsample introduction. The proposed method was also applied to the determination of manganese in water samples.

EXPERIMENTAL

Apparatus

A Thermo M series (Model: M5) flame atomic absorption spectrometer was utilized, equipped with a 50 mm burner head, deuterium background correction and air-acetylene flame. A manganese hollow cathode lamp (Thermo Scientific S51214) was used as radiation source, operated at 15 mA with a monochromator spectral bandpass of 0.1 nm. For manganese detection, the wavelength was set at the 232.0 nm resonance line. The acetylene and the air-flow rates were 0.8 and 10.0 L min⁻¹, respectively. The Centurion Scientific centrifuge (Model K240R, Arundel, UK) was used to accelerate the phase separation. The pH values were measured with a Metrohm pH-meter (Model: 691, Herisau, Switzerland), supplied with a glass-combined electrode.

Reagents and solutions

All reagents used were of analytical grade. All solutions were prepared with ultra pure water. The manganese stock solution (1000.0 mg L⁻¹) was prepared by dissolving appropriate amounts of Mn (NO₃)₂ in ultra pure water. Working solutions were prepared from the stock solution by serial dilutions with ultra pure water. Chloroform, carbon tetrachloride, chlorobenzene, acetone, methanol and ethanol were of analytical grade from Merck (Darmstadt, Germany). A 1 × 10⁻² mol L⁻¹ solution of 1-(2-pyridylazo)-2-naphthol (PAN) (Merck, Darmstadt, Germany) was prepared by dissolving an appropriate amount of PAN in acetone. This solution was kept in a dark place at room temperature. A stock standard ammonia/ammonium chloride buffer solution (0.1 mol L⁻¹, pH 10.0) was prepared by dissolving an appropriate amount of ammonia in ultra pure water and neutralizing to pH 10.0 with hydrochloric acid. The pipettes and vessels used for trace analysis were kept in 10%

nitric acid for at least 24 h and subsequently washed four times with ultra pure water before use.

Dispersive Liquid-Liquid Microextraction Procedure

5.0 mL of ultra pure water was placed in a 10 mL screw cap glass test tube with conical bottom and spiked at levels of 10-200 ng mL⁻¹ of manganese. Then 0.2 mL of 1.0 × 10⁻² mol L⁻¹ of PAN (as chelating agent) was added to this solution and the pH of the solution was adjusted by adding ammonia / ammonium chloride buffer solution (1.0 × 10⁻³ mol L⁻¹, pH 10.0). Then a mixture of 500 µL of ethanol (as disperser solvent) and 100 µL of chloroform (as extraction solvent) was injected rapidly into the sample solution by using 1.0-mL syringe, and the mixture was gently shaken. A cloudy solution (water, ethanol and chloroform) was formed in the test tube. In this step, manganese ions were extracted into the fine droplets of chloroform. The mixture was then centrifuged for 5 min at 4000 rpm. After this process, the dispersed fine droplets of chloroform were settled at the bottom of the conical test tube (70 ± 2 µL). The settled phase was separated using a micro-syringe, diluted to 100 µl with ethanol and then injected into the microsample introduction (discrete nebulization) system of FAAS.

RESULTS AND DISCUSSION

In this research, DLLME combined with FAAS was developed for determination of manganese in water samples. In order to obtain a high recovery and a high enrichment factor, the effects of different parameters on the complexation and extraction conditions such as pH, concentration of buffer and chelating agent, kind of extraction and disperser solvent and their volumes, extraction time and salt addition, were optimized. In order to study the mentioned parameters, extraction recovery and enrichment factor were calculated by equations (1) and (2), respectively.

$$EF = C_{\text{sed}} / C_0 \quad (1)$$

where EF, C_{sed} and C₀ are the enrichment factor, concentration of analyte in the sedimented phase and initial concentration of analyte in the aqueous sample, respectively.

$$R \% = [(C_{\text{sed}} \times V_{\text{sed}}) / (C_0 \times V_{\text{aq}})] \times 100 = [(EF \times V_{\text{sed}}) / V_{\text{aq}}] \times 100 \quad (2)$$

where R %, V_{sed} and V_{aq} are the extraction recovery, volume of sedimented phase and volume of aqueous sample, respectively. These parameters are known except C_{sed}. Calculation of C_{sed} was done by direct injection of a standard solution of Mn-

PAN complex in chloroform with concentration in the range of 0.5-10 $\mu\text{g mL}^{-1}$ to FAAS.

Effect of pH

The separation of metal ions by dispersive liquid-liquid microextraction involves prior formation of a complex with sufficient hydrophobicity to be extracted into the small volume of sedimented phase, thus achieving the desired preconcentration. The pH value plays a unique role in metal-chelate formation and subsequent extraction. The effect of pH on the complex formation and extraction of manganese from water samples was studied within the pH range of 2-12 by addition of NaOH or HCl. The results are illustrated in Figure 1. According to these results, the pH of 10.0 was chosen for the extraction.

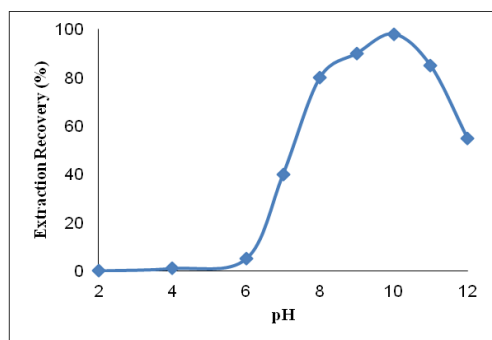


Fig. 1. Effect of pH on the extraction recovery of manganese by DLLME. Extraction conditions: water sample volume, 5.0 mL; disperser solvent (ethanol) volume, 500 μL ; extraction solvent (CHCl_3), 100 μL ; PAN concentration, $4.0 \times 10^{-4} \text{ mol L}^{-1}$, concentration of manganese, $50 \mu\text{g L}^{-1}$.

Effect of PAN concentration

Dispersive liquid-liquid microextraction of 0.25 μg of manganese using PAN from 5.0 mL sample solutions was conducted by varying the concentration of PAN. The extraction recovery for Mn (II) as a function of the concentration of chelating agent is shown in Figure 2. The recovery increases up to a PAN concentration of $1.0 \times 10^{-4} \text{ mol L}^{-1}$ and reaches near quantitative extraction efficiency. A concentration of $4.0 \times 10^{-4} \text{ mol L}^{-1}$ of PAN was chosen to account for other extractable species that might potentially interfere with the assaying of Mn (II).

Effect of Type and Volume of Extraction Solvent

Careful attention should be paid to the selection of the extraction solvent. It should have higher density than water, extraction capability for the compounds of interest and low solubility in water. Chloroform, carbon tetrachloride and

chlorobenzene were compared in the extraction of manganese. A series of sample solutions were studied by using 500 μL ethanol and different volumes of extraction solvent to achieve 70 μL volume of sedimented phase. Thereby, 100, 80 and 80 μL of chloroform, carbon tetrachloride and chlorobenzene, respectively, were used. The results revealed that chloroform has the highest extraction efficiency (98.5 %) in comparison with carbon tetrachloride (32.0 %) and chlorobenzene (76.0 %). Hence, chloroform was chosen as extraction solvent.

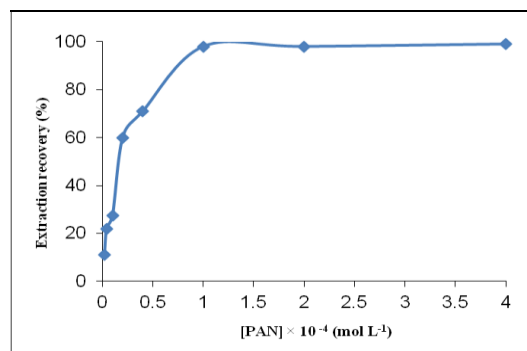


Fig. 2. Effect of PAN concentration on the extraction recovery of manganese by DLLME. Extraction conditions: water sample volume, 5.0 mL; disperser solvent (ethanol) volume, 500 μL ; extraction solvent (CHCl_3), 100 μL ; concentration of manganese, $50 \mu\text{g L}^{-1}$; pH = 10.0.

To examine the effect of the extraction solvent volume, solutions containing different volumes of chloroform were subjected to the same DLLME procedure. The experimental conditions were fixed and included the use of 500 μL ethanol containing different volumes of chloroform. Figure 3 shows the curve of extraction recovery *versus* volume of the extraction solvent (chloroform). According to Figure 3, the extraction recovery increases up to

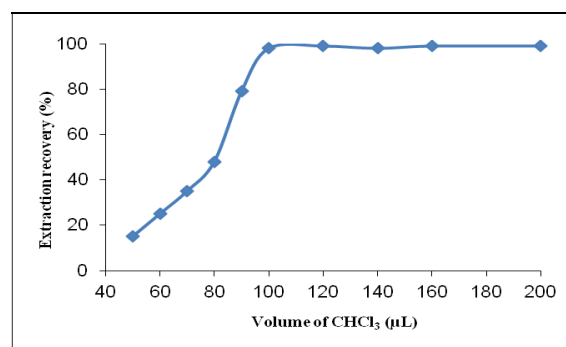


Fig. 3. Effect of the volume of extraction solvent (CHCl_3) on the extraction recovery of manganese by DLLME. Extraction conditions: water sample volume, 5.0 mL; disperser solvent (ethanol) volume, 500 μL ; PAN concentration, $4.0 \times 10^{-4} \text{ mol L}^{-1}$; concentration of manganese, $50 \mu\text{g L}^{-1}$; pH= 10.0.

100 μL of chloroform and then remains constant. Thus, 100 μL of chloroform was chosen as the optimum amount.

Effect of Type and Volume of Disperser Solvent

The main criterion for selection of the disperser solvent is its miscibility in both the extraction solvent and the aqueous sample. For this purpose, different solvents such as acetone, ethanol and methanol were tested. A series of sample solutions were studied by using 500 μL of each disperser solvent containing 100 μL of chloroform (extraction solvent). The results showed the best extraction recovery when ethanol was used. Thus, ethanol was selected as a disperser solvent.

Investigation of the effect of different volumes of ethanol (disperser solvent) on the extraction recovery would be very rough, because the variation of the volume of ethanol makes change in the volume of settled phase at constant volume of chloroform (extraction solvent). Thereby, to achieve a constant volume of the settled phase (70 μL) the volumes of ethanol and chloroform were changed simultaneously. The experimental conditions were fixed and included the use of different volumes of ethanol, 300, 400, 500, 600, 700, 800, 900, 1000, 1200 and 1500 μL containing 90, 95, 100, 105, 110, 115, 120, 125, 135 and 150 μL of chloroform, respectively. Under these conditions, the volume of the sedimented phase was constant ($70 \pm 2 \mu\text{L}$). Figure 4 shows the curve of extraction recovery *versus* volume of the disperser solvent (ethanol). The results show that there was no considerable variation of the extraction recovery between 400 and 800 μL of ethanol and the extraction recovery was high and then decreased by increasing the volume of ethanol. It is clear that by increasing the volume of ethanol, the solubility of

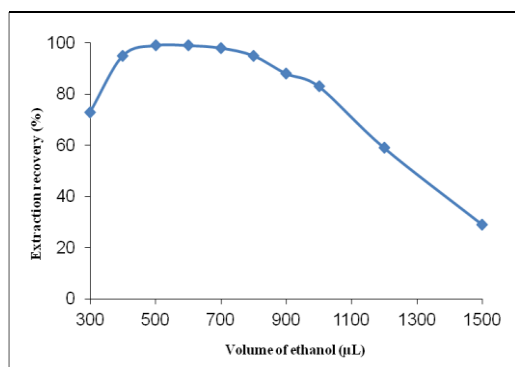


Fig. 4. Effect of the volume of disperser solvent (ethanol) on the extraction recovery of manganese by DLLME. Extraction conditions: water sample volume, 5.0 mL; extraction solvent (CHCl_3), 100 μL ; PAN concentration, $4.0 \times 10^{-4} \text{ mol L}^{-1}$; concentration of manganese, 50 $\mu\text{g L}^{-1}$; pH = 10.0.

the complex in water increases. Therefore, the extraction recovery decreases. Thus, 500 μL of ethanol was selected as the optimum volume in order to achieve a better and more stable cloudy solution.

Effect of Extraction Time

Extraction time is one of the most important factors in most extraction procedures. In DLLME, the extraction time is defined as the interval of time between injecting the mixture of disperser and extraction solvent, and starting centrifugation. The effect of extraction time was examined in the range of 0-45 min under constant experimental conditions. The results showed that the extraction time has no significant effect on the extraction efficiency. It was revealed that after the formation of the cloudy solution, the surface area between the extraction solvent and the aqueous phase is essentially infinitely large. Thereby, transfer of Mn-PAN complex from the aqueous phase to the extraction solvent is fast. This is one of the considerable advantages demonstrated by the DLLME technique, i.e., short extraction time.

Effect of Buffer Concentration

The influence of buffer amounts was studied by maintaining the other experimental variables constant. The results showed that above $0.5 \times 10^{-3} \text{ mol L}^{-1}$ of buffer solution, no obvious variation of the extraction yield took place. Thus, $1.0 \times 10^{-3} \text{ mol L}^{-1}$ of buffer solution was chosen as the optimal to achieve higher buffering capacity.

Effect of Salt

For investigating the influence of ionic strength on the performance of DLLME, experiments were carried out by adding different amounts of NaCl ($0.0 - 1.0 \text{ mol L}^{-1}$). The other experimental conditions were kept constant. The results showed that the ionic strength has no appreciable effect upon extraction efficiency up to 1.0 mol L^{-1} of NaCl. These observations showed the possibility of using this method to separation of manganese from highly saline solutions.

Effect of Other Ions

The effects of common ions in natural water samples on the recovery of manganese were studied. In these experiments, 5.0 mL of solutions containing 50 ng mL^{-1} of manganese and various amounts of interfering ions were treated according to the recommended procedure. An ion was considered to interfere when its presence produced a variation of more than 5% in the extraction

recovery of the sample. The results (Table 1) indicate that the Mn (II) recoveries are almost quantitative in the presence of interfering ions.

Table 1. Effect of foreign ions on the preconcentration and determination of manganese.

| Ion | Ion/Mn(II) (w/w) | Recovery (%) |
|-------------------------------|---------------------|-----------------|
| Li ⁺ | 1000 | 96.4 |
| Na ⁺ | 1000 | 101.5 |
| Cu ²⁺ | 500 | 98.7 |
| Ni ²⁺ | 500 | 95.8 |
| Al ³⁺ | 500 | 99.3 |
| Zn ²⁺ | 500 | 104.2 |
| Pb ²⁺ | 250 | 103.7 |
| Cd ²⁺ | 250 | 97.5 |
| Co ²⁺ | 100 | 99.5 |
| Cr ³⁺ | 100 | 102.6 |
| Fe ²⁺ | 50 | 104.3 |
| NO ₃ ⁻ | 1000 | 100.9 |
| Cl ⁻ | 500 | 96.6 |
| SO ₄ ²⁻ | 250 | 95.8 |

Figures of Merit

Table 2 summarizes the analytical characteristics of the optimized method, including linear range, limit of detection, repeatability, and enrichment factor. The calibration graph was linear within the range of 10-200 ng mL⁻¹ of manganese. The limit of detection, defined as C_L = 3S_B / m (where C_L, S_B and m are the limit of detection, standard deviation of the blank and slope of the

calibration graph, respectively), was 3.0 ng mL⁻¹. The relative standard deviation (RSD) for ten replicate measurements of 50 ng mL⁻¹ Mn (II) was 3.3 %. The enrichment factor was 50.

Application to Samples

The proposed DLLME-FAAS methodology was applied to the determination of Mn in several water samples. Water samples (i.e. tap water, sea water, river water and mineral water) were filtered through a 0.45 μm pore size membrane filter to remove suspended particulate matter and aliquots of water (5.0 mL) were subjected to DLLME. According to the results, the concentration of manganese in the analyzed water samples was below the LOD of the method. Moreover, the robustness of the proposed method was checked by performing recovery test on a synthetic sample (no certified reference material was available). Each type of water was spiked with variable amounts of Mn (II) to assess matrix effects. The results are shown in Table 3.

Table 2. Analytical characteristics of the proposed method.

| Parameter | Analytical feature |
|--|--------------------|
| Linear range (ng mL ⁻¹) | 10-200 |
| Limit of detection (ng mL ⁻¹) (n =10) | 3.0 |
| Repeatability (RSD, %) (n =10) | 3.3 |
| Enrichment factor | 50 |

Table 3. Determination of Mn (II) in different water samples.

| Sample | Mn ²⁺ spiked (ng mL ⁻¹) | Mn ²⁺ detected (ng mL ⁻¹) | Recovery (%) |
|--|---|---|-----------------|
| Tap water | 0.00 | n.d. ^a | — |
| (From the drinking water system of Tehran, Iran) | 0.10 | 0.098 (3.6) ^b | 98 |
| | 0.20 | 0.198 (3.5) | 99 |
| Sea water | 0.00 | n.d. | — |
| (Caspian sea water, Iran) | 0.10 | 0.102 (3.7) | 102 |
| | 0.20 | 0.192 (3.8) | 96 |
| River water | 0.00 | n.d. | — |
| (Ziarat River, Gorgan, Iran) | 0.10 | 0.101 (3.6) | 101 |
| | 0.20 | 0.190 (3.5) | 95 |
| Mineral water | 0.00 | n.d. | — |
| (From Abali mineral water, Tehran, Iran) | 0.10 | 0.097 (3.4) | 97 |
| | 0.20 | 0.206 (3.5) | 103 |

^a Not detected; ^b RSD of three replicate experiments

Table 4. Comparison of the present method with other methods for pre-concentration and determination of manganese(II).

| Method | LOD ng mL ⁻¹ | RSD (%) | EF | Reference |
|--------------|----------------------------|------------|-----|--------------|
| CPE-FAAS | 2.9 | 1.3 | 17 | 19 |
| CPE-FAAS | 5.0 | — | 20 | 20 |
| DLLME-UV-Vis | 4.0 | 3.8 | 5.9 | 28 |
| CPE-FAAS | 33 | — | 96 | 29 |
| SPE-UV-Vis | 17 | — | 60 | 30 |
| DLLME-FAAS | 3.0 | 3.3 | 50 | Present work |

The relative recoveries of manganese from the mentioned water samples at various spiking levels were between 95.0 and 103.0 %. These results demonstrated that the matrices of these water samples had little effect on DLLME of manganese.

Comparison with other methods

A comparison of the present method with other reported methods for manganese preconcentration and determination is given in Table 4. The present method has low LOD, good enrichment factor and good RSD and these characteristics are comparable or even better than most of the other methods named in Table 4. All these results indicate that the present method is a reproducible, simple, and low-cost technique that can be used for the preconcentration and determination of manganese (II) in real samples.

CONCLUSION

Dispersive liquid-liquid microextraction combined with flame atomic absorption spectrometry allows tackling the determination of manganese in natural waters in a simple way. The method is efficient, rapid and economical. High preconcentration factor was obtained easily through this method and a detection limit at the sub ng mL⁻¹ level was achieved with only 5.0 mL of sample. In this method preparation time, as well as consumption of toxic organic solvents was minimized without affecting the sensitivity of the method.

Acknowledgements: The author thanks the research council at the Qaemshahr Branch of Islamic Azad University for financial support.

REFERENCES

1. K. C. Teo, J. Chen, *Analyst*, **126**, 534 (2001).
2. H. J. M. Bowen, *Environmental Chemistry of the Elements*, Academic Press, London, UK, 1979, p. 15.
3. A. Mizuike, *Enrichment Techniques for Inorganic Trace Analysis*, Springer-Verlag, Berlin, 1983.
4. P.K. Tarafder, R.K. Mondal, L. Kunkal, P. Murugan, D.P.S. Rathore, *Chem. Anal. (Warsaw)*, **49**, 251 (2004).
5. S.A. Barakat, *Anal. Chim. Acta*, **393**, 223 (1999).
6. D.T. Burns, S.A. Barakat, M. Harriott, M.S. El-Shahawi, *Anal. Chim. Acta*, **270**, 213 (1992).
7. C. Cui, M. He, B. Hu, *J. Hazard. Mater.* **187**, 379 (2011).
8. S.G. Ozcan, N. Satiroglu, M. Soylak, *Food Chem. Toxicol.*, **48**, 2401 (2010).
9. M. Ghaedi, K. Niknam, K. Taheri, H. Hossainian, M. Soylak, *Food Chem. Toxicol.*, **48**, 891 (2010).
10. A. Baysal, S. Akman, *Environ. Monit. Assess.*, **160**, 199 (2010).
11. S. Tokalioglu, V. Yilmaz, S. Kartal, *Environ. Monit. Assess.*, **152**, 369 (2009).
12. D. Rekha, K. Suvardhan, J.D. Kumar, P. Subramanyam, P.R. Prasad, Y. Lingappa, P. Chiranjeevi, *J. Hazard. Mater.*, **146**, 131 (2007).
13. P. Pohl, B. Prusisz, *Food Chem.* **102**, 1415 (2007).
14. A.P. dos Anjos, L. Cornejo-Ponce, S. Cadore, N. Baccan, *Talanta*, **71**, 1252 (2007).
15. M. Knap, K. Kilian, K. Pyrzynska, *Talanta*, **71**, 406 (2007).
16. M. Soylak, M. Tuzen, *J. Hazard. Mater. B.* **137**, 1496 (2006).
17. M. Grotti, M.L. Abemoschi, F. Soggia, R. Frache, *Anal. Bioanal. Chem.*, **375**, 242 (2003).
18. H. Cesur, *Turk. J. Chem.*, **27**, 307 (2003).
19. Z. Sun, P. Liang, Q. Ding, Jing Cao, *Anal. Sci.*, **22**, 911 (2006).
20. V.O. Doroschuk, S.O. Lelyushok, V.B. Ishchenko, S.A. Kulichenko, *Talanta*, **64**, 853 (2004).
21. A.R. Rod, Sh. Borhani, F. Shemirani, *Eur. Food Res. Technol.*, **223**, 649 (2006).
22. M. Rezaee, Y. Assadi, M. R. Milani Hosseini, E. Aghaee, F. Ahmadi, S. Berijani, *J. Chromatogr. A.*, **1116**, 1 (2006).
23. R. R. Kozani, Y. Assadi, F. Shemirani, M. R. Milani Hosseini, M. R. Jamali, *Talanta*, **72**, 387 (2007).
24. R. R. Kozani, Y. Assadi, F. Shemirani, M. R. Milani Hosseini, M. R. Jamali, *Chromatographia*, **66**, 81 (2007).
25. S. Berijani, Y. Assadi, M. Anbia, M. R. Milani Hosseini, E. Aghaee, *J. Chromatogr. A.*, **1123**, 1 (2006).
26. E. Zeini Jahromi, A. Bidari, Y. Assadi, M. R. Milani Hosseini, M. R. Jamali, *Anal. Chim. Acta.* **585**, 305 (2007).
27. P. Liang, H. Sang, *Anal. Biochem.*, **380**, 21 (2008).
28. I.S. Balogha, L. Rusnakova, J.S Krlikova, L. Kocurova, M. Torokc, V. Andruch, *Intern. J. Environ. Anal. Chem.*, **92**, 1059 (2012).
29. M.A. Farajzadeh, M.R. Fallahi, *Anal. Sci.*, **22**, 635 (2006).
30. M. Dogutan, H. Filik, *Analytica Chimica Acta*, **485**, 205 (2003).

ОПРЕДЕЛЯНЕ НА СЛЕДИ ОТ МАНГАН ВЪВ ВОДНИ ПРОБИ ЧРЕЗ ПЛАМЪКОВА АТОМНО-АБСОРБЦИОННА СПЕКТРОФОТОМЕТРИЯ СЛЕД ДИСПЕРСИОННА ТЕЧНО-ТЕЧНА МИКРО-ЕКСТРАКЦИЯ

А. Мираби^{1*}, М.Р. Джамали², К. Каземи¹

¹ Департамент по химия, Клон Кхаемшахр, Ислямски университет „Азад“, Кхаемшахр, Иран

² Департамент по химия, Университет Паяме Нур, Бехшахр, Иран

Постъпила на 20 април, 2015 г.; приета на 28 декември, 2015 г.

(Резюме)

Дисперсионната течна-течна микро-екстракция е комбинирана с чрез пламъкова атомно-абсорбционна спектрофотометрия за определянето на манган във водни проби. Използвани са 1-(2-пиридиазо)-2-нафтол (PAN), хлороформ и етанол като хелатни агенти, екстрагент и диспергиращ разтворител. По този екстракционен метод смес от 500 μL етанол и 100 μL хлороформ (екстрагент) се инжектира бързо във водна проба, съдържаща манганови йони и $4 \times 10^{-4} \text{ mol L}^{-1}$ 1-(2-пиридиазо)-2-нафтол (PAN) (хелатообразуващ агент). Получава се мътна дисперсия. След центрофугиране (5 мин. при 4000 об./мин.) става утаяване на капки от дисперсията в конична епруветка ($70 \pm 2 \mu\text{L}$). Утаената фаза се отделя с помощта на микро-спринцовка и се разрежда до 100 μl д етанол. Тази система за въвеждане микро-проби се използва за анализ на разредени разтвори в чрез пламъкова атомно-абсорбционна спектрофотометрия. Оптимизирани са някои ефективни параметри на екстрагента и типът на диспергиращия разтворител и техния, времето за екстракция, солевият ефект, рН и концентрацията на хелатообразуващия агент. При оптималните условия факторът на обогатяване (EF) е 50 и е получен от водна проба само от 5 mL. Калибрационната линия е права в интервала 10–200 ng mL^{-1} с граница на откриване 50 ng mL^{-1} манган и 3.3 %. Методът е приложен успешно за екстракцията и определянето на манган в проби от някои природни води.

A new synthesis method and photophysical properties of Ir(C[^]N)₃ cyclometalated iridium phosphorescent complexes

Q.-W. Chang^{1,2}, J. Li², C.-X. Yan², J. Jiang², J.-L. Chen², Q.-S. Ye², J. Yu², W.-P. Liu^{1,2*}

¹Faculty of Material Science and Engineering, Kunming University of Science and Technology, Kunming 650093, Yunnan, People's Republic of China

²State Key Laboratory of Advanced Technologies for Comprehensive Utilization of Platinum Group Metals, Kunming Institute of Precious Metals, Kunming 650106, Yunnan, People's Republic of China

Received September 25, 2015, Revised October 13, 2015

A new convenient synthesis method with excellent yields for Ir(ppy)₃ and Ir(piq)₃ is developed using [(acac-O,O)₂(acac-C³)Ir(H₂O)] as an efficient starting material. Their structures are fully characterized by elemental analysis, ¹H-NMR and ESI-MS. The photophysical properties of both compounds are studied by UV-visible spectra and photoluminescence spectra.

Keyword: iridium, cyclometalated complexes, synthesis, phosphorescent, Ir(C[^]N)₃.

INTRODUCTION

Neutral cyclometalated iridium phosphorescent complexes with Ir(C[^]N)₃ and Ir(C[^]N)₂(LL) types are the most promising phosphorescent materials in organic light-emitting devices (OLEDs)[1-4]. Tris-cyclometalated iridium complexes have attracted considerable attention due to a potential application in OLED [5]. Several experimental procedures[5-6] have been developed for their synthesis using IrCl₃·nH₂O, Ir(acac)₃, [Ir(acac)(coe)₂] or the chlorinated bridged dimer as a precursor, their synthesis often requires harsh reaction conditions to proceed so that they can not be widely be applied in OLED. Therefore, developing the new synthesis route for Ir(C[^]N)₃ type phosphorescent complexes is very worthy and interesting. [(acac-O,O)₂(acac-C³)Ir(H₂O)] has a rich coordination and reaction chemistry due to the presence of a coordinated water ligand [7-9], which has a better reaction activity than Ir(acac)₃ for preparing Ir(C[^]N)₃ type phosphorescent complexes. In this contribution, a new convenient synthesis method with excellent yields for Ir(ppy)₃ and Ir(piq)₃ is developed using [(acac-O,O)₂(acac-C³)Ir(H₂O)] as a new precursor.

EXPERIMENTAL

General considerations

All manipulations were performed in an atmosphere of high purity argon using conventional Schlenk techniques. All reagents and solvents in this study were used without further purification. [(acac-O,O)₂(acac-C³)Ir(H₂O)] was synthesized

from IrCl₃·nH₂O and NaHCO₃ in refluxing acetylacetone according to the literature[10]. NMR spectra were obtained on a Bruker AV400 using tetramethylsilane as an internal reference. Mass spectrometry studies were carried out on an Autospec 3000 Instrument. Elemental analyses for C, H, and N were performed using a Carlo-Ebra Instrument. UV-visible absorption spectra were measured on a Cary 50Bio spectrophotometer. The photoluminescence (PL) spectra were recorded on an F-7000 spectrometer in CH₂Cl₂.

Synthesis of Fac-Ir(ppy)₃

[(acac-O,O)₂(acac-C³)Ir(H₂O)] (2 g, 3.94 mmol) and 2-phenylpyridine (3.67 g, 23.66 mmol) were refluxed under an inert gas atmosphere in 50 mL of glycerol for 24 h. After the mixture was cooled to room temperature, 50 mL of 1M HCl solution and 50 ml of methanol were added and stirred for 30 min and then filtered to yield the crude product. The crude product was flash chromatographed on a silica column using dichloromethane to yield 80% (2.06 g) product. ¹H-NMR (400 MHz, CDCl₃), ppm: 8.52(d, 1H), 7.84(d, 1H), 7.72(t, 1H), 7.52(d, 1H), 7.13(t, 1H), 6.77(t, 1H), 6.63(t, 1H), 6.27(d, 1H). ESI-MS: m/z = 655(M+1), 501(Ir(ppy)₂+1) Anal. Found: C 60.45, H 3.62, N 6.45. Calcd: C 60.53, H 3.69, N 6.42.

Synthesis of Ir(piq)₃

The synthesis procedure of Ir(piq)₃ was the same for Ir(ppy)₃ except that 1-phenylisoquinoline was used in place of 2-phenylpyridine in the same molar amount: yield 72% (2.28 g). Anal. Found: C 67.12, H 3.74, N 5.20. Calcd: C 67.15, H 3.76, N 5.22. ¹H-NMR (400 MHz, DMSO-*d*₆), ppm: 8.92(d, 1H), 8.16(d, 1H), 7.93(t, 1H), 7.78(t, 2H), 7.48(d, 1H),

* To whom all correspondence should be sent:
E-mail: liuweiping0917@126.com

7.36(d, 1H), 6.90(t, 1H), 6.79(d, 1H), 6.72(t, 1H).
ESI-MS: m/z = 827(M+23), 425(M/2+23).

RESULTS AND DISCUSSION

Synthesis and characterization of Ir(ppy)₃ and Ir(piq)₃

Ir(ppy)₃ and Ir(piq)₃ were synthesized by reacting [(acac-O,O)₂(acac-C³)Ir(H₂O)] with corresponding cyclometalated ligands (see scheme 1). And their structures were confirmed by element analysis, ESI-MS (see experiment section) and ¹H-NMR (see Figure 1). The results match those reported for Ir(ppy)₃ and Ir(piq)₃[11-12] and the molecule structures shown in Figure 2.

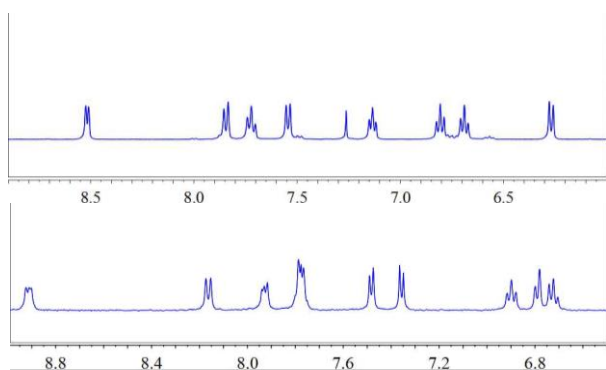


Fig. 1. ¹H-NMR of Ir(ppy)₃ in CDCl₃ (above) and Ir(piq)₃ in DMSO-*d*₆ (below).

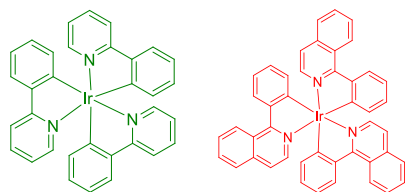


Fig. 2. Molecular structures of Ir(ppy)₃ and Ir(piq)₃.

Photophysical properties of Ir(ppy)₃ and Ir(piq)₃

The absorption and emission spectroscopic behaviors of Ir(ppy)₃ and Ir(piq)₃ are studied at room temperature in CH₂Cl₂. Figure 3 shows the UV-vis absorption and photoluminescence spectra of Ir(ppy)₃. The absorption band observed at 273 nm is related to spin-allowed π - π^* transitions (corresponding to ligand centered states, ¹LC) of the cyclometalated ppy ligands. The broad and unresolved absorption band at lower energy,

peaking at 367nm, is assigned to spin-allowed d- π^* transitions (corresponding to metal-to-ligand charge transfer states, ¹MLCT), whereas absorptions at wavelengths between at 430 nm and 500 nm involve ³MLCT states. The emission at ambient temperature shows a maximum peak at 512 nm. The UV-vis absorption and photoluminescence spectra of Ir(piq)₃ are also given in Figure 4. In the range below about 350 nm, the band is related to spin-allowed π - π^* transitions (¹LC), and the two lower-energy bands appear in the region of about 370-550 nm are tentatively assigned to the ¹MLCT and ³MLCT transitions. The maximum emission peak of Ir(piq)₃ is at 619 nm.

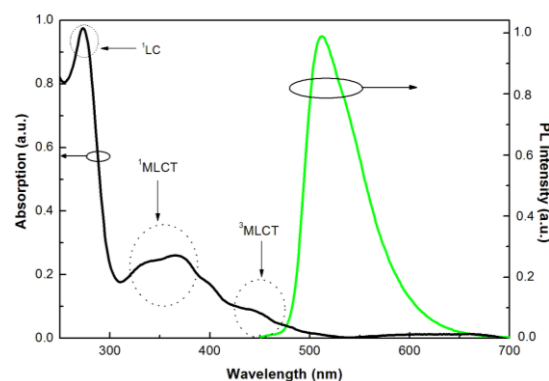


Fig. 3. Absorption and photoluminescence spectra of Ir(ppy)₃ in CH₂Cl₂ at ambient temperature.

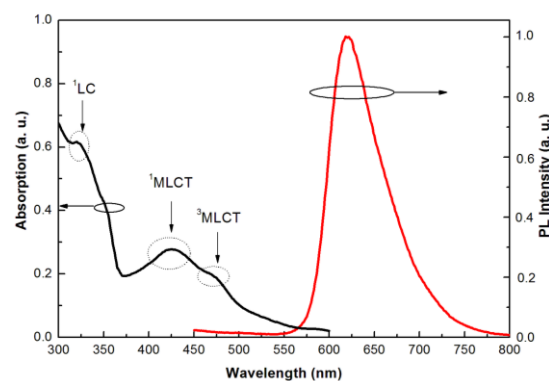
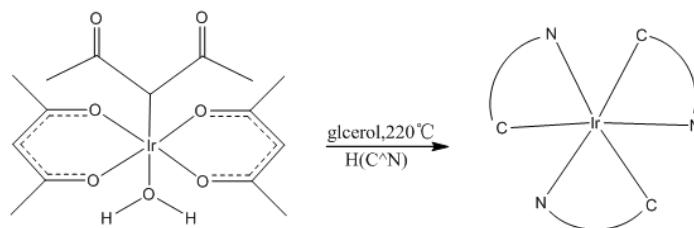


Fig. 4. Absorption and photoluminescence spectra of Ir(piq)₃ in CH₂Cl₂ at ambient temperature.



Scheme 1. Synthesis route of Ir(C^N)₃ type phosphorescent complexes.

Comparing the absorption and emission spectra of Ir(ppy)₃ and Ir(piq)₃, both compounds show similar spectral features which agree with the reports in the literature [12-15]. Differently, the absorption and emission peaks of Ir(piq)₃ have a red shift due to the bigger conjugation degree of piq than that of ppy.

CONCLUSION

In conclusion, The advantages of the herein described synthetic procedures are that the complexes Ir(ppy)₃ and Ir(piq)₃ can be obtained in high yields by a convenient method starting from [(acac-O,O)₂(acac-C³)Ir(H₂O)]. The general usefulness of the described procedures for the synthesis of closely related cyclometalated iridium complexes will be examined by us in the near future.

Acknowledgments: The authors are grateful to Yunnan Provincial Science Foundation (Grant No. 2015IB019) and Kunming Science Foundation (Grant No.2016KJJH059) P.R.China for the financial support.

REFERENCES

1. S. Lamansky, P. Djurovich, D. Murphy, F. Abdel-Razzaq, H. E. Lee, C. Adachi, P. E. Burrows, S. R. Forrest, M. E. Thompson, *J. Am. Chem. Soc.*, **123**, 4304 (2001).
2. M. A. Baldo, D. F. O'Brien, Y. You, A. Shoustikov, S. Sibley, M. E. Thompson, S. R. Forrest, *Nature*, **395**,151 (1998).
3. M. G. Helander, Z. B. Wang, J. Qiu, M. T. Greiner, D. P. Puzzo, Z. W. Liu, Z. H. Lu, *Science*, **332**, 944 (2011).
4. A. B. Tamayo, B. D. Alleyne, P. I. Djurovich, S. Lamansky, I. Tsyba, N. N. Ho, R. Bau, M. E. Thompson, *J. Am. Chem. Soc.*, **125**, 7377 (2003).
5. S. Lamansky, P. Djurovich, D. Murphy, F. Abdel-Razzaq, R. Kwong, I. Tsyba, M. Bortz, B. Mui, R. Bau, M. E. Thompson, *Inorg. Chem.*, **40**, 1704 (2001).
6. H. C. Böttcher, M. Graf, K. Sünkel, P. Maver, H. Krüger, *Inorganica Chimica Acta*, **365**,103 (2011).
7. Q. Chang, J. Chen, M. Xie, W. Liu, Y. Yu, Q. Ye, X. Chen, *J. Struct. Chem.*, **52**, 824 (2011).
8. Q. W. Chang, C. Y. Hu, J. L. Chen, M. J. Xie, W. P. Liu, Q. S. Ye, Y. Yu, X. Z. Chen, L. Q. Chen, *Transit. Met. Chem.*, **36**, 337 (2011).
9. Q. W. Chang, G. F. Chen, C. Y. Hu, J. L. Chen, Q. S. Ye, X. Z. Chen, J. Jiang, W. P. Liu, *Res. Chem. Intermed.*, **38**, 1571 (2012)..
10. R. A. Periana, X. Y. Liu, G. Bhalla, *Chem. Commun.*, **24**, 3000 (2002).
11. M. Lepeltier, F. Dumur, J. Marrot, E. Contal, D. Bertin, D. Gigmes, C. R. Mayer Dalton, *Trans.*, **42**, 4479 (2013).
12. M. G. Colombo, T. C. Brunold, T. Riedener, H. U. Güdel, *Inorg. Chem.*, **33**, 545 (1994).
13. W. Holzer, A. Penzkofer, T. Tsuboi, *Chemical Physics Letters*, **308**, 93 (2005).
14. H. Yersin, T. Hofbeck, *Inorg. Chem.*, **49**, 9290 (2010).
15. J. Brey, P. Stössel, S. Schrader, A. Starukhin, W. J. Finkenzeller, H. Yersin, *Chem. Mater.*, **15**, 1745 (2005).
16. K. Dedeian, P. I. Djurovich, F. O. Garces, G. Carlson, R. J. Watts, *Inorg. Chem.*, **29**, (1990).

НОВ МЕТОД ЗА СИНТЕЗАТА И ФОТО-ФИЗИЧНИ СВОЙСТВА НА Ir(C^N)₃ ЦИКЛОМЕТАЛИРАНИ ИРИДИЕВИ ФОСФОРЕСЦЕНТНИ КОМПЛЕКСИ

К.-У. Чанг^{1,2}, Дж. Ли², Ц.-С. Ян², Дж. Джианг², Дж.-Л. Чен², К.-С. Йе², Дж. Ю, У.-П. Лю^{1,2*}

¹Факултет по материалознание и инженерство, Кунминг'ски университет за наука и технология, Кунминг 650093, Юнан, КНР

²Държавна ключова лаборатория по нови технологии за пълно оползотворяване на метали от платиновата група, Кунминг'ска лаборатория за благородни метали, Кунминг 650106, Юнан, КНР

Постъпила на 25 септември 2015 г.; коригирана на 13 октомври 2015 г.

(Резюме)

Създаден е нов удобен метод за синтеза на Ir(ppy)₃ и Ir(piq)₃ с отличен добив. Като изходен материал е използван [(acac-O,O)₂(acac-C³)Ir(H₂O)]. Тяхната структура е напълно охарактеризирана чрез елементен анализ, ¹H-NMR и ESI-MS. Фотофизичните свойства на двете съединения са изучени чрез UV-Vis спектри и фотолуминисцентни спектри.

Preparation and modification of peanut shells and their application for heavy metals adsorption

Z. Yang¹, Y. G. Wang^{1,3,4}, Y. J. Jing^{3,4}, Q. W. Wei^{3,4}, F. F. Leng^{3,4}, H. Ma^{3,4}, Y. L. Wang^{3,4}, J. X. Chen^{1,2*}

¹ School of Energy and Power Engineering, Lanzhou University of Technology, Lanzhou 730050, China

² School of Petrochemical Engineering, Lanzhou University of Technology, Lanzhou 730050, China

³ School of Life Science and Engineering, Lanzhou University of Technology, Lanzhou 730050, China

⁴ The Key Lab of Screening, Evaluation and Advanced Processing of TCM and Tibetan Medicine, Gansu Educational Department, Lanzhou 730050, China

Received June 13, 2016, Accepted July 26, 2016

Peanut shells are a test adsorption material, the influences of key factors (pH, reaction duration, initial concentration and adsorption dosage) on its adsorption of heavy metal ions including Pb^{2+} , Cu^{2+} and Zn^{2+} were studied. The results showed that: the adsorption rate of the above mentioned heavy metal ions increased gradually with the pH increase. We also noticed that the adsorption of heavy metal ions by unmodified peanut shells performed well under acidic conditions, while the best results for modified peanut shells were obtained under alkaline conditions. Meanwhile, the adsorption rate reached about 88% of the maximum adsorption rate after treatment for a 15 min reaction and tended to balance after 50 min; with increasing initial ion concentration, the adsorption rate increased gradually, and reached the maximum adsorption rate at 30 mg/L. However, it was gradually reduced when over 30 mg/L. The results revealed that adsorption rate increased with the adsorbent dosage. The dynamic behaviors of both modified and unmodified peanut shells well fit the Lagergren (II) order chemical reaction kinetics model. Additionally, compared with unmodified peanut shells, the adsorption effect for modified shells was significant.

Keywords: Peanut Shell, Adsorption, Heavy Metals, Modification, Dynamics.

INTRODUCTION

The heavy metals, Pb^{2+} , Cu^{2+} , Zn^{2+} , are harmful to the environment. They accumulate in the living organisms by adsorption and thus pose a serious threat to public health. Excessive accumulation of copper *in vivo* could lead to many diseases like diarrhea, skin diseases and even death [1, 2]. Lead is a cumulative poison acting on various systems and organs of the human being [3], such as the hematopoietic and cardiovascular system, the central nervous systems and the reproductive organs [4]. There are many technical methods used to treat contamination by heavy metals, such as ion exchange resin, activated carbon adsorption, chemical precipitation and electrochemical treatment [5]. These methods have some effect, but their cost compared with biotechnology, is much larger and may cause secondary pollution.

In recent years, the biomass material, as an adsorbent applied for controlling heavy metals contamination, is becoming a hot research topic. Biomass materials have the advantage of widespread-sources, convenience, low-cost, directly-treated and thus greatly reduce the cost of

the treatment of heavy metals. Therefore biomass materials find good application prospects [6, 7]. Different from the traditional process, the biological assay has the following advantages: metal ions can be selectively removed with low concentrations of heavy metals; energy-efficiency, cost-effectiveness; easy separation and recovery of heavy metals; the sustainability-adsorbent is easily regenerated and recycled.

As the increasing lack of non-renewable resources such oil and coal, the preparation of new industrial products with agricultural and forestry waste together with other renewable resources as raw materials gradually draws attention from all over the world. The common agricultural and sideline products include bark, cotton shells, peanut shells, sawdust, orange peel and others. A large number of peanut shells are discarded in the natural environment or burned, which not only cause serious environmental pollution, but also are a waste of resources. Peanut hull carbide (PHC), commonly used as a bio-adsorbent produced from piles of peanut shells, is similar to the activated carbon structure in appearance. According to the research, PHC may contain polar functional groups such as aldehydes, ketones, acids and phenolic compounds, which can be involved in the formation

* To whom all correspondence should be sent:
E-mail: 412316788@163.com

of chemical bonds and can adsorb heavy metal ions [9]. In China, peanut shells are cheap and have a wide range of sources. In this paper, peanut shells are used as an adsorbent and therefore the mechanism of heavy metal ions in solution adsorption laws are discussed.

Peanut shells are an abundant inexpensive adsorbent and can be applied to govern heavy metal pollution after modifying its structural characteristics [10]. Up until now, many researchers [11, 12] have removed heavy metal ions from the wastewater using peanut shells as an adsorbent or using peanut shells as a raw material for activated carbon preparation [13], which had a great practical significance for recycling and application of such a large quantity of cheap agricultural and forestry waste in environmental pollution. However, these studies only focus on the effects of polluted water following the adsorption of heavy metals together with characteristics, such as the adsorption temperature, pH, amount of adsorbent and the initial ion concentration. However, these do not fully explore the best adsorption conditions of modified peanut shells. This paper mainly studied the optimum conditions of adsorption. In this paper, we modified peanut shells with 0.1 mol/L of hydrochloric acid and applied modified peanut shells to process the simulated industrial wastewater containing copper, lead and zinc ions, which provided a new thought as regards the utilization of peanut shells and the treatment for heavy metal ions.

MATERIALS AND METHODS

Preparation of solutions and samples

The peanut shells used in this study were derived from fresh peanuts. All the chemical reagents used were analytical grade. A stock solution with 100 mg/L Pb^{2+} , Cu^{2+} , Zn^{2+} respectively was prepared by deionized water, $Pb(NO_3)_2$, $Cu(NO_3)_2$ and $Zn(NO_3)_2$. Working solutions were obtained by appropriate dilution. Peanut shells were smashed and screened through a mesh of size 80. Then the samples were soaked with deionized water for 24 hours and the fine suspended material was removed as well as the soluble matter. The samples were stored in a desiccator after being dried at 80°C the modified peanut shells were prepared as follows: 200 g of peanut shells were placed in a 2.5 L beaker, 500mL 1 mol/L hydrochloric acid was added in the beaker. After being stirred for 1 h, the liquid portion was removed by filtration. The solid fraction was washed with deionized water until neutral and dried at 80°C. Infrared spectrum samples were prepared by

potassium bromide tableting. Unmodified or modified peanut shells powder and potassium bromide powder were thoroughly ground. The mixed powder was made into a transparent sheet with about 1 mm thickness by a pneumatic tableting machine. Then the samples were analyzed by a Fourier transform infrared spectrometer at 400 - 4000 cm^{-1} .

Peanut shells adsorption of simulated industrial wastewater

The ion mixed solution was made from 50 mg/L Pb^{2+} , Cu^{2+} , Zn^{2+} . 60 mL of ion mixed solution was added in an 100 mL Erlenmeyer flask, the pH of which was adjusted. The initial concentration of Pb^{2+} , Cu^{2+} , Zn^{2+} was measured by an atomic absorption spectrophotometer. Unmodified or modified peanut shells were placed in an Erlenmeyer flask and cultured in the constant temperature incubator shaker with an oscillation rate of 120 r/min at 32°C. Thereafter, 10 mL of solution in a centrifugal tube was centrifuged to remove the impurities in the solution. The concentration of Pb^{2+} , Cu^{2+} , Zn^{2+} after adsorption was measured by an atomic absorption spectrophotometer. The adsorption rate was used to determine the optimum adsorption conditions.

Single factor experiment and orthogonal test

The adsorption rate is an evaluation index, four factors including the adsorption reaction duration (A), the initial ion concentration (B), dosage of the samples (C), pH value (D) were selected to be the testing factors of the adsorption efficiency of the peanut shells. According to the results of the single factor experiment, an orthogonal test with four-factors and three-levels was applied to optimize the adsorption condition of the peanut shells.

Kinetics experiments

50 mL, 40 mg/L or a 50 mg/L mixed ion solution was added into a 100 mL Erlenmeyer flask with a pH adjusted to 5.00 ± 0.01 . 0.50 g unmodified peanut shells powder was added in the solution. Then the solution was shaken for 10, 20, 30, 40, 60, 80 min, separately at 32°C. The concentration of Pb^{2+} , Cu^{2+} , Zn^{2+} were assayed and plotted after being filtered and centrifuged. Characterization of the dynamic mechanism of the data in the figure was analyzed using the following two models.

Lagergren apparent first-order kinetic model

$$\ln(1-q/q_e) = -k_1 t \quad (1)$$

In which: q_t , q_e (mg/g) are the Cu^{2+} adsorption at t (min) time, Cu^{2+} equilibrium adsorption. Respectively; k_1 (g/(mg·min)) is the adsorption rate constant of first order which can be obtained by a plot using $\ln(1 - q_t/q_e)$ and t .

Lagergren apparent second-order kinetic model

$$t/q_t = (1/k_2 q_e^2) + (t/q_e) \quad (2)$$

In which: k_2 (g/(mg·min)) is the adsorption rate constant of apparent second order which can be obtained by a plot using t/q_t and t ; $k_2 q_e^2$ (mg/(g·min)) is the initial adsorption rate.

RESULTS AND DISCUSSION

Effect of pH on the adsorption

As shown in Fig. 1, the metal ions adsorption rate of peanut shells increased gradually with the increase of pH at a range of 3-5. Unmodified peanut shells reached a maximum value when the pH was 5 and reduced when the pH was 7. However, modified peanut shells continued to increase gradually under given alkaline conditions. Thus, the optimum pH of unmodified peanut shells was acidic and the optimum pH of modified peanut shells was alkaline. Moreover, the maximum adsorption rate of modified peanut shells was higher than that of unmodified peanut shells. The maximum adsorption rates of unmodified peanut shells for Pb^{2+} , Cu^{2+} , Zn^{2+} were 93.3%, 77.6%, 71.5%, respectively, while the adsorption maximum of modified peanut shells for Pb^{2+} , Cu^{2+} , Zn^{2+} were 96.2%, 87.0%, 74.0%, respectively. Generally, the absorption efficiency of modified peanut shells was better than the unmodified one and the adsorption of peanut shells on Pb^{2+} was the most obvious.

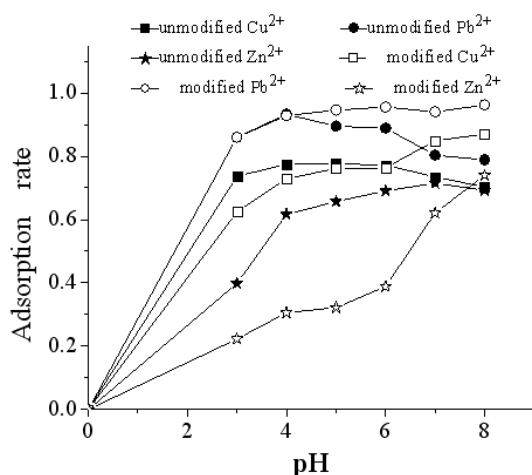


Fig. 1. The influence of pH on adsorption

Effect of the adsorption reaction duration on adsorption

Fig. 2 showed that the adsorption rate of peanut shells for metal ions increased with time and reached a balance after a reaction duration of 50 minutes. The adsorption rate reached 88% of the maximum adsorption rate after 15 min, which showed that the adsorption by peanut shells of metal ions was terminated in a short space of time. The adsorption of modified and unmodified peanut shells and metal ions at the interface between the liquid and solid was mainly physical adsorption. In theory, the longer the reaction duration the more the adsorbent dosage, the more thorough the adsorption removal is. The maximum adsorption rates of unmodified peanut shells for Pb^{2+} , Cu^{2+} , Zn^{2+} were 94.3%, 69.3%, 16.7%, respectively, while the adsorption maximums of modified peanut shells for Pb^{2+} , Cu^{2+} , Zn^{2+} were 68.9%, 48.9%, 16.4%, respectively. Overall, the absorption efficiency of unmodified peanut shells was better than the modified one and the adsorption of peanut shells on Pb^{2+} was the most obvious.

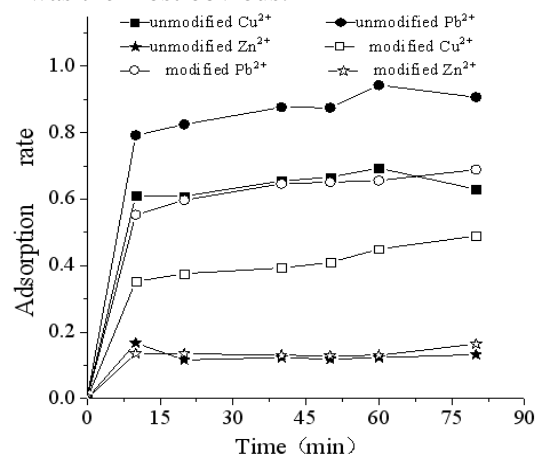


Fig. 2 The influence of reaction duration on adsorption

Effect of the initial ion concentration on adsorption

The absorption rate increased with the initial ion concentration and reached a maximum with the initial ion concentration being 30 mg/L and then reduced gradually. When the initial ion concentration in the solution was much higher, the adsorption sites of the peanut shells for metal ions on the surface were saturated so the adsorption rate gradually decreased. In Fig. 3, when the concentration of metal ions was low, the adsorption rate was relatively high, while the adsorption rate became lower with the higher metal ion concentration, which indicated that the peanut shells were suitable for the adsorption of low metal ion concentrations. The maximum adsorption rates of unmodified peanut shells for Pb^{2+} , Cu^{2+} , Zn^{2+}

were 90.1%, 69.9%, 69.1%, respectively, while the adsorption maximums of modified peanut shells for Pb^{2+} , Cu^{2+} , Zn^{2+} were 85.9%, 77.6%, 78.1%. In total, the absorption efficiency of modified peanut shells was better than the unmodified one and the adsorption of peanut shells on Pb^{2+} was the most obvious.

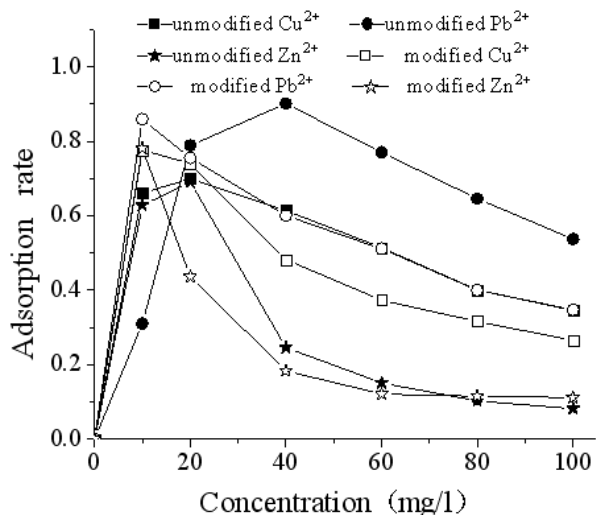


Fig. 3 The effect of the initial concentration on adsorption

Effect of the pH value on the adsorption

As manifested in Fig. 4, the metal adsorption range of unmodified peanut shells were 0.2-0.6g and the adsorption rate increased with the adsorbent dosage.

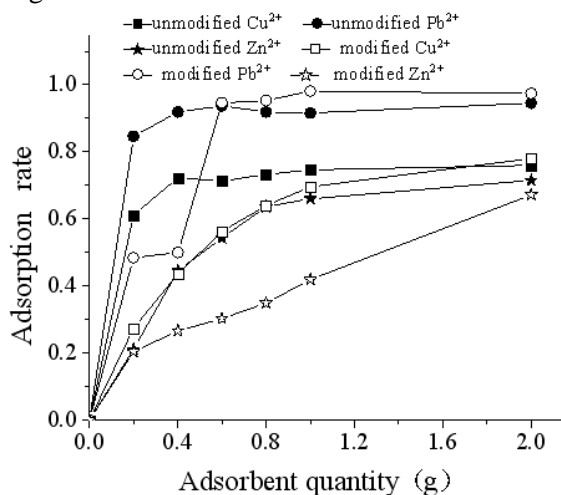


Fig. 4 The effect of the adsorbent dosage on adsorption

The maximum adsorption rates of unmodified peanut shells for Pb^{2+} , Cu^{2+} , Zn^{2+} were 94.5%, 76.0%, 71.5%, respectively. The adsorption rate of modified peanut shells was also increased with the adsorbent dosage and reached the maximum when the dosage of samples was 2.0 g. The adsorption maximums of modified peanut shells for Pb^{2+} , Cu^{2+} ,

Zn^{2+} were 98.1%, 78.0%, 67.2%. Increasing the amount of peanut shells increases the surface area of the peanut shells in the metal solution and the effective adsorption sites, therefore the adsorption rate increases. But when the adsorption rate of the heavy metal ions reach an equilibrium, the increasing adsorbent dosage would reduce the adsorption capacity of the per unit mass adsorbent which means non-saturation of the adsorption capacity and results in a waste of adsorbent. In total, the absorption efficiency of the modified peanut shells was better than that of the ones unmodified and the adsorption efficiency on Pb^{2+} was more obvious.

Analysis of the orthogonal results

Orthogonal results assay of the unmodified peanut shells

The most obvious factor was the initial ion concentration for Cu^{2+} and Zn^{2+} while the most significant factor was the pH value of Pb^{2+} by the Anova and range analysis in Table 1 and Table 2. Based on the K value, the best combinations of Cu^{2+} , Zn^{2+} and Pb^{2+} were $A_2B_3C_1D_1$, $A_3B_3C_3D_2$ and $A_1B_2C_1D_3$ respectively, which meant that the optimum condition for Cu^{2+} was the reaction duration for 60min, the initial ion concentration being 40 mg/L, the 0.5 g of adsorbent at pH 5; the optimum condition for Pb^{2+} lasted for 80min, the initial ion concentration being 40 mg/L, the 0.7 g of adsorbent at pH 6; the optimum condition for Zn^{2+} lasted for 40min, the initial ion concentration being 30 mg/L, the 0.5 g of adsorbent at pH 7.

Orthogonal results analysis of modified peanut shells

According to the Anova and range analysis in Table 3 and Table 4, the most obvious factor was the adsorption reaction duration for Pb^{2+} and Zn^{2+} , while the most significant factor was the initial ion concentration for Cu^{2+} . Based on the K value, the best combination of Cu^{2+} , Zn^{2+} and Pb^{2+} were $A_3B_3C_2D_1$, $A_3B_3C_3D_3$ and $A_1B_2C_3D_3$, respectively, which, in detail, means that the optimum condition for Cu^{2+} was a reaction lasting for 80 min, the initial ion concentration being 30 mg/L, the 1.5 g adsorbent at pH 6; the optimum condition for Pb^{2+} was a reaction lasting for 80 min, the initial ion concentration was 30 mg/L, the 2.0 g adsorbent at pH 8; besides, the optimum condition for Zn^{2+} was a reaction lasting for 60 min, the initial ion concentration was 20 mg/L, the 2.0 g adsorbent at pH 8.

Table 1. Orthogonal experimental results of unmodified peanut shells.

| Factors | Adsorption Rate | | | | | | | | |
|------------|---|------------------|------------------|---|------------------|------------------|---|------------------|------------------|
| | K1 | | | K2 | | | K3 | | |
| A | Cu ²⁺ | Pb ²⁺ | Zn ²⁺ | Cu ²⁺ | Pb ²⁺ | Zn ²⁺ | Cu ²⁺ | Pb ²⁺ | Zn ²⁺ |
| | 0.700 | 0.966 | 0.709 | 0.711 | 0.965 | 0.695 | 0.704 | 0.969 | 0.691 |
| B | Cu ²⁺ | Pb ²⁺ | Zn ²⁺ | Cu ²⁺ | Pb ²⁺ | Zn ²⁺ | Cu ²⁺ | Pb ²⁺ | Zn ²⁺ |
| | 0.653 | 0.953 | 0.711 | 0.710 | 0.955 | 0.715 | 0.753 | 0.992 | 0.669 |
| C | Cu ²⁺ | Pb ²⁺ | Zn ²⁺ | Cu ²⁺ | Pb ²⁺ | Zn ²⁺ | Cu ²⁺ | Pb ²⁺ | Zn ²⁺ |
| | 0.719 | 0.957 | 0.704 | 0.681 | 0.954 | 0.681 | 0.715 | 0.988 | 0.703 |
| D | Cu ²⁺ | Pb ²⁺ | Zn ²⁺ | Cu ²⁺ | Pb ²⁺ | Zn ²⁺ | Cu ²⁺ | Pb ²⁺ | Zn ²⁺ |
| | 0.733 | 0.981 | 0.689 | 0.708 | 0.983 | 0.698 | 0.675 | 0.935 | 0.708 |
| Best Group | Cu ²⁺ | | | Pb ²⁺ | | | Zn ²⁺ | | |
| | A ₂ B ₃ C ₁ D ₁ | | | A ₃ B ₃ C ₃ D ₂ | | | A ₁ B ₂ C ₁ D ₃ | | |

Table 2. Anova table of unmodified peanut shells.

| Variance Source | Factors | | | | | | | | | | | |
|-----------------|---|------------------|------------------|------------------|------------------|------------------|------------------|------------------|------------------|------------------|------------------|------------------|
| | A | | | B | | | C | | | D | | |
| SS | Cu ²⁺ | Pb ²⁺ | Zn ²⁺ | Cu ²⁺ | Pb ²⁺ | Zn ²⁺ | Cu ²⁺ | Pb ²⁺ | Zn ²⁺ | Cu ²⁺ | Pb ²⁺ | Zn ²⁺ |
| | 0.000 | 0.000 | 0.001 | 0.015 | 0.003 | 0.004 | 0.003 | 0.002 | 0.001 | 0.005 | 0.005 | 0.001 |
| Df | Cu ²⁺ | Pb ²⁺ | Zn ²⁺ | Cu ²⁺ | Pb ²⁺ | Zn ²⁺ | Cu ²⁺ | Pb ²⁺ | Zn ²⁺ | Cu ²⁺ | Pb ²⁺ | Zn ²⁺ |
| | 2 | 2 | 2 | 2 | 2 | 2 | 2 | 2 | 2 | 2 | 2 | 2 |
| MS | Cu ²⁺ | Pb ²⁺ | Zn ²⁺ | Cu ²⁺ | Pb ²⁺ | Zn ²⁺ | Cu ²⁺ | Pb ²⁺ | Zn ²⁺ | Cu ²⁺ | Pb ²⁺ | Zn ²⁺ |
| | 0.000 | 0.000 | 0.571 | 2.609 | 1.200 | 2.286 | 0.522 | 0.800 | 0.571 | 0.870 | 2.000 | 0.571 |
| F-value | Cu ²⁺ | Pb ²⁺ | Zn ²⁺ | Cu ²⁺ | Pb ²⁺ | Zn ²⁺ | Cu ²⁺ | Pb ²⁺ | Zn ²⁺ | Cu ²⁺ | Pb ²⁺ | Zn ²⁺ |
| | 4.460 | 4.460 | 4.460 | 4.460 | 4.460 | 4.460 | 4.460 | 4.460 | 4.460 | 4.460 | 4.460 | 4.460 |
| Significance | Cu ²⁺ | Pb ²⁺ | Zn ²⁺ | Cu ²⁺ | Pb ²⁺ | Zn ²⁺ | Cu ²⁺ | Pb ²⁺ | Zn ²⁺ | Cu ²⁺ | Pb ²⁺ | Zn ²⁺ |
| | \ | \ | \ | \ | \ | \ | \ | \ | \ | \ | \ | \ |
| Note | Error: Cu ²⁺ : 0.02, 8; Pb ²⁺ & Zn ²⁺ : 0.01, 8; \—non-significance. | | | | | | | | | | | |

Table 3. Orthogonal experiment results of modified peanut shells

| Factors | Adsorption Rate | | | | | | | | |
|------------|---|------------------|------------------|---|------------------|------------------|---|------------------|------------------|
| | K1 | | | K2 | | | K3 | | |
| A | Cu ²⁺ | Pb ²⁺ | Zn ²⁺ | Cu ²⁺ | Pb ²⁺ | Zn ²⁺ | Cu ²⁺ | Pb ²⁺ | Zn ²⁺ |
| | 0.602 | 0.595 | 0.731 | 0.646 | 0.847 | 0.702 | 0.651 | 0.906 | 0.655 |
| B | Cu ²⁺ | Pb ²⁺ | Zn ²⁺ | Cu ²⁺ | Pb ²⁺ | Zn ²⁺ | Cu ²⁺ | Pb ²⁺ | Zn ²⁺ |
| | 0.418 | 0.633 | 0.665 | 0.738 | 0.792 | 0.731 | 0.744 | 0.923 | 0.692 |
| C | Cu ²⁺ | Pb ²⁺ | Zn ²⁺ | Cu ²⁺ | Pb ²⁺ | Zn ²⁺ | Cu ²⁺ | Pb ²⁺ | Zn ²⁺ |
| | 0.599 | 0.783 | 0.704 | 0.659 | 0.769 | 0.675 | 0.642 | 0.873 | 0.708 |
| D | Cu ²⁺ | Pb ²⁺ | Zn ²⁺ | Cu ²⁺ | Pb ²⁺ | Zn ²⁺ | Cu ²⁺ | Pb ²⁺ | Zn ²⁺ |
| | 0.649 | 0.736 | 0.689 | 0.611 | 0.769 | 0.671 | 0.639 | 0.843 | 0.728 |
| Best Group | Cu ²⁺ | | | Pb ²⁺ | | | Zn ²⁺ | | |
| | A ₃ B ₃ C ₂ D ₁ | | | A ₃ B ₃ C ₃ D ₃ | | | A ₁ B ₂ C ₃ D ₃ | | |

Table 4. Anova table of modified peanut shells

| Variance Source | Factors | | | | | | | | | | | |
|-----------------|---|------------------|------------------|------------------|------------------|------------------|------------------|------------------|------------------|------------------|------------------|------------------|
| | A | | | B | | | C | | | D | | |
| SS | Cu ²⁺ | Pb ²⁺ | Zn ²⁺ | Cu ²⁺ | Pb ²⁺ | Zn ²⁺ | Cu ²⁺ | Pb ²⁺ | Zn ²⁺ | Cu ²⁺ | Pb ²⁺ | Zn ²⁺ |
| | 0.004 | 0.164 | 0.009 | 0.209 | 0.127 | 0.007 | 0.006 | 0.049 | 0.002 | 0.002 | 0.018 | 0.005 |
| Df | Cu ²⁺ | Pb ²⁺ | Zn ²⁺ | Cu ²⁺ | Pb ²⁺ | Zn ²⁺ | Cu ²⁺ | Pb ²⁺ | Zn ²⁺ | Cu ²⁺ | Pb ²⁺ | Zn ²⁺ |
| | 2 | 2 | 2 | 2 | 2 | 2 | 2 | 2 | 2 | 2 | 2 | 2 |
| MS | Cu ²⁺ | Pb ²⁺ | Zn ²⁺ | Cu ²⁺ | Pb ²⁺ | Zn ²⁺ | Cu ²⁺ | Pb ²⁺ | Zn ²⁺ | Cu ²⁺ | Pb ²⁺ | Zn ²⁺ |
| | 0.072 | 1.832 | 1.565 | 3.783 | 1.419 | 1.217 | 0.109 | 0.547 | 0.348 | 0.036 | 0.201 | 0.870 |
| F-value | Cu ²⁺ | Pb ²⁺ | Zn ²⁺ | Cu ²⁺ | Pb ²⁺ | Zn ²⁺ | Cu ²⁺ | Pb ²⁺ | Zn ²⁺ | Cu ²⁺ | Pb ²⁺ | Zn ²⁺ |
| | 4.460 | 4.460 | 4.460 | 4.460 | 4.460 | 4.460 | 4.460 | 4.460 | 4.460 | 4.460 | 4.460 | 4.460 |
| Significance | Cu ²⁺ | Pb ²⁺ | Zn ²⁺ | Cu ²⁺ | Pb ²⁺ | Zn ²⁺ | Cu ²⁺ | Pb ²⁺ | Zn ²⁺ | Cu ²⁺ | Pb ²⁺ | Zn ²⁺ |
| Note | Error: Cu ²⁺ : 0.22, 8; Pb ²⁺ : 0.36, 8; Zn ²⁺ : 0.02, 8; \ —non-significance. | | | | | | | | | | | |

Table 5. Reaction kinetics parameters of unmodified peanut shells

| Adsorbent | Initial ion concentration | Apparent first order | | Apparent second order | |
|--------------------------|---------------------------|----------------------|--------|-----------------------|----------------|
| | | k1 | r1 | k2 | r ² |
| Unmodified peanut shells | Pb ²⁺ (40mg/L) | 0.0257 | 0.3769 | 0.4277 | 0.9947 |
| | Cu ²⁺ (40mg/L) | 0.0397 | 0.6709 | 0.4630 | 0.9987 |
| | Zn ²⁺ (40mg/L) | 0.0319 | 0.2885 | 0.1145 | 0.9976 |
| | Pb ²⁺ (50mg/L) | 0.0527 | 0.7279 | 0.1304 | 0.9993 |
| | Cu ²⁺ (50mg/L) | 0.0524 | 0.3590 | 0.4402 | 0.9932 |
| | Zn ²⁺ (50mg/L) | 0.0234 | 0.2510 | 0.3375 | 0.9867 |

Table 6. Reaction kinetics parameters of modified peanut shells

| Adsorbent | Initial ion concentration | Apparent first order | | Apparent second order | |
|------------------------|---------------------------|----------------------|--------|-----------------------|----------------|
| | | k1 | r1 | k2 | r ² |
| Modified peanut shells | Pb ²⁺ (30mg/L) | 0.0361 | 0.7412 | 0.1264 | 0.9707 |
| | Cu ²⁺ (30mg/L) | 0.0289 | 0.7508 | 0.0423 | 0.9715 |
| | Zn ²⁺ (30mg/L) | 0.0321 | 0.5385 | 0.1465 | 0.8934 |
| | Pb ²⁺ (50mg/L) | 0.0922 | 0.9178 | 0.0613 | 0.9961 |
| | Cu ²⁺ (50mg/L) | 0.0423 | 0.8610 | 0.1645 | 0.9863 |
| | Zn ²⁺ (50mg/L) | 0.0276 | 0.5499 | 0.1096 | 0.9615 |

Dynamics analysis

The process and dynamical behavior of adsorption of metal ions (Pb²⁺, Cu²⁺, Zn²⁺) by peanut shells was consistent with the Lagergren apparent second-order kinetic model as shown in Table 5 and Table 6, which indicated that the physical adsorption and the biological adsorption of heavy metals happened simultaneously which coincided with many previous reports. Under the optimum condition, the average absolute deviation rate of the equilibrium adsorption amount from the Lagergren apparent first-order kinetic model (q_{e, cal}) and experiments (q_{e, exp}) was relatively large, while the one from Lagergren apparent second-order kinetic model (q_{e, cal}) and experiments (q_{e, exp}) was much smaller. Therefore, the apparent second-order adsorption dynamics model better

describes the adsorption process under the optimum condition. Moreover, the apparent second-order adsorption dynamics model was more suitable for the system when reached equilibrium after a much longer time with q_e unknown.

Infrared spectrum (IR) analysis

As stated in Fig. 5 and Fig. 6, the infrared absorption spectra of unmodified and modified peanut shells is similar, which indicates that the hydrochloric acid modification does not have a great influence on the chemical properties of peanut shells.

The absorption peak of modified peanut shells broadened at 3420 cm⁻¹ and 1050 cm⁻¹ and the absorption intensity increased at 1640 cm⁻¹ and 1510 cm⁻¹.

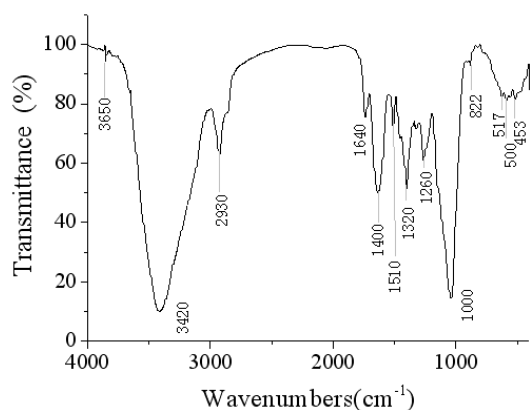


Fig. 5. Infrared spectrum of unmodified peanut shells

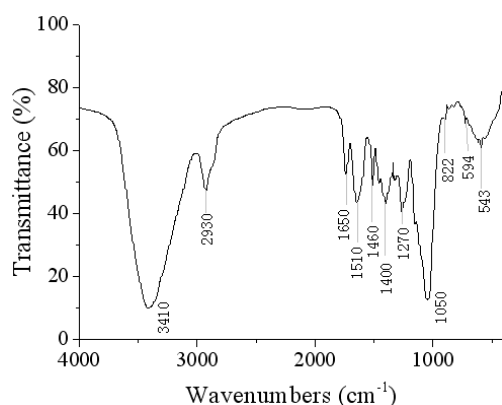


Fig. 6. Infrared spectrum of modified peanut shells.

A strong absorption peak at 3420 cm^{-1} was stretching the vibration absorption peak of unsaturated hydrocarbon together with a small amount of the amino group; the peak at 2930 cm^{-1} was an asymmetric stretching vibration of methylene; the peak at 1640 cm^{-1} was a stretching vibration absorption peak of carbonyl; the peak at 1510 cm^{-1} was likely to be an anti-symmetric stretching vibration absorption peak of the ester group from carboxylate; the peak at 1270 cm^{-1} was a plane vibration absorption peak of hydroxy from cellulose; the peak at 1050 cm^{-1} was a vibration absorption peak of polysaccharide backbone, which is mainly caused by stretching the vibration of C-OH from sugars or P-O-C.

CONCLUSION

Peanut shells have the ability to adsorb Pb^{2+} , Cu^{2+} and Zn^{2+} ions which could be influenced by factors such as the adsorption reaction duration, the initial ion concentration, dosage of the samples and the pH value. The adsorption rate grew with the increase of the pH value, the reaction duration and the adsorbent dosage, while the adsorption rate decreased with the initial rise in ion concentration. The study indicated that the adsorption of metal ions by peanut shells is completed within a short time. The effect of the recommended factors on the

adsorption was not obvious and the dynamical behavior of unmodified and modified peanut shells was more suitable for the Lagergren second-order kinetic model. The maximum adsorption rates of unmodified peanut shells for Pb^{2+} , Cu^{2+} , Zn^{2+} were 99.8%, 77.6%, 72.3%, respectively, while the maximum adsorption rates of modified peanut shells for Pb^{2+} , Cu^{2+} , Zn^{2+} were 97.6%, 80.3%, 77.1%, respectively. In a word, the absorption efficiency of modified peanut shells was higher than that of unmodified shells. Meanwhile, the adsorption efficiency of modified peanut shells was increased and further optimized.

So far, enormous progress has been made in the study of the adsorption of heavy metal ions. The experiments showed that the adsorption by agricultural and forestry waste is an effective method for removing heavy metals from wastewater, but its industrial introduction was slow and the study and development of the adsorption carriers need more hard work. There were various factors affecting the adsorption efficiency which should be further discussed, such as the modification methods and characteristics of the absorbing materials, desorption conditions of the adsorption materials and the recycling of heavy metal ions together with the regeneration and repeated utilization of the adsorbent. The influence of the coexisting cations on the adsorption process should be taken into consideration if the solution is a mixture of metals. In order to put adsorption of heavy metals into applications more efficiently, we should focus on the adsorption mechanism, the regeneration of biological adsorbent, reuse of industrial sewage, and establishment of a better adsorption technical process in the next stage.

Acknowledgments: This research was supported by the Special Scientific Research Fund of the Agricultural Public Welfare Profession of China (No. 201203042, 201403048-8), Science and Technology Innovation Projects of CAAS (No. CAAS-ASTIP-2014-LIHPS-08), Chinese National Natural Science Foundation (No. 31460032), Natural Science Foundation of Gansu Province (No. 1212RJYA008, 1308RJZA287), and the Foundation of Excellent Young Teachers of LUT (No. 10-061406).

REFERENCES

1. C.S. Zhu, L.P. Wang, W.B. Chen, *Journal of Hazardous Materials*, **168**(2-3), 739 (2009).
2. C.X. Wu, Q.H. Wu, C. Wang, Z. Wang, *Chinese Chemical Letters*, **22**, 473 (2011).

3. A. Schutz, M. Olsson, A. Jensen, L. Gerhardsson, J. Borjesson, S. Mattsson, S. Skerfving, *Int Arch Occup Environ Health*, **78**, 35 (2005).
4. M. Sallmén, M.L. Lindbohm, Anttila A, Taskinen H, Hemminki K, *Epidemiology*, **11**(2), 141 (2000).
5. Y.H. Huang, C.L. Hsueh, H.P. Cheng, L.C. Su, C.Y. Cheng, *Journal of Hazardous Materials*, **144**(1-2), 406 (2007).
6. S. Dhiraj, M. Garima, M.P. Kaur, *Bioresource Technology*, **99**(14), 6017 (2008)
7. W.S.W. Ngah, M.A. Hanafiah, *Bioresource Technology*, **99**(10), 3935 (2008).
8. A.W. Krowiak, R.G. Szafran, S. Modelski, *Desalination*, **265**, 126 (2011).
9. S. Ricordel, S. Taha, I. Cisse, G. Dorange, *Separation and Purification Technology*, **24**(3), 389 (2001).
10. S.H. Zhao, Z.L. Chen, T.P. Zhang, W.B. Pan, X.C. Peng, R. Che, Y.J. Ou, G.J. Lei, D. Zhou, *Huan Jing Ke Xue*, **35**(4), 1548 (2014).
11. P.D. Johnson, M.A. Watson, J. Brown, I.A. Jefcoat, *Waste Management*, **22**(5), 471 (2002).
12. Q. Li, J.P. Zhai, W.Y. Zhang, M.M. Wang, J. Zhou, *Journal of Hazardous Materials*, **141**(1), 163 (2007).
13. S.B. Deng, B.Y. Hu, T. Chen, B. Wang, J. Huang, Y.J. Wang, G. Yu, *Adsorption*, **21**, 125 (2015).

МОДИФИЦИРАНЕ НА ШЛЮПКИ ОТ ФЪСТЪЦИ И ТЯХНОТО ПРИЛОЖЕНИЕ ЗА АДСОРБЦИЯ НА ТЕЖКИ МЕТАЛИ

З. Янг¹, И.Г. Уанг^{1,3,4}, И.Дж. Джинг^{3,4}, К.У. Уей^{3,4}, Ф.Ф. Ленг^{3,4}, Х. Ма^{3,4}, И.Л. Уанг^{3,4}, Дж. Кс. Чен^{1,2}

¹Училище по енергия и енергетика, Ланджоу университет по технологии, Ланджоу 730050, Китай

²Училище по нефтохимическо инженерство, Ланджоу Университет по технологии, Ланджоу 730050, Китай

³Училище по инженерство и науки за живота, Технологичен университет Ланджоу, Ланджоу 730050, Китай

⁴Стопански институт за фармация в Ланджоу, Китайска академия за селскостопански науки, Ланджоу 730050, Китай

Постъпила на 13 юни, 2016 г.; приета на 26 юли, 2016 г.

(Резюме)

Шлюпките от фъстъци са пробен материал за адсорбция. Изследвана е способността им да адсорбират тежки метали (Pb^{2+} , Cu^{2+} и Zn^{2+}) в зависимост от различни фактори (рН, времетраене на пиролизата, начална концентрация, доза). Резултатите показват, че адсорбцията на тежките метали расте с повишаването на рН. Беше установено, че адсорбцията на йоните на тежки метали върху не-модифицирани шлюпки протича добре в кисела среда, докато при модифицираните това е в алкална среда. Степента на адсорбция достига 88% от максималната след 15 минути с тенденция към равновесие след 50 мин. Степента на адсорбция расте с нарастване на концентрацията на металните йони, като максимумът се достига при 30 mg/L, а след това тя намалява.

Динамичното отнасяне както на модифицираните, така и на не-модифицираните шлюпки добре се описват от модела на Lagergren за химична кинетика на реакция от 2-ри порядък. Адсорбционният ефект на модифицираните шлюпки е много по-добър от не-модифицираните.

Generalized atom-bond connectivity analysis of several chemical molecular graphs

W. Gao^{1*}, W. F. Wang², M. K. Jamil³, R. Farooq⁴, M. R. Farahani⁵

¹ School of Information Science and Technology, Yunnan Normal University, Kunming 650500, China

² Department of Mathematics, Zhejiang Normal University, Jinhua 321004, China

³ Department of Mathematics, Riphah Institute of Computing and Applied Sciences, Riphah International University, 14 Ali Road, Lahore, Pakistan

⁴ School of Natural Sciences, National University of Sciences and Technology, H-12 Islamabad, Pakistan

⁵ Department of Applied Mathematics of Iran University of Science and Technology, Narmak, Tehran 16844, Iran

Received June 15, 2016; Accepted July 10, 2015

Lots of drug tests show strong inner relationships between the bio-medical and pharmacological characteristics of the drugs and their molecular structures. Due to the effectiveness for pharmaceutical and medical scientists of their ability to grasp the biological and chemical characteristics of new drugs, the generalized atom-bond connectivity index was defined to analyze the drug molecular structures. The analysis should find widespread application prospects in developing countries, especially in poor places without the adequate financial ability and affordability of much needed chemical reagents and equipment. In this paper, based on the drug molecular structure analysis and driving edge technology, we propose the generalized atom-bond connectivity index of several popular chemical structures which is quite common in drug molecular graphs.

Keywords Computational chemical; Generalized atom-bond connectivity index; dendrimer stars; bridge graph; benzenoid series

INTRODUCTION

A wide range of new drugs emerge each year with the rapid development of the manufacture of medicines. Therefore, lots of work is needed to determine the pharmacological, chemical and biological characteristics of these new drugs. The relevant reagent equipment and lab assistants are in demand in order to test the performance and side effects of these new drugs. However, in some poor areas (such as the countries in South America, Africa and Southeast Asia), they are not rich enough to afford the reagents and equipment necessary to assess the biochemical properties. Luckily, we can refer to the contributions of relevant previous studies, for example, the chemical and pharmacodynamics characteristics of the drugs and their molecular structures as these are closely linked. Once the indicators of these drug molecular structures are calculated in view of defining their topological indices, these can be used to understand their medical properties and help to repair and make up for all the defects of the medicine following the chemical experiments. From this point of view, we can appreciate the effectiveness of the methods on the topological index of computation especially for developing countries, where the available biological and medical infor-

mation about new drugs may be easily obtained without the need to carry out chemical experiments and purchase expensive hardware.

Traditionally, we look upon the structure of a drug as an undirected graph in the mathematical model of a given medicine. Each vertex represents an atom in the graph and the chemical bond between these atoms is represented by each edge. We consider G as a simple graph corresponding to a drug structure with an atom (vertex) set as $V(G)$ and a chemical bond (edge) set as $E(G)$. A topological index defined on the molecule structure G can be regarded as a real-valued function $f: G \rightarrow R^+$ which maps each drug molecular structure to certain real numbers. Decades ago, scientists introduced significant indices, including the Wiener index, the PI index, the Zagreb index and the eccentric index, to measure the characters of the drug molecules. Some reports help to determine these topological indices of special molecular graphs in chemical, nanomaterials and pharmaceutical engineering (See Yan et al. [1], Gao et al. [2-3], Gao and Farahani [4-5], Gao and Shi [6], and Gao and Wang [7-10] for more detail). The referred notations and terminologies without clear explanations can be found in Bondy and Murty [11].

Furtula et al. [12] defined the generalized version of the atom-bond connectivity index which was defined as:

* To whom all correspondence should be sent:

E-mail: gaowei@ynnu.edu.cn

$$ABC_{\lambda}(G) = \sum_{uv \in E(G)} \left(\frac{d(u) + d(v) - 2}{d(u)d(v)} \right)^{-\lambda},$$

where $\lambda < 0$. Clearly, taking $\lambda = -\frac{1}{2}$, it becomes

the atom-bond connectivity index defined by Estrada et al. [13]. Also, Furtula et al. [12] introduced the augmented Zagreb index which was denoted as:

$$AZI(G) = \sum_{uv \in E(G)} \left(\frac{d(u)d(v)}{d(u) + d(v) - 2} \right)^3.$$

Obviously, the augmented Zagreb index is a special case of the generalized atom-bond connectivity index when $\lambda=3$.

Despite the contributions to the distance-based indices and degree-based molecular structures, the researches of the generalized atom-bond connectivity index for certain special drug structures still await further studies. As a consequence, the research on the generalized atom-bond connectivity index of the drug molecular structure from a mathematical point of view are becoming more and more heated with the years with more and more academic and industrial interest drawn from a variety of fields.

Respectively, we designate $\delta(G)$ and $\Delta(G)$ to be the minimum and maximum degrees of G . The edge set $E(G)$ can be categorized into different parts: for any i and j , $\delta(G) \leq i, j \leq \Delta(G)$, let $E_{ij} = \{e=uv \in E(G) \mid d(v)=i, d(u)=j\}$ and $n_{ij} = |E_{ij}|$.

In this paper, we obtain the generalized atom-bond connectivity index of several important chemical structures with a high frequency in drug structures.

MAIN RESULTS

The generalized atom-bond connectivity index of graphene $G(m, n)$

Graphene, a two-dimensional material, is a planar sheet of carbon atoms. It is usually densely packed in a honeycomb crystal lattice and also the main element of certain carbon allotropes including charcoal, fullerenes and graphite, please refer to Figure 1.

Theorem 1. Let $G(m, n)$ be a graphene sheet with n rows and m columns. We obtain:

$$ABC_{\lambda}(G(m, n)) =$$

$$\begin{cases} (4m+3n)\left(\frac{1}{2}\right)^{-\lambda} + \left\lfloor \frac{n}{2} \right\rfloor (5m+1) + \left\lfloor \frac{n}{2} \right\rfloor (m+3) \left(\frac{4}{9}\right)^{-\lambda}, & n \equiv 1(\text{mod } 2) \\ (4m+3n)\left(\frac{1}{2}\right)^{-\lambda} + \left\lfloor \frac{n}{2} \right\rfloor (5m+1) + \left\lfloor \frac{n}{2} \right\rfloor (m+3) + 2m-1 \left(\frac{4}{9}\right)^{-\lambda}, & n \equiv 0(\text{mod } 2) \end{cases}$$

Proof. Based on the structure analysis, we obtain:

$$\begin{aligned} |E(G(m, n))| &= \\ \begin{cases} \left\lfloor \frac{n}{2} \right\rfloor (5m+1) + \left\lfloor \frac{n}{2} \right\rfloor (m+3), & n \equiv 1(\text{mod } 2) \\ \left\lfloor \frac{n}{2} \right\rfloor (5m+1) + \left\lfloor \frac{n}{2} \right\rfloor (m+3) + 2m-1, & n \equiv 0(\text{mod } 2) \end{cases} \end{aligned}$$

After further calculation, we get $n_{22} = n + 4$, $n_{23} = 4m + 2n - 4$, and

$$n_{33} = |E(G(m, n))| - 4m - 3n.$$

As a result, according to the definition of the generalized atom-bond connectivity index, we obtain the expected result.

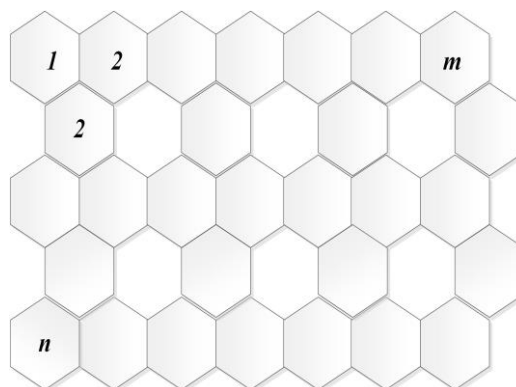


Fig. 1. 2-Dimensional graph of a graphene sheet

Generalized atom-bond connectivity index of three family of dendrimer stars

In this section, three famous infinite classes $NS_1[n]$, $NS_2[n]$ and $NS_3[n]$ of dendrimer stars are defined and they are common in the drug structures.

Theorem 2. Let n be the number of steps of growth in this type of dendrimer stars. We indicate

$$\begin{aligned} ABC_{\lambda}(NS_1[n]) &= (27 \cdot 2^n - 9) \left(\frac{1}{2}\right)^{-\lambda} \\ &\quad + \left(\frac{2}{3}\right)^{-\lambda} + 3 \left(\frac{5}{12}\right)^{-\lambda}, \\ ABC_{\lambda}(NS_2[n]) &= (36 \cdot 2^n - 6) \left(\frac{1}{2}\right)^{-\lambda} + \left(\frac{4}{9}\right)^{-\lambda}, \\ ABC_{\lambda}(NS_3[n]) &= \\ &= (50 \cdot 2^n - 13) \left(\frac{1}{2}\right)^{-\lambda} + 2^{n+1} \left(\frac{2}{3}\right)^{-\lambda} + 6 \cdot 2^n \left(\frac{4}{9}\right)^{-\lambda}. \end{aligned}$$

Proof. After the observation to the structures

of these three dendrimer stars, we present its edge dividing below:

- for $NS_1[n]$: $n_{23} = 18 \cdot 2^n - 12$,
 $n_{22} = 9 \cdot 2^n + 3$, $n_{13} = 1$ and $n_{34} = 3$;
- for $NS_2[n]$: $n_{23} = 24 \cdot 2^n - 8$,
 $n_{22} = 12 \cdot 2^n + 2$ and $n_{33} = 1$;
- for $NS_3[n]$: $n_{23} = 28 \cdot 2^n - 6$,
 $n_{22} = 22 \cdot 2^n - 7$, $n_{33} = 6 \cdot 2^n$ and $n_{13} = 2^{n+1}$.

Hence, with the reference to the definition of the generalized atom-bond connectivity index, we obtain the expected result.

Generalized atom-bond connectivity index of polyomino chains of n-cycles and triangular benzenoid

In the field of mathematics, a polyomino system, an edge-connected union of cells, is a finite 2-connected plane graph where each interior face (i.e. cell) is encircled by a C_4 . More details can be found in Klarnar [14] and Ghorbani and Ghazi [15]. For instance, the polyomino chains of 8-cycles can be represented in Figure 2.

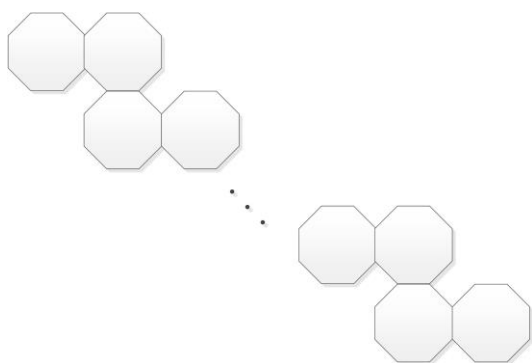


Fig. 2. The zig-zag chain of 8-cycles.

Theorem 3. Let G be a molecular graph as described above. We have

$$ABC_\lambda(G) = (20n + 4)\left(\frac{1}{2}\right)^{-\lambda} + (8n - 3)\left(\frac{4}{9}\right)^{-\lambda}.$$

Proof. Based on the structure analysis, we infer $n_{22} = 12n + 4$, $n_{23} = 8n$, and $n_{33} = 8n - 3$.

Therefore, considering the definition of the generalized atom-bond connectivity index, we get the expected result.

Next, the generalized atom-bond connectivity index of a triangular benzenoid molecular graph $T(n)$ is computed and the structure is described in Figure 3.

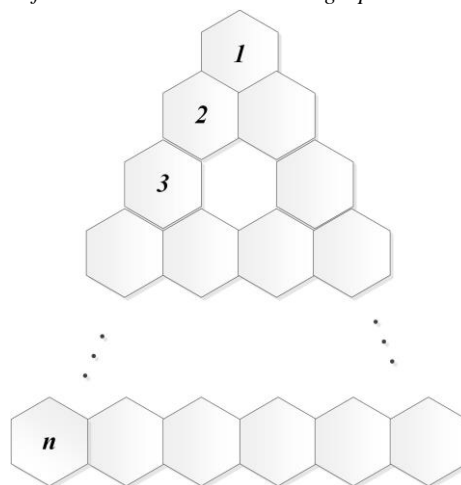


Fig. 3. Molecular graph of a triangular benzenoid $T(n)$

Theorem 4. Let $T(n)$ denote a triangular benzenoid. We get

$$ABC_\lambda(T(n)) = \frac{3n^2 - 3n + 12}{2} \left(\frac{1}{2}\right)^{-\lambda} + (6n - 6) \left(\frac{4}{9}\right)^{-\lambda}.$$

Proof. Based on the edge dividing technology, we get $n_{22} = 6$, $n_{23} = \frac{3n(n-1)}{2}$, and $n_{33} = 6(n-1)$. Hence, concerning the definition of the generalized atom-bond connectivity index, we obtain the result.

Generalized atom-bond connectivity index of bridge molecular structures

Let's consider $\{G_i\}_{i=1}^d$ a set of finite pairwise disjoint molecular graphs with $v_i \in V(G_i)$. The bridge molecular graph $B(G_1, \dots, G_d) = B(G_1, \dots, G_d; v_1, \dots, v_d)$ of $\{G_i\}_{i=1}^d$ regarding the vertices $\{v_i\}_{i=1}^d$ is acquired from the molecular graphs G_1, \dots, G_d where the vertices v_i and v_{i+1} are linked through an edge for $i=1, 2, \dots, d-1$. As a result, this section helps to determine the formulas of some degree based indices for the infinite family of drug structures of the bridge molecular graph with G_1, \dots, G_d (see Figure 4). Then we define $G_d(H, v) = B(H, \dots, H, v, \dots, v)$ for special situations of the bridge molecular graphs.

We analyze the bridge graphs as follows and the main parts of the graphs are path, cycle and complete molecular graph, respectively.

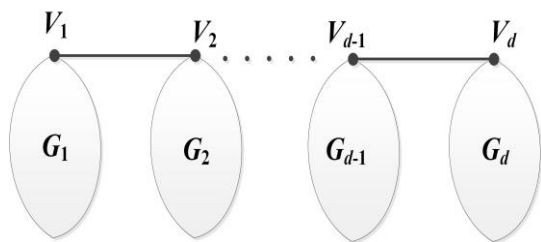


Fig. 4. The bridge molecular graph.

- Let P_n be the path with n vertices. We have dn vertices and $dn-1$ edges for the bridge molecular graph $G_d(P_n, v)$ (see Figure 5 for more details). Moreover, the edge set of the bridge graph $G_d(P_n, v)$ can be categorized into four parts: $n_{22} = d(n-3) + 2$, $n_{23} = n_{12} = d$, and $n_{33} = d - 3$.

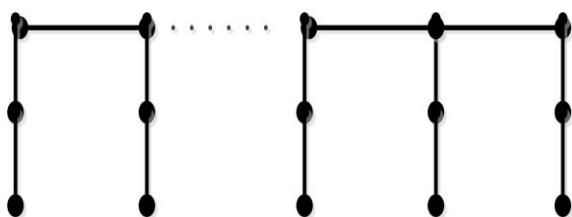


Fig. 5. The bridge molecular graph $G_d(P_n, v)$.

- Let C_n be the cycle with n vertices. We get dn vertices and $dn+d-1$ edges for the bridge molecular graph $G_d(C_n, v)$ (see Figure 6 for more details). Moreover, the edge set of the bridge molecular graph $G_d(C_n, v)$ can be categorized into five parts: $n_{22} = d(n-2)$, $n_{23} = 4$, $n_{24} = 2d-4$, $n_{34} = 2$ and $n_{44} = d-3$.

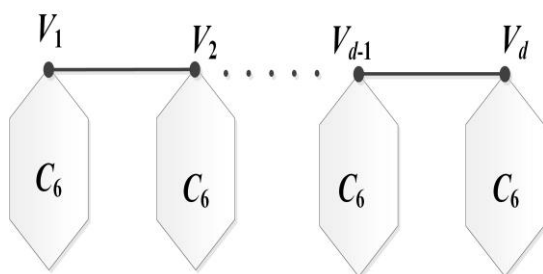


Fig. 6. The bridge molecular graph $G_d(C_n, v)$.

- Let K_n be a complete molecular graph with n vertices. We get dn vertices and $\frac{dn(n-1)}{2} + d - 1$ edges for the bridge molecular graph $G_d(K_n, v)$ (see Figure 7, $G_d(K_3, v)$ as an example). Moreover, the edge set of the bridge

molecular graph $G_d(K_n, v)$ can be categorized into five partitions: $n_{55} = n_{5(n-1)} = d - 2$, $n_{45} = n_{4(n-1)} = 2$ and $n_{(n-1)(n-1)} = \frac{d(n-1)(n-2)}{3}$.

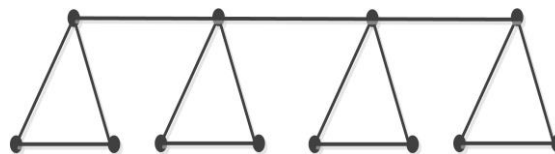


Fig. 7. The bridge molecular graph $G_d(K_3, v)$.

In view of the definition of the generalized atom-bond connectivity index, the main result of this section is obtained and represented below. The detailed proofs are omitted here.

Theorem 5.

$$\begin{aligned}
 ABC_\lambda(G_d(P_n, v)) &= d(n-1)\left(\frac{1}{2}\right)^{-\lambda} + (d-3)\left(\frac{4}{9}\right)^{-\lambda}, \\
 ABC_\lambda(G_d(C_n, v)) &= \\
 &dn\left(\frac{1}{2}\right)^{-\lambda} + (d-3)\left(\frac{3}{8}\right)^{-\lambda} + 2\left(\frac{5}{12}\right)^{-\lambda}, \\
 ABC_\lambda(G_d(K_n, v)) &= (d-2)\left(\frac{8}{25}\right)^{-\lambda} + 2\left(\frac{7}{20}\right)^{-\lambda} \\
 &+ 2\left(\frac{1}{4}\right)^{-\lambda} + (d-2)\left(\frac{n+2}{5(n-1)}\right)^{-\lambda} \\
 &+ \frac{d(n-1)(n-2)}{3} \left(\frac{2n-4}{(n-1)^2}\right)^{-\lambda}.
 \end{aligned}$$

Generalized atom-bond connectivity index of the carbon tube networks

In this section, we place emphasis on the $m \times n$ quadrilateral section P_m^n with $m \geq 2$ hexagons on the top and bottom sides and $n \geq 2$ hexagons on the lateral sides cut from the regular hexagonal lattice, refer to Figure 8 to observe the detailed chemical structure.

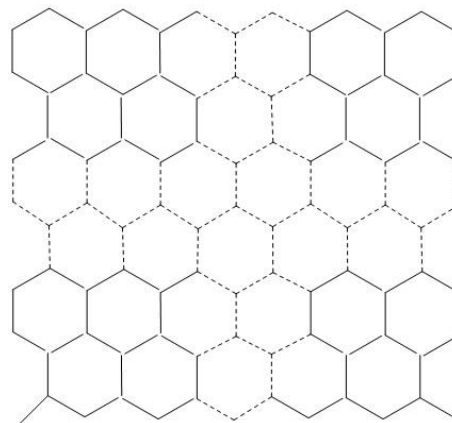


Fig. 8 Quadrilateral section P_m^n cuts from the regular hexagonal lattice.

The tube NA_m^n with $2m(n+1)$ vertices and $(3n+2)m$ edges is obtained by identifying two lateral sides of P_m^n by identifying the vertices u_i^j and u_m^j ($j=0,1,\dots,n$).

Let $n \in \mathbb{N}$ be even so that $n, m \geq 2$. The tube NC_m^n of order $n(2m+1)$ with size $n(3m + \frac{1}{2})$ can be obtained if we identify the top and bottom sides of the quadrilateral section P_m^n in a similarly way in which the vertices u_i^0 and u_i^n for $i=0,1,\dots,m$ and vertices v_i^0 and v_i^n for $i=0,1,\dots,m$ are identified. See Baca et al. [16] for more details.

Theorem 6.

$$ABC_\lambda(NA_m^n) = 4m(\frac{1}{2})^{-\lambda} + m(3n-2)(\frac{4}{9})^{-\lambda},$$

$$ABC_\lambda(NC_m^n) = 3n(\frac{1}{2})^{-\lambda} + n(3m - \frac{5}{2})(\frac{4}{9})^{-\lambda}.$$

Proof. For tube NA_m^n , we derive $n_{23} = 4m$, and $n_{33} = m(3n-2)$. For tube NC_m^n , we derive $n_{22} = n$, $n_{23} = 2n$, and $n_{33} = n(3m - \frac{5}{2})$. Hence, in accordance with the definition of the for the generalized atom-bond connectivity index, we obtain the desired result.

Generalized atom-bond connectivity index of dendrimer stars $D_3[n]$

In this section, an essential chemical structure $D_3[n]$ is analyzed. It describes the n -th growth of star dendrimer for $\forall n \in \mathbb{N} \cup \{0\}$. Refer to Figure 9 for more details on the structure of this chemical molecular graph which is quite common in drug structures.

Based on the analysis in Farahani [17], we know that $E(D_3[n])$ can be divided into four parts: $n_{13} = 3 \cdot 2^n$, $n_{22} = 6(2^{n+1} - 1)$, $n_{23} = 12(2^{n+1} - 1)$, and $n_{33} = 9 \cdot 2^n - 6$. Hence, we get the conclusion described below for these molecular structures.

Theorem 7. $ABC_\lambda(D_3[n]) = 3 \cdot 2^n (\frac{2}{3})^{-\lambda} + 18(2^{n+1} - 1)(\frac{1}{2})^{-\lambda} + (9 \cdot 2^n - 6)(\frac{4}{9})^{-\lambda}.$

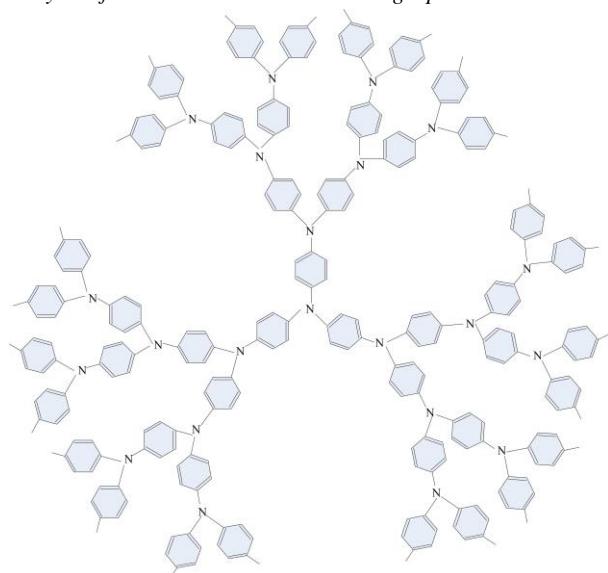


Fig. 9. The 2-Dimensional of the n -th growth of star dendrimer $D_3[n]$.

Generalized atom-bond connectivity index of two classes of benzenoid series

In this section, we plan to determine the generalized atom-bond connectivity index of two classes of benzenoid series.

First, the circumcoronene series of benzenoid H_k is concerned. While $k=1, 2, 3$, the structures are presented in Figure 10.

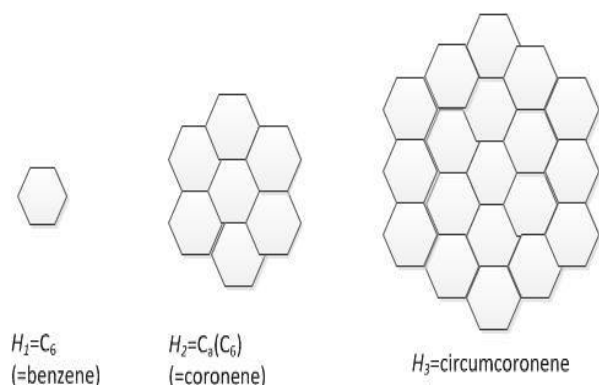


Fig. 10. The first, second and third molecular graphs H_1, H_2 and H_3 from the circumcoronene series of benzenoid.

Hence, the family of circumcoronene homologous series of benzenoid is made up of some copies of benzene C_6 on circumference, for more details of this structure, please refer to Figure 11.

OTHER CONCLUSIONS

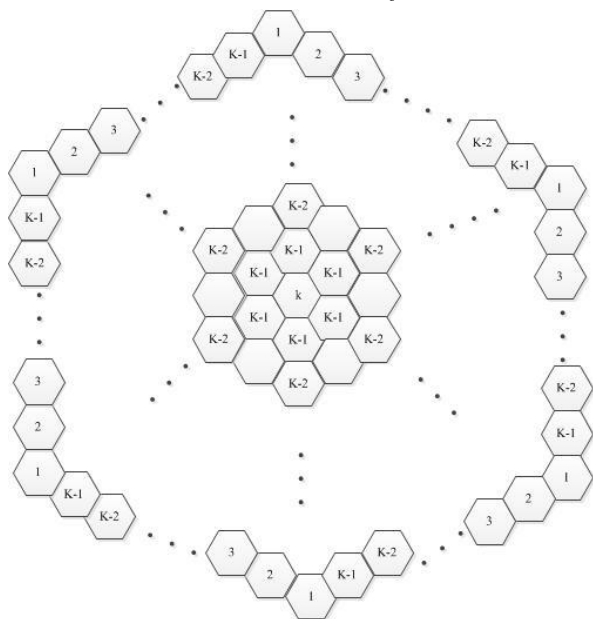


Fig. 11. The circumcoronene series of benzenoid H_k for $k \geq 1$.

Theorem 8.

$$ABC_\lambda(H_k) = (12k - 6)\left(\frac{1}{2}\right)^{-\lambda} + (9k^2 - 15k + 6)\left(\frac{4}{9}\right)^{-\lambda}.$$

Proof. Consider the circumcoronene series of benzenoid H_k for $k \geq 1$. It is not hard to check that $|V(H_k)| = 6k^2$ and $|E(H_k)| = 9k^2 - 3k$. Moreover, we deduce $n_{33} = 9k^2 - 15k + 6$, $n_{23} = 12(k - 1)$, and $n_{22} = 6$. Thus, regarding the definition of the generalized atom-bond connectivity index, we indicate the result.

Next, the capra-designed planar benzenoid series $Ca_k(C_6)$ (the structure can be referred to Farahani and Vlad [18] for more details) is considered. By means of the intermediate results presented in Farahani and Vlad [18], we present the generalized atom-bond connectivity index of $Ca_k(C_6)$ which is stated as follows.

Theorem 9.

$$ABC_\lambda(Ca_k(C_6)) = (5 \cdot 3^k + 3)\left(\frac{1}{2}\right)^{-\lambda} + (3 \cdot 7^k - 2 \cdot 3^k - 3)\left(\frac{4}{9}\right)^{-\lambda}.$$

Proof. Based on the analysis of the molecular structure of $Ca_k(C_6)$, we check that the edge set of $Ca_k(C_6)$ can be divided into three partitions: $n_{22} = 3^k + 3$, $n_{23} = 4 \cdot 3^k$, and $n_{33} = 3 \cdot 7^k - 2 \cdot 3^k - 3$. Thus, using the definition of the generalized atom-bond connectivity index, we infer the desired result.

Finally, we present the generalized atom-bond connectivity index for the chemical structures discussed in Gao et al. [2].

Theorem 10. Let $SP[n]$ be the Dox-loaded micelle comprising a PEG-PAsp block copolymer with a chemically conjugated Dox. We obtain

$$ABC_\lambda(SP[n]) = (27n + 4)\left(\frac{1}{2}\right)^{-\lambda} + (9n + 1)\left(\frac{2}{3}\right)^{-\lambda} + n\left(\frac{3}{4}\right)^{-\lambda} + 16n\left(\frac{4}{9}\right)^{-\lambda} + n\left(\frac{5}{12}\right)^{-\lambda}.$$

Theorem 11. Let $D_2[n]$ and $D_4[n]$ be polyphenylene dendrimers with n stages. We have

$$ABC_\lambda(D_2[n]) = (104 \cdot 2^n - 92)\left(\frac{1}{2}\right)^{-\lambda} + (36 \cdot 2^n - 35)\left(\frac{4}{9}\right)^{-\lambda},$$

$$ABC_\lambda(D_4[n]) = (104 \cdot 2^n - 80)\left(\frac{1}{2}\right)^{-\lambda} + (36 \cdot 2^n - 36)\left(\frac{4}{9}\right)^{-\lambda} + 4\left(\frac{5}{12}\right)^{-\lambda}.$$

Theorem 12. Let S be a benzenoid system with n vertices, h hexagons and r inlets. We infer

$$ABC_\lambda(S) = (n - 2h + r + 2)\left(\frac{1}{2}\right)^{-\lambda} + (3h - r - 3)\left(\frac{4}{9}\right)^{-\lambda}.$$

Theorem 13. Let PH be phenylene. We deduce

$$ABC_\lambda(PH) = (2h + r + 4)\left(\frac{1}{2}\right)^{-\lambda} + (6h - r - 6)\left(\frac{4}{9}\right)^{-\lambda}.$$

Theorem 14. Let PAH_n be the Polycyclic Aromatic Hydrocarbons

$$ABC_\lambda(PAH_n) = 6n\left(\frac{2}{3}\right)^{-\lambda} + (9n^2 - 3n)\left(\frac{4}{9}\right)^{-\lambda}.$$

CONCLUSIONS

Accompanied by the contentiously emerging viruses, more and more unnamed diseases are found in the world at a high speed each year. This demands the development of more new drugs to treat them. The generalized atom-bond connectivity index was introduced to measure the medicinal properties of new drugs and it is quite welcome and popular in poor areas. In our paper, based on the detailed drug structure analysis and

edge dividing, we defined the generalized atom-bond connectivity index of certain molecular graphs which frequently appear in drug structures. As a result, the conclusions obtained in our paper show the promising prospects of these applications in pharmacy engineering.

Acknowledgements: We thank the reviewers for their constructive comments in improving the quality of this paper. This work was supported in part by NSFC (Nos.11401519 and 61262070).

REFERENCES

1. L. Yan, W. Gao, J. S. Li, *J. Comput. Theor. Nanosci.*, **12**(10), 3940 (2015).
2. W. Gao, M. R. Farahani, L. Shi, *Acta Med. Medit.*, **32**, 579 (2016).
3. W. Gao, M. K. Siddiqui, M. Imran, M. K. Jamil, M. R. Farahani, *Saudi Pharm. J.*, **24**(3), 258 (2016).
4. W. Gao, W. F. Wang, *Chaos Solitons Fract.*, **89**, 290 (2016).
5. W. Gao, M. R. Farahani, *Appl. Math. Nonlinear Sci.*, **1**(1), 94 (2016).
6. W. Gao, L. Shi, *IAENG Int. J. Appl. Math.*, **45**(2), 138 (2015).
7. W. Gao, W. F. Wang, *J. Diff. Eqs. Appl.*, ID:1197214, DOI:10.1080/10236198.2016.1197214
8. W. Gao, W. F. Wang, *J. Chem.*, Volume 2014, Article ID 906254, 8 pages, <http://dx.doi.org/10.1155/2014/906254>.
9. W. Gao, W. F. Wang, *Comput. Math. Meth. Med.*, Volume 2015, Article ID 418106, 10 pages, <http://dx.doi.org/10.1155/2015/418106>.
10. W. Gao, M. R. Farahani, *J. Nanotechnol.*, 2016, Article ID 3129561, 6 pages. <http://dx.doi.org/10.1155/2016/3129561>.
11. J. A. Bondy, U. S. R. Murty, *Graph Theory*, Springer, Berlin, 2008.
12. B. Furtula, A. Graovac, et al., *J. Math. Chem.*, **48**, 370 (2010).
13. E. Estrada, L. Torres, L. Rodriguez, I. Gutman, *Indian J. Chem.*, **37**(10), 849 (1998).
14. D. A. Klarner, Polyominoes. In: J. E. Goodman, J. O'Rourke, (eds.) *Handbook of Discrete and Computational Geometry*, 225-242. CRC Press, Boca Raton, 1997, Chapter 12.
15. M. Ghorbani, M. Ghazi, *Digest J. Nanomater. Biostruct.*, **5**(4), 1107 (2010).
16. M. Baca, J. Horvathova, et al., *Can. J. Chem.*, **93**(10), 1157 (2015).
17. M. R. Farahani, *Chem. Phys. Res. J.*, **6**(1), 27 (2013).
18. M. R. Farahani, M. P. Vlad, *Studia Ubb Chemia*, **LVIII**, 133 (2013).

ОБОБЩЕН АНАЛИЗ НА СВЪРЗАНАТА АТОМНА ВРЪЗКА С НЯКОЛКО МОЛЕКУЛНИ ГРАФИ

У. Гао^{1*}, У.Ф. Уанг², М.К. Джамил³, Р. Фарук⁴, М.Р. Фарахани⁵

¹ Училище по информатика и технология, Университет в Юнан, Кунминг 650500, Китай

² Департамент по математика, Университет в Жейджанг, Джинхуа 321004, Китай

³ Департамент по математика, Институт по компютърни и приложни науки „Рифа“, Международен университет „Рифа“, Лахор, Пакистан

⁴ Училище по естествени науки, Национален университет за наука и технологии, Исламабад, Пакистан

⁵ Департамент по приложна математика, Ирански университет за наука и технологии, Нармак, Техеран 16844, Иран

Постъпила на 15 юни, 2015 г.; приета на 28 юли, 2015 г.

(Резюме)

Много тестове върху лекарства показват силна взаимовръзка между био-медицинските и фармакологичните им характеристики с тяхна молекулна структура. С цел да се подобри възможността на изследователите в медицината и фармацията да оценят характеристиките на нови лекарства е дефиниран обобщен индекс на свързаната атомна връзка за анализа на молекулната структура на лекарствата. В тази работа се предлага обобщен индекс на атомните връзки на няколко известни структури, които са твърде сходни с молекулните графи на лекарствата.

Organic matter removal performance and mechanism in the constructed rapid infiltration system

W.L. Xu, Y.N. Yang*, J.Wang, M. Tang, Y.Jian, X.J. Pei

State Key Laboratory of Geohazard Prevention and Geoenvironment Protection, Chengdu University of Technology, Chengdu 610059, China

Received June 15, 2015; Accepted July 26, 2015

The Constructed Rapid Infiltration System (CRI system) finds application in engineering, however, the pollutant removal mechanism is still not clear, which limits its further promotion and application. The experiment of processing wastewater by building a CRI simulation column while studying the pollutant removal mechanism and performance showed: after the CRI system operated steadily, under operation mode 1, that the CRI system had a higher removal rate of Chemical Oxygen Demand (COD) and COD had been removed effectively in a CRI filter tank 0-100cm segment, with a removal rate of up to 77.8%, under operation mode 2, the CRI system has a relatively low removal rate of COD, with an average removal rate of only 59.1%. Filtration and adsorption was the first step in the removal of organic pollutants by the CRI system; organic matter was accumulated during the flooding period and oxidized and decomposed during the drying period in the CRI system, degradation of aerobe mater played an important role in the removal of organic matter by the CRI system; alternation of the wetting and drying operation mode facilitated COD removal. The study results enrich our theoretical knowledge of the CRI system and promote the application of the CRI system.

Key words: Organic matter; Removal performance; Mechanism; Constructed rapid infiltration system

INTRODUCTION

The Constructed Rapid Infiltration system (CRI system) employs a new biological wastewater treatment method, which is now becoming a hot spot of research and application in China. The CRI system finds application in engineering, however, its pollutant removal capacity and fundamentals are still insufficiently studied and limit further promotion. Therefore it is necessary to further study the migration, transformation and degradation rules and master the degradation mechanism of various pollutants in the CRI system [1-4]. This study will provide a theoretical basis to further promote and apply the CRI system by conducting the experimental processing of domestic wastewater by building a CRI simulation column in the laboratory as well as by analysis of the organic matter and removal performance.

MATERIALS AND METHODS

Building a CRI Simulation Column

A CRI simulation column was built in the laboratory. The main part of the CRI simulation column reactor consists of an organic glass column, the column height is 200cm, the internal diameter is 21cm, the filtering material consists of 90% of

natural sand + 5% of sand marble + 5% of zeolite sand, with at a height of 150cm, the 7 sampling ports are set 25cm from the top filtering material layer to the bottom filtering material layer: 1# sampling port, 2# sampling port, 3# sampling port, 4# sampling port, 5# sampling port, 6# sampling port and 7# sampling port were set at 0cm, 25cm, 50cm, 75cm, 100cm, 125cm and 150cm from the top filtering material layer, respectively. A water distribution pipe was fixed on the top of the filtering material of the CRI system, the wastewater enters the water distribution pipe and feeds the water to the CRI system after extraction by a water pump, the wastewater quantity is controlled with a flowmeter and the wastewater flows straight down in the CRI system where it is purified by trickling through the filtering material from top to bottom. Fig.1 shows the schematic diagram of the filter tank of the CRI simulation column.

Operation and Management of the CRI Simulation Column

The CRI simulation column was operated on July 10, 2009, the experimental water was domestic wastewater from the sewer of a student apartment. The experimental design hydraulic load was 1m/d; two intermittent water distribution modes were adopted, an operational mode 1: 4 times of waterdistribution per day, 0.5h for each time, every time the water distribution quantity was 0.25m, the water was distributed once every 6h; the

* To whom all correspondence should be sent:
E-mail: xuwenlai1983@163.com

operational mode was 2: the water was distributed once every day, for 2h every time, every time the water distribution quantity was 1m, the water was distributed once every 24h. The CRI simulation column was started with fresh water and the COD test yielded effluent every 3d.

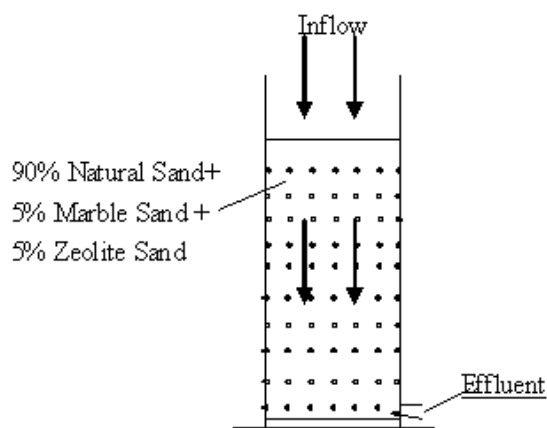


Fig.1. CRI simulation column.

Experimental Monitoring Items

The experimental monitoring items included CODCr, NH3-N, NO3-N, TN and TP. Table 1 shows the experimental monitoring method [5].

EXPERIMENTAL RESULTS AND ANALYSES

Experimental Results of COD Removal by the Cri System

Table 2 shows the COD concentration and removal rate of influent and effluent by the CRI simulation column under operational mode 1 (Notes: sampling times 1-13 are the natural bio-film colonization stage of the CRI system, and the sampling time 14 is the stable operational stage of the CRI system, Table 2 starts from sampling time 14) and Table 3 shows the COD concentration and

removal rate of influent and effluent of the CRI simulation column under operational mode 2. Table 4 shows the removal effect of COD by filtering materials of different heights in the CRI simulation column under operational mode 1.

To investigate the degradation rule of COD along with flow in the CRI simulation column, a wastewater sample at each sampling port along the flow in the CRI simulation column under operational mode 1 was taken, Table 4 displays the specific experimental results.

Rule Analyses of COD Removal by the Cri System

It can be seen from Table 2 that after the CRI system was operated steadily following successful natural bio-film colonization, the CRI system manifest a high COD removal rate under operational mode 1 (the hydraulic load cycle was 6h): after 7 tests (sampling numbers 14-32), after 12 tests the effluent COD concentration in the CRI system was less than 20mg/L, after 19 tests the effluent COD concentration in the CRI system was less than 30mg/L, after 19 tests the effluent COD concentration in the CRI system was less than 20.39 mg/L, in terms of the COD index, the effluent COD concentration in the CRI system under operational mode 1 reached the A-level standard or the first class standard of the Pollutant Discharge Standard for the Town and Country Sewage Treatment Project (GB18918-2002).

The influent COD concentration in the CRI system had a larger fluctuation range, whose minimum COD concentration was 90.36 mg/L and the maximum COD concentration was 189.61 mg/L, however, the effluent COD concentration in the CRI system had a small fluctuation range, which was maintained at 14-25 mg/L, suggesting that the CRI system had a stronger capacity for resisting the impact load for COD.

Table 1. Experimental methods of pollutant indexes.

| Index | Experimental method |
|-------------------|---|
| Water temperature | Thermometer method |
| Ph | Glass-electrodes method |
| COD | Potassium dichromate method |
| NH3-N | Nessler's reagent colorimetry |
| TN | Alkaline potassium per sulfate digestion-uv spectrophotometric method |
| TP | Ammonium molybdate spectrophotometric method |

Table 2. COD Concentration and Removal Rate of Influent and Effluent of the CRI Simulation Column under Operational Mode 1.

| Sampling times | Influent concentration (mg/L) | Effluent concentration (mg/L) | Removal rate (%) |
|----------------|-------------------------------|-------------------------------|------------------|
| 14. | 159.64 | 23.31 | 85.4 |
| 15 | 136.48 | 20.47 | 85 |
| 16 | 126.31 | 19.33 | 84.7 |
| 17 | 104.34 | 14.50 | 86.1 |
| 18 | 97.34 | 15.67 | 83.9 |
| 19 | 112.32 | 17.18 | 84.7 |
| 20 | 159.69 | 24.59 | 84.6 |
| 21 | 178.34 | 22.47 | 87.4 |
| 22 | 189.61 | 21.05 | 88.9 |
| 23 | 104.35 | 18.57 | 82.2 |
| 24 | 90.36 | 15.45 | 82.9 |
| 25 | 94.58 | 17.59 | 81.4 |
| 26 | 147.35 | 21.07 | 85.7 |
| 27 | 163.24 | 22.69 | 86.1 |
| 28 | 158.31 | 22.64 | 85.7 |
| 29 | 146.36 | 23.56 | 83.9 |
| 30 | 165.65 | 23.36 | 85.9 |
| 31 | 115.43 | 20.66 | 82.1 |
| 32 | 151.23 | 23.29 | 84.6 |

It can be seen from Table 3 that the removal effect of COD when the hydraulic load cycle was 24h declined dramatically compared with that when the hydraulic load cycle was 6h, with an average removal rate of only 59.1%, after 10 sampling tests (sampling numbers 33-42), after 7 sampling tests the final effluent COD concentration in the CRI system was greater than 60mg/L, after 3 tests the effluent COD concentration in the CRI system was greater than 50mg/L, after 10 tests the effluent average COD concentration in the CRI system was 60.77 mg/L, in terms of COD index, the effluent COD concentration in the CRI system exceeded the A-level standard of the first class standard of the

Pollutant Discharge Standard of the Town and Country Sewage Treatment Project (GB18918-2002).

Table 4 shows the change in COD concentration along the flow in the CRI system under operational mode 1 (the hydraulic load cycle is 6h). The average removal rate of COD by the CRI system in the 5 experiments was 84.9%, the removal rate of COD in the CRI filter tank 0-75cm segment reached 71.9%, accounting for 84.6% out of the total removal rate of COD by the CRI system, the removal rate of COD in the CRI filter tank 0-100cm segment reached 77.8%, accounting for 91.6% out of the total COD removal rate by the CRI system, suggesting that COD had been effectively removed

in the CRI filter tank 0-100cm segment and removed less effectively (only about 6%) in the CRI filter tank 0-100cm below the segment.

Mechanism Analyses of COD Removal by the Cri System

The following conclusions can be reached from the analysis of the COD removal mechanism by the laboratory simulation column[6-10]:

(1) Filtration and adsorption was the first step of organic pollutant removal by the CRI system.

It took a long time for the organic matter in the wastewater to be decomposed completely in the CRI system, more especially, some of the macromolecular organic matter can continue to be decompose aided by the microorganisms surrounding the filtering material in the CRI system only by being first decomposed into a dissolved state through hydrolytic processes, which needed to take a relatively long period of time, in the CRI system, the filtering material and bio-film first managed the interception and adsorption of organic matter to allow sufficient contact time with the microorganisms, during which they started the biochemical reaction to let the organic matter to be completely decomposed, absorbed and utilized by the microorganisms. The filtration and adsorption was the first step of organic pollutant removal by the CRI system, providing a basis for further degradation and removal of the organic matter.

(2) The organic matter accumulates during the flooding period and is oxidized and decomposed during the drying period in the CRI system.

When the wastewater flows through the filtering material of the CRI system, the organic matter becomes detached from the aqueous phase due to adsorption, interception and flocculation. By filtering the material and bio-film, among which a portion of low molecular weight and dissolved organic matter can be quickly decomposed, absorbed and utilized by the microorganisms in the CRI system and wastewater, but the macromolecular or granular organic matter can continue to be completely decomposed by the microorganisms in the CRI system only by first being decomposed by the hydrolytic process. This involves a process where the macromolecular and granular organic matter is decomposed and dissolved to organic matter that can be absorbed and utilized by the microorganisms following the action of the hydrolytic enzyme released by the microorganisms. This process needs a relatively long period of time, so the macromolecular organic matter absorbed by the filtering material of the CRI system cannot be decomposed by the

microorganisms in a timely fashion. The matter accumulates in the CRI system, if the CRI system is fed with water all the time, then more and more organic matter accumulates in the CRI system and this will easily result in a blockage of the CRI system. In order to operate normally, the CRI system adopted an alternate wetting and drying operational mode, during the flooding period, the organic mater accumulates in the CRI system, only a small portion of low molecular weight and dissolved organic matter can be decomposed by the microorganisms, in the drying period, because no new organic matter enters the CRI system, so the microorganisms in the CRI system have plenty of time to conduct biodegradation of organic matter accumulated during the flooding period, the assimilative capacity of the CRI system was restored in the drying period, allowing continued effective adsorption and accumulation of organic matter during the next wastewater feed. The alternate wetting and drying operational modes were the safeguard for a normal operation of the CRI system, while limiting the hydraulic load of the CRI system because it took a certain time for the macromolecular organic matter to be hydrolyzed, absorbed and utilized by the microorganisms, so the drying period should not be too short. Therefore, such alternate wetting and drying operational modes limit the increase of the hydraulic load of the CRI system.

(3) The aerobic degradation played an important role in the removal of organic matter by the CRI system.

The study showed that because the CRI system adopted the alternate wetting and drying operational mode and characteristics of the CRI system itself, the CRI filter tank upper segment (0-100cm) belongs to the aerobic/anaerobic alternating segment, which has a wide range of microorganisms, very complex, including obligate aerobes, facultative microorganisms and obligate anaerobes, a relatively rich content. The obligate anaerobes required a much stricter living environment than the bligate aerobes, since the CRI system had a longer drying period and shorter flooding period, which means that the aerobic/anaerobic alternating segment had a longer aerobic state and a shorter anaerobic state, thus this segment was advantageous to the growth and reproduction of aerobes and inhibits the growth of anaerobes. Therefore, the degradation of aerobes played an important role in organic matter removal by the CRI system in the aerobic/anaerobic alternating segment (CRI filter tank 0-100cm segment).

Table 3. COD Concentration and Removal Rate of Influent and Effluent of the CRI Simulation Column under Operational Mode 2.

| Sampling times | Influent concentration (mg/L) | Effluent concentration | Removal rate |
|----------------|-------------------------------|------------------------|--------------|
| | | (mg/L) | (%) |
| 33 | 163.4 | 47.39 | 71.4 |
| 34 | 158.6 | 65.03 | 59.6 |
| 35 | 148.3 | 63.32 | 57.3 |
| 36 | 167.5 | 68.34 | 59.2 |
| 37 | 159.1 | 61.73 | 61.2 |
| 38 | 146.8 | 64.45 | 56.1 |
| 39 | 152.4 | 59.89 | 60.7 |
| 40 | 154.7 | 65.75 | 57.5 |
| 41 | 146.2 | 58.77 | 59.8 |
| 42 | 136.7 | 53.04 | 61.2 |

Table 4. COD Concentration (mg/L) along the Flow in the CRI Simulation Column under Operation Mode 1.

| Sampling times | CRI filter tank depth (cm) | | | | | | |
|--------------------------|----------------------------|-------|------|------|------|------|-------|
| | 0 | 25 | 50 | 75 | 100 | 125 | 150 |
| 43 | 168.6 | 105.8 | 66.6 | 46.6 | 34.6 | 28.2 | 25.3 |
| 44 | 171.3 | 105.6 | 63.9 | 44.0 | 37.6 | 26.3 | 25.1 |
| 45 | 159.6 | 103.7 | 66 | 48.3 | 39.7 | 28.7 | 25.1 |
| 46 | 163.2 | 103.9 | 65.5 | 47.2 | 35.1 | 27.0 | 24.2 |
| 47 | 160.8 | 101.7 | 63.7 | 45.2 | 35.7 | 26.8 | 24.2. |
| Average removal rate (%) | 0 | 37.2 | 60.4 | 72.4 | 79.5 | 83.3 | 85 |

The CRI filter tank lower segment (100-150cm) was in an anaerobic state, but it made a small contribution to organic matter removal, there were two main reasons:

1. The decomposition capacity of anaerobes was far less than that of aerobes and the decomposition of organic matter was not complete.

2. The anaerobic reaction rate of the microorganisms related to the initial concentration of nutrients, the higher the initial concentration of organic pollutants, the faster the anaerobic decomposition reaction, which is otherwise slower.

3. Because the CRI filter tank 0-100cm segment had a high removal rate of the organic matter, with an average removal rate of around 80%, by producing a small quantity of organic matter entering the anaerobic zone of the CRI filter tank the lower segment had a low anaerobic biodegradation rate of organic matter.

In conclusion, the organic matter removal by the CRI system depended mainly on aerobic biodegradation.

4. The alternation of wetting and drying operational mode facilitated COD removal.

It can be seen from Table 2 and Table 3 that under the conditions of different wet-to-dry rates, the CRI system had a remarkably different removal efficiency for organic matter, which was mainly caused by a change in the hydraulic load cycle of the CRI system due to a different wet-to-dry rate. The organic matter removal by the CRI system depended mainly on aerobic biodegradation, so the reaeration state and hydraulic retention time of the CRI system will have a great influence on organic matter removal. The main reasons for the large difference in the removal rate of COD under the conditions of two different wet-to-dry rates in this experiment are mainly as follows:

1) Differences of the reaeration effect of the CRI system.

The CRI system is a technology for wastewater treatment using a natural system without the need for aeration and its reaeration process relies mainly on air convection and diffusion. At the time of infiltration of the residual water on the surface layer of the CRI system, the air inside and outside the CRI system initiates air convection due to infiltration and inhalation by the water and air convection carried through once within one hydraulic load cycle, the volume of air convected is equal to the volume of all the water coming out of the CRI system during the time from drying of the residual water on the surface layer of the CRI system to the next wastewater feeding of the CRI system. When the CRI system was in the drying period, its reaeration mainly relied on the air diffusion. The study conducted by Zhang Jinbing [7] suggests that even when the CRI system is in the drying period, the amount of reaeration through air diffusion is still low and it is difficult for oxygen to reach deeper into the CRI system. To allow for better reaeration of the CRI system, the hydraulic load cycle of the CRI system needed to be shortened, the wastewater feeding and drying frequencies needed to be increased, and air the convection times of the air inside and outside the CRI system needed to be increased, thus allowing for an increase of the reaeration efficiency of the CRI system, which will be favorable for the decomposition of organic matter by the aerobes inside the CRI system.

The operational mode for sampling numbers 14-32 required a one time wastewater dosing every 6h, 4 times per day and the CRI system completed the whole process of one time drying and flooding every 6h. Under such an operational mode, the CRI system had a higher drying frequency and less time and it conducted air convection 4 times every day, such an operational mode strengthened the

reaeration of the CRI system, while for sampling numbers 33-42, the infiltration column only conducted air convection once every day. Thus it can be seen that the hydraulic load cycle will directly affect the reaeration way and reaeration efficiency of the CRI system. Under these experimental conditions, the reaeration way of sampling numbers 14-32 relied mainly on the air convection, while the reaeration way of sampling numbers 33-42 relied mainly on the air diffusion. Therefore, the reaeration efficiency of sampling numbers 14-32 was much higher than that of sampling numbers 33-42, it was more favorable for the decomposition of organic pollutants by aerobes under the conditions of sampling numbers 14-32, so the CRI system had better removal efficiency for organic pollutants under the operational mode of 4 times of wastewater dosing per day and one time every 6h.

2) Hydraulic retention time.

The organic matter removal by the CRI system mainly relied on the degradation by aerobes, so the length of time of contact between the organic pollutants with the bio-film in the CRI system will have a great influence on the removal effect of the organic pollutants. Because the hydraulic load of the CRI system was relatively high in the CRI system, the hydraulic retention time (HRT) had a much greater influence on the removal effect of organic pollutants [8,9].

This experiment adopted two obviously different hydraulic load cycles and the HRT had a major difference under the conditions for two different hydraulic load cycles [10-13]. When the sampling numbers 14-32 adopted 4 times of wastewater dosing per day, once every 6h and the sampling numbers 33-42 adopted the hydraulic load cycle of 24h, under such different conditions the hydraulic load was the same, however, the wastewater quantity flowing through the CRI system of each time of wastewater distribution of sampling numbers 33-42 was equal to the total wastewater quantity flowing through the CRI system of 4 times of wastewater distribution for sampling numbers 14-32, so the actual flow rate of wastewater for sampling numbers 33-42 was significantly greater than that for sampling numbers 14-32. Therefore, the wastewater had longer HRT for sampling numbers 14-32, such an operational mode was more favorable for the degradation and removal of organic matter by microorganisms in the CRI system [14, 15].

CONCLUSIONS

The following conclusions were reached through the wastewater processing experiment by building a CRI simulation column:

(1) After the CRI system operated stably following the successful natural bio-film colonization, the CRI system had a high COD removal rate under operational mode 1: COD had been effectively removed in the CRI filter tank 0-100cm segment, with a removal rate reaching 77.8%, the effluent COD concentration in the CRI system under operational mode 1 reached the A-level standard for the first class standard of the Pollutant Discharge Standard of the Town and Country Sewage Treatment Project (GB18918-2002). The CRI system had a stronger capacity of resisting impact load for COD. The CRI system had a relatively ineffective removal effect of COD under operational mode 2, with an average removal rate of only 59.1%.

(2) Filtration and adsorption were the first steps in organic pollutant removal by the CRI system; organic matter in the CRI system was accumulated during the flooding period and oxidized and decomposed during the drying period; the aerobic degradation played an important role in organic matter removal by the CRI system; the alternate wetting and drying operational mode facilitated COD removal.

Acknowledgements: The research was funded by the Natural Science Foundation of China (No. 41502333), the State Key Laboratory of Geohazard Prevention and Geoenvironment Protection Foundation (No. SKLGP2015Z012, SKLGP2014Z001), the specialized research fund for the doctoral program of colleges and universities (No. 20135122120020), the scientific research plan of education department of Sichuan Province (No. 14ZB0073).

REFERENCES

1. W.L. Xu, Y.N. Yang, C. Cheng, *Journal of Coastal Research*, **73**, 386 (2015).
2. W.L. Xu, G. Liu, G.Y. Cui, *Journal of Pure and Applied Microbiology*, **7**(2), 1227 (2013).
3. Y. Xie, A. Kang, M. Li, *Chinese Journal of Environmental Engineering*, **4**(6), 1272 (2010).
4. W. Xu, J. Zhang, Y. Liu, *Fresenius environmental bulletin*, **20**(6A), 1487 (2011).
5. State Environmental Protection Administration, *Methods of Water and Wastewater Monitoring and Analysis* (Edition 4), Beijing, 2002.
6. J.B. Liu, PhD. Dissertation, China University of Geosciences, Beijing, 2006.
7. J. Zhang, PhD. Dissertation, China University of Geosciences, Beijing, 2010.
8. F. Zhao, PhD. Dissertation, China University of Geosciences, Beijing, 2010.
9. W. Xu, PhD. Dissertation, Southwest Jiaotong University, Chengdu, 2011.
10. R. Yao, PhD. Dissertation, Chongqing University, Chongqing, 2006.
11. J. Chen, PhD. Dissertation, Southwest Jiaotong University, Chengdu, 2008.
12. H. C. Qi, W. X. Peng, Y. Q. Wu, S. B. Wu, G. J. Xu, *Journal of Computational and Theoretical Nanoscience*, **9**(9), 1525 (2012).
13. Z. L. Liu, *Information Technology Journals*, **12**(17), 4158 (2013).
14. Z. L. Liu, *Journal of Applied Sciences*, **13**(21), 4702 (2012).

ОТСТРАНЯВАНЕ НА ОРГАНИЧНА МАТЕРИЯ И МЕХАНИЗЪМ НА ДЕЙСТВИЕ НА СИСТЕМАТА ЗА БЪРЗА ИНФИЛТРАЦИЯ

У.Л. Ксу, И.Н. Янг, Дж. Уанг, М. Танг, И. Джиан, С.Дж. Пей

Държавна ключова лаборатория за предотвратяване на геологични опасности и опазване на околната среда, Технологичен университет в Ченгду, 610059, Китай

Постъпила на 15 юни, 2015 г.; приета на 26 юли, 2015 г.

(Резюме)

Конструирана е бърза инфилтрационна система (CRI), която намира приложение в отстраняването на замърсители от водите. Механизмът на този процес още не е ясен, което пречатства на неговото разпространение и приложение. Експериментите по третиране на води в колона на базата на CRI-системата показват следното. При стационарен режим по способ 1 се постига висока степен на отстраняване на ХПК (до 77%) в слой от 0 до 100 cm. При способ 2 се постига средно само 59,1 % отстраняване на ХПК. При CRI-системата първите степени са филтруването и адсорбцията. Органичната материя се натрупва през периода на омокряне, а се окислява и се разлага в периода на сушене. Деграцията на аеробната материя изграе важна роля за отстраняване на органиката. Редуването на заливане и сушене благоприятства отстраняването на ХПК. Тези резултати обогатяват теоретичните знания за CRI-системата и насърчават приложението ѝ.

Performance, synthesis and removal of vanadium on ferruginous manganese composite material

Y. B. Huang¹, Q. Qiu^{1,*}, C. Y. Niu¹, H. Q. Gao¹, C. Huang¹, S. X. Tu²

¹School of Resources and Environmental Engineering, Wuhan University of Technology, Wuhan 430070, China;

²College of Resource and Environment, Huazhong Agricultural University, Wuhan 430070, China

Received May 10, 2015, Revised June 2, 2015

Through the processes of precipitation, filtration, drying and calcination, Fe-Mn compounds were synthesized artificially. The performance of these processes is accessed. By using X-ray fluorescence, testing the specific surface area, analyzing the X-ray diffraction, infrared spectroscopy, scanning electron microscopy testing technology to characterize this material, in order to investigate its mechanism of arsenate adsorption and the factors that influence. The results of the experiment showed that when the initial concentration of vanadium was 50mg/L, 0.1g of ferruginous manganese composite material was used, the reaction time reached 2 hours. The best absorption efficiency was obtained at the temperature 30°C and pH value of 4. Adsorption of ferruginous and manganese complexes of vanadium (V) are in accord with the Langmuir adsorption model ($R^2=0.9682$), the kinetic data are consistent with the two order kinetic models ($R^2=0.9999$), the maximum adsorption capacity is 14.16mg/g.

Key words: Fe-Mn compounds; Vanadium (V); influencing factors; adsorption mechanism; kinetics

INTRODUCTION

Vanadium is one of the main trace elements in fossil fuels, the vanadium compounds are usually toxic and their toxicity is enhanced by the increase vanadium content. Vanadium compounds have the highest toxicity. The vanadium smelt factory and vanadium alloy plant produce the chemical dust and aerosols which cause the high concentration of vanadium pollution in the neighboring area. The oil refineries, fuel and coal fired plants and chemical plants, also cause high toxicity and vanadium pollution of the water body. In the process of vanadium industry development the high concentration of vanadium industrial waste water has the characteristics of large and harmful emissions, heavy-toxicity, not easy to biodegrade. Therefore, finding an effective treatment to the vanadium containing wastewater and restoring the vanadium (V) polluted soil has become one of the most important research subject in the field of environmental science and technology.

Currently, the research on the treatment methods of industrial wastewater containing vanadium (V) at home and abroad mainly include chemical precipitates (including iron precipitation, lime neutralization precipitation and SO₂ precipitation), the ion exchange method and the adsorption method. The adsorption method is renewable and widely used. The previous reports in the literature on vanadium adsorbents, such as

natural mineral water talc [5], manganese acid leaching residues [6], modified iron-chips [7], modified ferrous ion zeolite [8], that have the good adsorption capacity of vanadium (V) ions. At the same time, the pilot study of the experiment [2] proved that natural iron manganese ore has the adsorption capacity of vanadium (V) up to 522 $\mu\text{g}\cdot\text{g}^{-1}$ and the contrast experiment resulted that the proportion of different iron ore and ferromanganese has a great influence on the removal of vanadium (V). Due to the above study, this experiment will compound the oxide iron that has a high surface charge, large specific surface area and strong adsorption ability for many inorganic contaminants [9] with manganese that has a strong oxidation ability. In the experiment, an effort to obtain more efficient vanadium (V) adsorption materials as well as the absorption performance and the functional mechanism of the oxide ferromanganese compound surface on the absorption of vanadium (V).

Introduction to the experiment

The main reagents and equipment

The equipment used in the experiments is comprised of ASAP 2020M an automatic specific surface area and porosity analyzer (American Micromeritics), an Axios advanced X-ray fluorescence spectrometer (Netherland PANalytical B.V), D/MAX-RB a target X-ray diffractometer (Japan RIGAKU), JSM-5610LV a scanning electron microscope (JEOL), UV-1100 an ultraviolet and visible spectrophotometer (Shanghai MAPADA) and others.

* To whom all correspondence should be sent:
E-mail: 364957055@qq.com

The main reagents used in this experiment were NaVO_3 , carbamide, BPHA, $\text{FeSO}_4 \cdot 7\text{H}_2\text{O}$, $\text{MnSO}_4 \cdot \text{H}_2\text{O}$, with a high purity, the water was deionized.

Introduction of the experimental methods

The preparation of ferruginous manganese composite material

To prepare the compound a series of different concentrations of Fe/Mn solutions, through the mixture of $\text{FeSO}_4 \cdot 7\text{H}_2\text{O}$ and $\text{MnSO}_4 \cdot \text{H}_2\text{O}$ in water and drop the precipitation saturated solution respectively in the series solutions. In the process of dropping, the stirring of solution need be done until it no longer produces new precipitation, the solution be put standing, and pour out the supernatant liquid. Following suction and filtering the lower metal oxide hydrate precipitate in the solution and after repeatedly washing the precipitate with deionized water, until the adding of BaCl_2 no longer produces a white precipitate in the filtrate. The metal oxide is dried under 105°C for 2 hours at a constant weight then put in a muffle furnace and calcinated for 2 hours under 450°C . After cooling, grinding and sieving with a 100 ~ 190 mesh, it is stored for further use.

Introduction of the characterization experiment

The Fe-Mn compounds are experimentally characterized by using XRF, BET, XRD, FTIR and SEM.

Introduction of the static adsorption experiment

Using a sodium metavanadate simulated compound 500 mg/L of vanadium (V) contained in wastewater reserve liquid (in this paper, the vanadium in the solution is measured as V_2O_5). Accurately weigh a 0.1g adsorbent and put it in a 100mL conical flask, 30.00mL certain a concentration simulated V_2O_5 solution, reacting after 1 hour in the thermostat oscillator under 30°C , then subjected to a high speed centrifugal spin for 30 min, BPHA and the extraction spectrophotometric method are used to analyze the residual V_2O_5 concentrations in the supernatant.

Introduction to the adsorption and adsorption kinetics experiment

By changing the pH value (2.0~12.0) and temperature ($25\sim 50^\circ\text{C}$) for different water quality conditions of the vanadium solution the adsorptive characteristics of vanadium (V) by the Fe-Mn compound is explored. Weighing another 0.1g of adsorbent and putting it in a 100mL conical flask, with 30.00mL of the concentration of 50mg/l V_2O_5 solution is placed in a thermostat oscillator under

30°C , the samples were taken at different time intervals, the vanadium (V) concentrations were measured and calculate the adsorption quantity for different periods.

THE RESULTS AND ANALYSIS

The best Fe/Mn mole ratio in the preparation of composite material

The selection of precipitant

In the preparation of a series of solutions where the Fe/Mn mole ratios are 5:1, 3:1, 1:1, 1:3, 1:5, NaOH and Na_2CO_3 are used as the precipitants, to prepare the compound oxides, the removal efficiency of vanadium (V) is compared, the results are shown in figure1. When the Na_2CO_3 is used as the precipitant, the removal rate of vanadium (V) is obviously higher than the NaOH precipitant, the reason is that Na_2CO_3 reacts with iron, manganese and generates the carbonate precipitation, in the subsequent calcination process, the carbonate decomposition releases large amounts of CO_2 , and the porosity of the Fe-Mn compound is increased. Due to the higher porosity, a better removal will result for vanadium (V), therefore, when Na_2CO_3 is used as the precipitant the Fe-Mn composite compound removal of vanadium (V) is better than when NaOH is the precipitant. In the subsequent experiments, Na_2CO_3 will be used as the precipitant to prepare the Fe-Mn compound and the precipitation sequence of different precipitants can be analyzed.

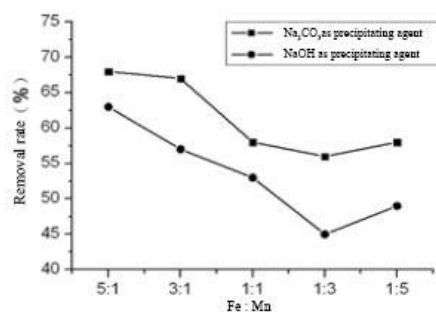


Fig.1. Comparison of the removal efficiency of the Fe-Mn compound when NaOH and Na_2CO_3 are used as precipitants.

Selection of the Fe/Mn mole ratio

Preparation of a series of solutions with Fe/Mn mole ratios (in this study refer to the mole ratio) are 12:1, 8:1, 5:1, 3:1, 1:1, 1:3, 1:5, 1:8, 1:12, the Na_2CO_3 is used as the precipitant to prepare the Fe-Mn compounds, by comparing the best Fe/Mn ratio for the removal efficiency of vanadium (V), the results are shown in figure 2.

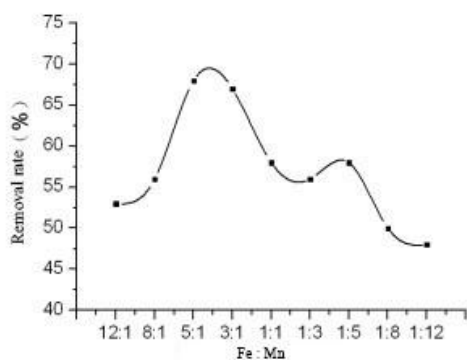


Fig. 2. Different Fe/Mn ratios (mole ratio) of Fe-Mn compounds with respect to the changes in the removal rate of vanadium (V).

As evident from figure 2 the removal efficiency increases quickly with the smaller ratio of Fe/Mn, when the Fe/Mn ratio was 5:1, the maximum removal rate reached 67.8%, and then showed a decrease trend. Therefore, the subsequent experiments will choose the 5:1 Fe/Mn ratio as the best ratio for the removal of vanadium (V).

The influence of water quality on Fe-Mn compound removal performance for vanadium

The influence of the pH value on the removal performance of vanadium

Under the same reaction conditions, the initial pH value of the vanadium solution is changed in turn to explore the adsorption effects, the results are shown in figure 3. It can be seen from the figure 3 that in the pH value range of 2.0 ~ 12.0, the removal rate of the Fe-Mn compound of vanadium (V) first increases with the increase of the pH then decreases. Under the acidic reacting conditions the adsorption efficiency of vanadium (V) is higher, when the pH value reaches around 4.0, the best adsorption efficiency is achieved, the reason is that the colloid of the Fe-Mn compound is positively charged; when the experiment deals with the adsorption of positive and negative charges the pH value is close to 2, vanadium exists as VO_2^+ , where the positive charge is not conducive to adsorption. When the pH value is between 3.8 ~ 3.8, the vanadium acid radical ion is $V_{10}O_{28}^{6-}$, $HV_{10}O_{28}^{5-}$ when the removal rate achieves a maximum [1]. The reason is that the acidic condition can enhance the protonation effect of the manganese ore surface, thus increasing the positive charge on the manganese ore surface [10] and plenty of H^+ will dissolve the ore into some metal, making it appear more porous increasing the specific surface area, thereby increasing the removal efficiency of vanadium (V) [11]. The adsorption efficiency obviously decreases with the increasing pH value, the reason is that the vanadium anion is

under an alkaline environment and for the OH^- there is a competition for adsorption sites on the surface of the manganese ore. Therefore, the best pH value for vanadium (V) adsorption of the Fe-Mn compound is 4.0.

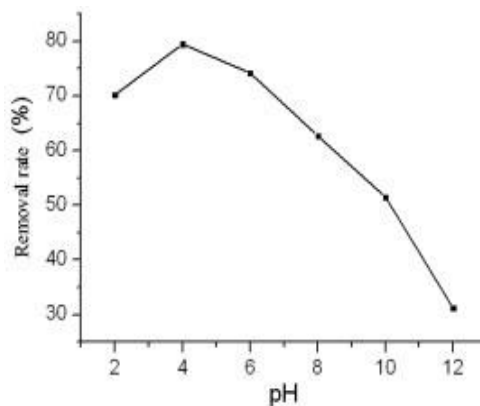


Fig. 3. The influence of the change in pH value on the removal performance of vanadium (V).

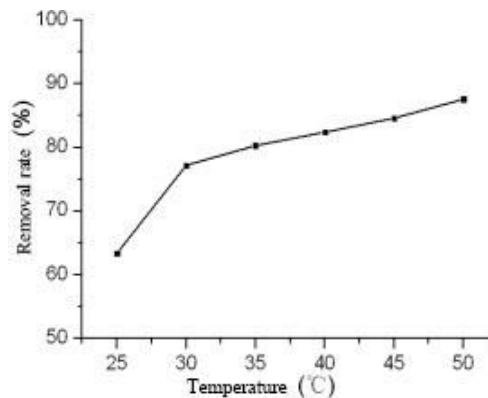


Fig. 4. The influence of the change reaction temperature on the removal performance of vanadium (V)

The influence of the reaction temperature on the removal performance of vanadium (V)

The characterization and functional mechanism of the Fe-Mn compound

The analysis of the Fe-Mn compound's composition

The composition of the adsorbent is the key factor that decides the adsorption performance of the material. In this study, the best Fe-Mn mole ratio of three mixture preparations are chosen as the adsorbents and the adsorbents are processed by grinding, drying and calcination, so the preparation of the adsorbent will not only contain iron, manganese ions, but could still contain a variety of other elements. In order to fully and accurately research the removal mechanism of compounds of the vanadium (V), XRF technology is used to obtain the composition elements of the Fe-Mn compound is shown in table 1. From table 1, it can be seen that there are 10 kinds of elements for Fe-

Mn compounds and according to the calculation the mole ratio is 5.04:1. In addition to iron and manganese oxide together with the Fe-Mn compound, due to cleaning that produce only residues of sodium oxide content that are more than 1%, the rest of the elemental contents are negligible. The removal efficiency in elimination of other elements' rather than vanadium (V) is high.

Table 1. The weight percentage of each oxide in the Fe-Mn compound.

| Name | Percentage (%) |
|--------------------------------|----------------|
| Na ₂ O | 2.76 |
| MgO | 0.06 |
| Al ₂ O ₃ | 0.02 |
| SiO ₂ | 0.05 |
| P ₂ O ₅ | 0.01 |
| SO ₃ | 0.74 |
| CaO | 0.10 |
| MnO | 7.53 |
| Fe ₂ O ₃ | 85.47 |
| Cl | 0.02 |
| Initial weight | 3.14 |

The analysis by SEM and BET

The methods of SEM and BET are used to analyze and measure the surface topography and specific surface area of the Fe-Mn compound. Presented in Figure 5 is a photo taken by a scanning electron microscopy that shows the morphology at an Fe/Mn ratio of 5:1. The Fe-Mn composite material before and after the removal of vanadium (V) are observed. It can be seen from figure 5 that the most of particles of the Fe-Mn compound are uneven in size although some are spherical, these particles adhere to each other and form a network structure, this natural phenomenon reflects the inherent adsorption properties of the Fe-Mn compound. The vanadium (V) ions are absorbed by water surface particles, with the help of a mesh structure bridge connection, the vanadium (V) ions form a large film that separates and removes the water. In the photo of after absorption that the space between spherical particles are significantly reduced, and large amounts of vanadium particles is absorbed by the surface of spherical particles. This photo further illustrates the reasons why the Fe-Mn compound has a good removal performance. Meanwhile, in the method of nitrogen adsorption - stripping characteristics are used to measure the specific surface area of the Fe-Mn compound that is 69.2m²/g. The result shows that the Fe-Mn

compound particles have a large specific surface area and high a surface free energy, which increases the chances that the particles react with the vanadium in the water and has a strong ability to remove the vanadium in the waste water.

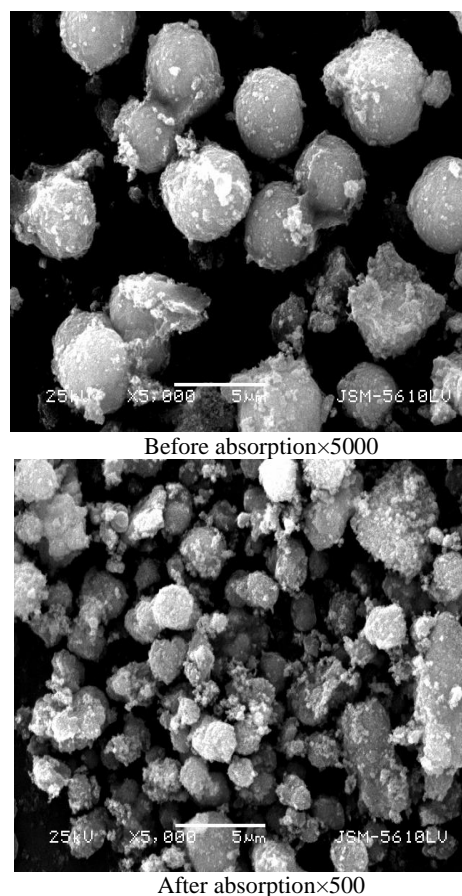


Fig. 5. The SEM pictures before and after the Fe-Mn compound adsorbs vanadium (V)

The analysis by XRD

The XRD technology is used to analyze the phase compositions of the Fe-Mn compound before and after adsorption of vanadium (V). It can be seen from figure 6 that before adsorption the composition of the Fe-Mn compound, appears similar to the magnetite and Mn₂O₃ characteristics of the diffraction peak, the main phase compositions are Fe₃O₄ (JCPDS 01-1111) and Mn₂O₃ (JCPDS 02-0902). There are some serious wide and diffuse peaks in the Fe-Mn compound XRD figure showing that the Fe-Mn compound is not crystalline but porous, most of the Fe-Mn compound is amorphous in form. Compared with the XRD figures presenting the material before and after adsorption, it can be argued that the graphics have large changes before and after adsorption. The material presented in figure 7 after the reaction appears similar to the V₂O₃, Fe₂O₃ and Mn₂O₃ characteristics of the diffraction peak in the Fe-Mn

compound, the main phase compositions are V₂O₃(JCPDS 01-1293), Fe₂O₃(JCPDS 03-0800), O₃(JCPDS 02-0902). These show that the chemical reaction occurs in the process of surface adsorption, partial vanadium acid radical ions are generate V₂O₃ and Fe₃O₄ is oxidized to Fe₂O₃.

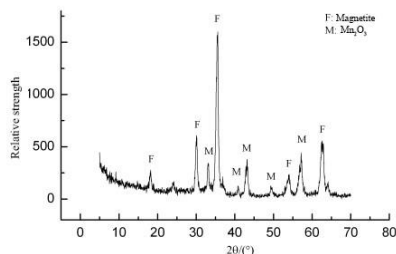


Fig. 6 The XRD figure before the Fe-Mn compound adsorbs vanadium (V).

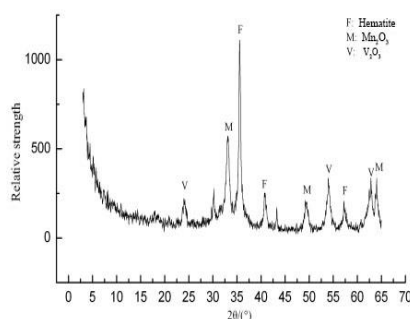


Fig. 7. The XRD figure after the Fe-Mn compound adsorbs vanadium (V).

The analysis by FTIR

In the study by an FTIR test to determine whether M-OH exist in the Fe-Mn compound, the FTIR figure of the process before and after adsorption is shown in figure 8.

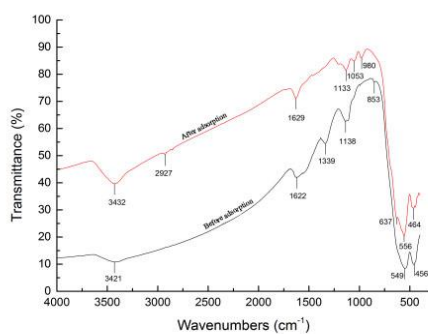


Fig. 8. The FTIR figure of the process before and after adsorption.

As shown in figure 8, the Fe-Mn compound there has the characteristic stretch vibration absorption peak of water and -OH (3421cm⁻¹~3432cm⁻¹) and -OH bending and vibration absorption peaks (1629cm⁻¹-1622cm⁻¹). The

absorption peak and the corresponding hydrated MnO₂ surface hydroxyl of the Mn-OH functional groups appear around 1138cm⁻¹. The characteristic peaks appear at around 1200cm⁻¹ both figures, which can explain the presence of Mn-OH. The absorption peak appearing at 1400cm⁻¹ is caused by the MnO₂ hydration component of the hydroxyl groups and water molecules. The stretching and vibration absorption peaks of the hydroxyl groups in Fe(OH)₃ and water molecules appear at 3421cm⁻¹ and 3432cm⁻¹; the bending and vibration peaks of the hydroxyl groups in Fe(OH)₃ and water molecules appear at 1622 cm⁻¹, 1629 cm⁻¹; the absorption peaks of α-FeOOH appear at 1162 cm⁻¹ and 460 cm⁻¹. Therefore, the iron compounds and hydroxyls play an important role in the process of the Fe-Mn compound removal of vanadium (V). It can result in adsorption of the Fe-Mn compound and removal of vanadium (V) and the complexation of the surface of material and hydroxyl of iron compounds. In figure 8, the vibration and absorption band at 980cm⁻¹ is caused by the V=O bond in the partial vanadium acid radical and the absorption band at 547cm⁻¹ corresponds to the vibration of the V-O-V bond in the aggregation of partial vanadium acid radicals[14].

The isotherm and kinetics of adsorption

The adsorption isotherm

Using the isothermal adsorption models of Langmuir and Freundlich and fitting the results show that the correlation of the former ($R^2=0.9682$) is bigger than the latter ($R^2=0.9056$), which shows that the removal of vanadium from the Fe-Mn compound is applicable in the Langmuir adsorption isothermal adsorption equation. The related model equation is shown below.

The Langmuir equation:

$$qe = 21.786 \frac{1 + 0.513p_e}{0.513p_e}$$

The model of the Langmuir isothermal curves fit well and illustrate the adsorption process of vanadium by the Fe-Mn compound, when the concentration is low the adsorption rate is fast and the adsorption quantity of growth is slow with the increase in concentration while the adsorption is gradually in balance, which also illustrates the removal of vanadium (V) which is directly adsorbed.

The adsorption kinetics

Figure 9 shows the vanadium (V) adsorption kinetics process for the Fe-Mn compound. It can be seen that the adsorption rate of vanadium (V) by the Fe-Mn compound is very fast, the adsorption

capacity reached in 2-hours' is 13.19 mg/g, after 4-hours' the adsorption is gradually balanced.

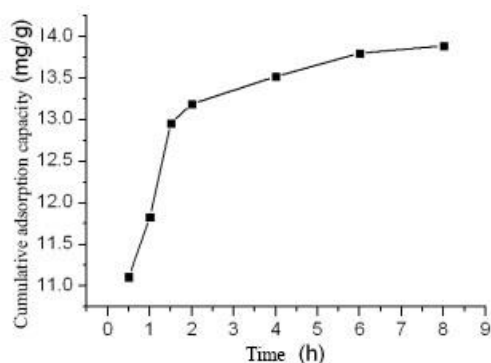


Fig.9. Curve of the adsorption rate of vanadium (V)

By using the kinetics adsorption model the specific fitting involved is shown in table 2, the adsorption model of the secondary kinetics ($R^2=0.9999$) has the greatest correlation and the Lagergren adsorption model of first order kinetics ($R^2=0.9765$) is greater than the fixed Elovich kinetics model ($R^2=0.9066$), so the adsorption kinetics of the Fe-Mn compound with vanadium is a better fit to the adsorption model of the secondary kinetics. Therefore, the adsorption process of vanadium (V) by the Fe-Mn compound is the chemical adsorption process. According to the calculation by this model, the maximum adsorption capacity of vanadium (V) by the Fe-Mn compound is 14.16 mg/g.

CONCLUSIONS

This paper presents a study on the removal performance of vanadium (V) through the co-precipitation preparation of the Fe-Mn compound; the conclusions obtained are as follows:

(1) The best conditions for preparation of the Fe-Mn compound are: the $\text{FeSO}_4 \cdot 7\text{H}_2\text{O}$ is chosen

as the ferrous salt, the $\text{MnSO}_4 \cdot \text{H}_2\text{O}$ is chosen as the manganese salt and Na_2CO_3 is used as the precipitate agent, when the calcination temperature is 450°C and a Fe/Mn ratio of 5:1 the best removal ability of vanadium (V) is achieved.

(2) In this paper, the chosen removal agent has a good performance and the metal elements are distributed evenly in the Fe/Mn compound (the mole ratio Fe-Mn is 5:1), its specific surface area is $69.2\text{m}^2/\text{g}$. Besides, the Fe-Mn compound particles attach to each other and form a mesh structure that arrange loosely, which has a good adsorption of the colloidal particles in the water that have a bridge connection and a trap function.

(3) Through the analysis of the controlling variables method the best water quality conditions are achieved: 0.1g of the Fe-Mn compound are used to process 50 mg/L of simulated wastewater that contain vanadium (V), oscillation under a constant temperature of 35°C for 120 min, when the pH value is 4.0 the highest removal efficiency of vanadium (V) is realized.

(4) The model of secondary kinetics and isothermal adsorption models of Langmuir can better fit the adsorption process of vanadium (V) respectively by using the Fe-Mn compound, in accordance with fitting the equation calculation of the Fe-Mn compound removal efficiency of vanadium (V), the maximum adsorption capacity is 14.16 mg/g.

The analysis of the mechanism of removal of vanadium (V) from the Fe-Mn compound contains the physical adsorption, electrical adsorption and co-precipitation, dependant on the pH value. The combination of multiple adsorption methods make the co-precipitation preparation of the Fe-Mn compound has a higher removal ability of vanadium (V).

Table 2. The fitting results of the stimulated kinetics data for the Fe-Mn compound adsorption of vanadium (V)

| | | | | | | | | |
|--------------------------------|---------------------------------------|---------|--------------------|---|--------|-------------------------------------|-------|--------|
| Lagergren first order kinetics | $q_e / \text{mg} \cdot \text{g}^{-1}$ | 13.89 | Secondary kinetics | $q_e / \text{mg} \cdot \text{g}^{-1}$ | 14.16 | Elovich Revised absorption kinetics | a | 12.09 |
| | k_1 / min^{-1} | -0.5321 | | $k_2 / \text{mg} \cdot \text{g}^{-1} \text{min}^{-1}$ | 0.448 | | b | 1.0007 |
| | R^2 | 0.9765 | | R^2 | 0.9999 | | R^2 | 0.9066 |

Acknowledgments: This research was supported by the national natural science foundation of China (Grant No. 41471407, 2015-2018), Major Projects on the Control and Management of the Water Body Pollution of China (2009ZX07104-001), China's rural environmental special fund, Program of Science and Technology in Wuhan, China (201060723315), and Innovation funds of postgraduate in Wuhan University of Technology, China (2010-24-ZH-010). The authors would like to thank Professor Y. Lin, X.Y. Long, L. Q. Qin et al for their assistance with the XRF and FTIR.

REFERENCES

1. B. Donald., *Cli. Tox.*, **37** (2), 273 (1999).
2. Y. B. Huang, C. Huang, Q. X. Yang. *Jou. of wuh. uni. (sci. edi.)*, **4**(1), 6 (2014)..
3. A. Bhatnagar, A. K. Minocha, D. Pudasainee. *Chem. Eng. Jou.*, **144**(2), 5 (2008).
4. F. Kaczala, M. Marques, W. Hogland. *Wat., Air & Soil Pol.*, **223**(5): 238 (2012).
5. A. Naeem, P. Wsterhoff. *Wat. Res.*, **41** (7), 1596 (2007).
6. H. R. Li, Y. L. Feng, J. L. Liang. *Rare met.*, **27** (2), 118 (2008).
7. C. Bioconjugate. *Env. Sci and Tec.*, **19** (3), 748 (2008)..
8. C. L. Peacock, D. M. Sherman. *Geo. et Cos. Acta*, **68** (8), 1727 (2004).
9. T. Kohn, K. J. T. Livi, A. L. Roberts. *Env. sci. & tec.*, **39**(8), 2875 (2005).
10. A. Astruc, C. Cochon, S. Dessources. *App. Cat. A-gen.*, **453**(2), 24 (2013).
11. Johanssonl. *Wat. Sci Te.* 35(5), 90 (1997).
12. K. Nakamoto. N. Y., Lon., J. W., **1**, 35 (2006).
13. M. Ding. *Geo. et Cos. Acta*, **64**(5), 1216 (2000).
14. Beg S., A. Al-Alas, N. A. S. Al-Areqi. *Mat. Chem.*, **124**(1), 309 (2010).

СВОЙСТВА, СИНТЕЗА И ОТСТРАНЯВАНЕ НА ВАНАДИЙ ОТ ФЕРО-МАНГАНОВИ КОМПОЗИТНИ МАТЕРИАЛИ

И.В. Хуанг¹, К. Кю^{1,*}, К.И. Ню¹, Х.К. Гао¹, К. Хуанг¹, С.С. Ту²

¹Училище по околна среда и ресурси, Технологичен университет в Ухан, 430070, Китай

²Училище по околна среда и ресурси, Селскостопански университет Хуажонг, Ухан 430070, Китай

Постъпила на 10 май, 2015 г.; приета на 2 юни, 2015 г.

(Резюме)

Изкуствено са синтезирани Fe-Mn-съединения чрез утаяване, филтруване, сушене и калциниране. Изследвани са свойствата им с помощта на рентгенова флуоресценция, инфрачервена спектроскопия, сканираща електронна микроскопия. Резултатите показват, когато началната концентрация на ванадия е 50 mg/L и са използвани 0.1 g от композитния материал реакционното време достига 2 часа. Най-добра абсорбция се постига при 30°C и рН 4. Адсорбцията на ванадий (V) върху композитите е в съгласие с изотермата на Лангмюир с висок коефициент на корелация ($R^2=0.9682$), а кинетичните данни се описват от кинетикана реакция от 2-ри порядък ($R^2=0.9999$). Максималният адсорбионен капацитет е 14.16mg/g.

Synthesis, structural and biological studies of cobalt ferrite nanoparticles

M.W. Mushtaq¹, M. Imran¹, S. Bashir², F. Kanwal¹, L. Mitu^{3*}

¹Institute of Chemistry, University of the Punjab, Lahore-54890, Pakistan

²Centre of Ionics, Department of Physics, Faculty of Science, University of Malaya-50603, Kuala Lumpur, Malaysia

³Department of Chemistry, University of Pitesti, Pitesti-110040, Romania

Received May 31, 2015; Accepted December 16, 2015

Cobalt ferrite's nanoparticles, CoFe_2O_4 (CF) were synthesized via the co-precipitation method using a new monomeric surfactant called sorbitol. Fourier Transform Infrared (FTIR) spectroscopy, X-ray powder Diffraction (XRD), a Vibrating Sample Magnetometer (VSM) and Scanning Electron Microscope (SEM) were used for their characterization. The presence of an (M–O) bond was confirmed by the absorption band at 589 cm^{-1} in the FTIR spectrum. VSM studies revealed the super paramagnetic nature of cobalt ferrite nanoparticles having a saturation magnetization value of 62.55 emu/g and 59.89 emu/g for cobalt ferrite NPs prepared without and with surfactant assistance respectively. The hysteresis loops showed negligible hysteresis, remanence and coercivity at 300 K. The powder X-ray Diffraction (XRD) pattern confirmed a single phase spinel cubic structure. SEM micrographs have been used to confirm the particle size which is found to be 28 nm with the surfactant and 60 nm without the surfactant and to analyse the distribution of NPs. Thermogravimetric measurements have also been studied to measure the presence of surfactant. The synthesized nanoparticles via the surfactant method were screened for their antibacterial activity against *Escherichia Coli* and *Staphylococcus Aureus* and demonstrated an appreciable activity. Furthermore, the interaction of cobalt ferrite nanoparticles with calf-thymus DNA was also investigated.

Keywords: Cobalt ferrite, Nanoparticles, Antibacterial activity, Calf-thymus DNA.

INTRODUCTION

In the past decade, nano-sized ferrite particles gained an attraction as a new emerging class of inorganic compounds because of their comprehensive applications in applied chemistry, high-density data storage, biochemistry, MRI and targeted drug delivery [1-3]. The paramount features about ferrite nanoparticles (NPs) established in the literature are that these compounds are non-toxic, biofriendly and exhibit strong antibacterial potential and magnetic capability [4,5]. Among these compounds, some notable examples of ferrites are iron Oxide (Fe_3O_4), nickel ferrite (NiFe_2O_4), manganese ferrite (MnFe_2O_4) and cobalt ferrite (CoFe_2O_4) nanoparticles that possess biocompatibility, small size, minimum toxicity and superparamagnetic properties enabling them as suitable candidates in the biomedical sciences. Ferrites are a family of metal oxides having a spinel structure MFe_2O_4 ($\text{M} = \text{Fe}^{+2}, \text{Co}^{+2}, \text{Ni}^{+2}, \text{Zn}^{+2}, \text{Mg}^{+2}, \text{etc.}$). The distribution of metal ions in ferrite NPs $[\text{M}^{+2}]_{\text{tetra}}[\text{Fe}^{+3}]_{\text{octa}}\text{O}_4$, modifies their magnetic behaviour.

One of the important type of nanoferrites is cobalt ferrite (CF) which exhibits an inverse spinel structure, a high curie temperature, superior chemical and mechanical stability and a large magnetic spin magnitude [6,7]. Cobalt ferrites (CoFe_2O_4) NPs have been synthesized by various physico-chemical methods such as hydrothermal reaction, micro-emulsion, sol-gel and co-precipitation techniques [8-10]. Relative co-precipitation is found to be the most used [11]. It is established in the literature that the nanostructure of cobalt ferrite possess Co^{+2} ions in octahedral sites (B) while Fe^{+3} ions are equally distributed between tetrahedral (A) and octahedral sites (B) [12].

To apply ferrite NPs in the engineering and biomedical fields, it is crucial to control the size, morphology and surface properties. During the genesis and growth of the primary nanoparticles, the surface chemistry of the primary nanoparticles is an important factor to control the final structure of the secondary nanoparticles by a process called Ostwald ripening, aggregation and coarsening [13]. The introduction of surfactants as a capping agent during synthesis of NPs, has been widely applied to control the size as well as the mechanical stability of ferrites as reported in the literature [14]. Various capping agents were applied to control the growth of building blocks of NPs including monomeric surfactants (ethylene glycol, glycerol, etc.) [15] and polymeric surfactants (PEG₃₀₀, PEG₆₀₀, PEG₁₀₀₀,

* To whom all correspondence should be sent:
E-mail: ktm7ro@yahoo.com

PEG₁₀₀₀₀, PVP₄₀₀₀₀, etc.)[16]. However, post treatment of NPs with monomeric surfactant is more beneficial because the polymeric surfactant may decrease the surface area by increasing the particle size. With monomeric surfactant, the particle size of the ferrites is easily controllable and a uniform distribution of metal ions is observed in octahedral and tetrahedral sites.

Keeping in view the literature and interesting features of cobalt ferrite nanoparticles, we have synthesized them by using a wet chemical route following the addition of a novel monomeric surfactant called sorbitol to explore their characteristic aspects as well as their biological properties.

EXPERIMENTAL

Materials: Iron chloride FeCl₃·6H₂O (98%), cobalt chloride CoCl₂·6H₂O (98%) were purchased from Uni-chem. Sodium hydroxide (99%) was procured from Riedel-de Haen while sorbitol and calf thymus DNA from BDH-England and Sigma Aldrich respectively. All these purchased chemicals were used without further purification.

The preparation of cobalt ferrite (CoFe₂O₄) nanoparticles: FeCl₃·6H₂O (0.03 mol, 8.109 g) and CoCl₂·6H₂O (0.015 mol, 3.567 g) were dissolved together in 100ml of double de-ionized water. Then sodium hydroxide solution (0.3 mol, 12g/100 ml) was added slowly until a pH of 11–12 was reached. The resulting reaction mixture was subsequently stirred at 80°C for 1h. Upon stirring a black coloured precipitate started to settle down. Finally, the formed precipitates were cooled, filtered, washed with de-ionized water and then by ethanol. The resulting solid was then dried at 100°C for 1h [17]. We also synthesized CoFe₂O₄ NPs by adding 2-3 drops of sorbitol (0.01 mol, 1.82 g) as a monomeric surfactant or capping agent while keeping all other parameters constant as mentioned above. The corresponding nanopowders obtained without and with a surfactant assisted approach are called product a and b respectively.

Characterization: Powder X-ray diffraction (PXRD) analysis was conducted on a Philips analytical X-ray diffractometer using CuK α radiation ($\lambda = 0.154$ nm). Fourier transform infrared (FTIR) absorption spectra were recorded using a Cary 630 FTIR spectrometer in the wave number range of 4000–400 cm⁻¹ with potassium bromide (KBr) pellets. UV–Vis spectra of pure cobalt ferrite NPs were obtained by using a UV–Vis spectrophotometer (UV-2600, Shimadzu). The magnetic behavior was studied by using a

Lakeshore-7404 vibrating sample magnetometer (VSM) at room temperature, 27°C up to a maximum applied magnetic field of 10 KOe.

Biological Studies

Antimicrobial studies; CoFe₂O₄ were screened for their antibacterial potential against Staphylococcus aureus and Escherichia coli strains by the Kirby-Bauer technique [18]. The antibacterial activity was determined by measuring the clear zone of inhibition after incubation for 24 h at 37°C.

Interaction between DNA and cobalt ferrite nanoparticles; the nanocomposite DNA/CoFe₂O₄ was prepared by mixing 0.1 mg/ml of calf-thymus DNA (0.308 mM for the Phosphate group) and 0.5 mg/ml of cobalt ferrite NPs in a Tris-Hcl buffer (10 mM, pH = 7.5). The resulting bionanocomposite was isolated from the solution using magnetic separation and washed with double distilled water. The concentration of DNA was recorded by a UV-Vis Spectrophotometer at 260 nm. The amount of adsorbed DNA was calculated by the following formula:

$$A = [(C_0 - C_i)v/m] \times 100\%$$

where C₀ is the initial concentration (mg/ml) of DNA in the solution, C_i is the concentration (mg/ml) of unbound DNA molecules, V is the volume of the reaction medium in ml and m is the mass of CF nanopowder. The adsorption capacity was expressed in mol/g and mol/m² taking into account that 1 mg/ml of DNA concentration corresponded to a 3.08 mmol/l concentration of the DNA phosphate group.

RESULTS AND DISCUSSION

The UV-Visible spectrum of CoFe₂O₄ NPs synthesized by the surfactant assisted method is shown in Fig.(1). It displays a characteristic band in the range 330–450 nm, which developed particularly from the dispersion and absorption phenomenon of CoFe₂O₄ magnetic nanoparticles and is in agreement with previous relations [18].

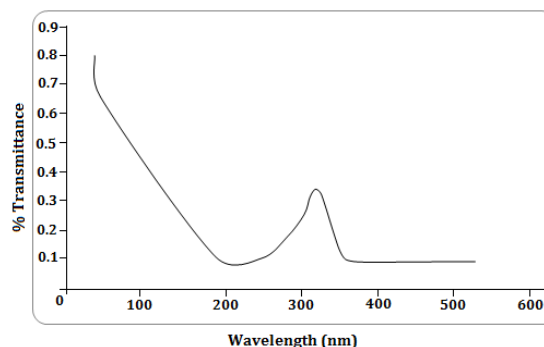


Fig. 1. UV-Visible spectrum of cobalt ferrite NPs.

Fig. 2 shows the effect of an applied magnetic field on the magnetization (emu/g) value of prepared cobalt ferrite NPs without and with the assistance of surfactant called product a and b respectively at room temperature. The M–H curves of both products (a, b) indicate types of hysteresis loop formation for soft magnetic materials with negligible coercivity, $H_c \sim 17.62$ and ~ 16.94 . It was also observed that by increasing the strength of the applied field, the value of saturation magnetization (M_s) for product a and b sharply increases and becomes nearly saturated at about 62.55 (emu/g) and 59.89 (emu/g) respectively, suggesting the presence of small magnetic particles exhibiting superparamagnetic behaviour of CF nanoparticles [18]. Fig.(2b) affirms that the magnetic feedback is not significantly altered by applying a sorbitol coating as a surfactant on the cobalt ferrite nanoparticles. However, the small decrease in the M_s value of the surfactant assisted prepared cobalt ferrite NPs is due to the small size of the magnetic core than the uncoated cobalt ferrite NPs. In addition to this, the non-magnetic coating layer of sorbitol can behave as a magnetic dead layer on the surface of cobalt ferrite NPs, thus reducing their saturation magnetization potential [19].

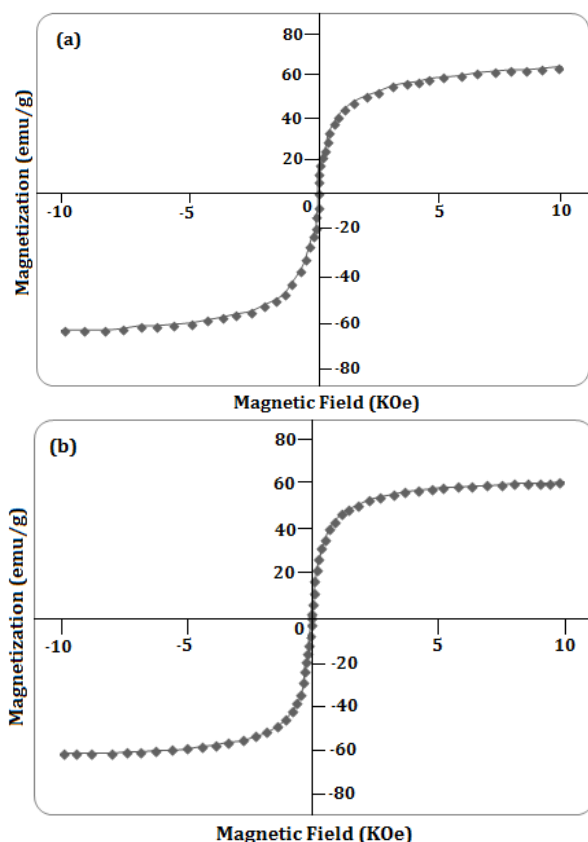


Fig. 2. (a) Effect of an applied field on the magnetization value of cobalt ferrite NPs prepared without surfactant (b) with surfactant.

FT-IR spectra of pure cobalt ferrite NPs synthesized without and with the sorbitol assisted method at room temperature are shown in Fig.(3). Two characteristic bands at ~ 598 , ~ 592 and ~ 492 , ~ 484 cm^{-1} were observed in both products a and b which may correspond to intrinsic stretching vibrations of the metal at a tetrahedral site ($M_{\text{tetra}}-\text{O}$) bond and at an octahedral site ($M_{\text{octa}}-\text{O}$) respectively [20,21]. The other important peaks of products a and b at ~ 3440 , ~ 3478 and ~ 1640 , ~ 1636 cm^{-1} can be attributed to H–O–H stretching and bending vibrations of the absorbed water molecules on the surface of cobalt ferrite NPs respectively [22]. The additional peaks observed in Fig.(3b) at 2930 and 2864 cm^{-1} correspond to $\nu_{\text{as}}(\text{C-H})$ and $\nu_{\text{s}}(\text{C-H})$ respectively and confirm the coated layer of sorbitol surfactant.

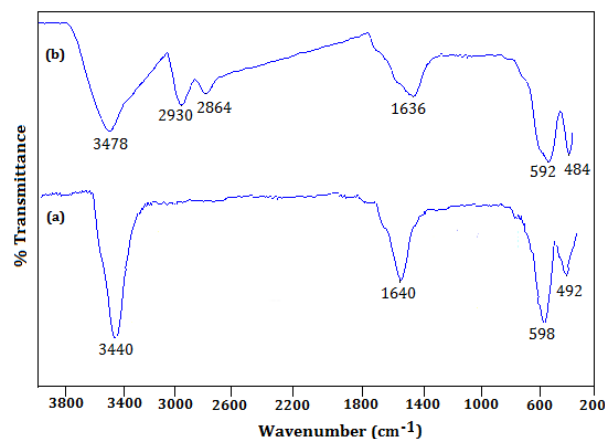


Fig. 3. (a) FT-IR spectra of CoFe_2O_4 nanoparticles synthesized without surfactant (b) with surfactant assistance.

DSC/TGA was carried out in the temperature range 25°C to 650°C and the curves of the product b prepared with surfactant are shown in Fig.(4). The TGA curve in Fig.(4) exhibits two steps attributed to individual weight loss. The first loss was observed in the range 25°C to 150°C while the second loss appeared in the range 300°C to 450°C . The DSC curve shows a broad endothermic peak at 150°C . This might be due to desorption of water molecules from the surface of the surfactant and cobalt ferrite. The exothermic peak in the DSC curve was observed at 350°C . The exothermic peak can be referred to the combustion of coated surfactant. Above 450°C , no weight loss was found indicating the presence of only cobalt ferrite nanoparticles in the temperature range 450°C to 650°C [23,24].

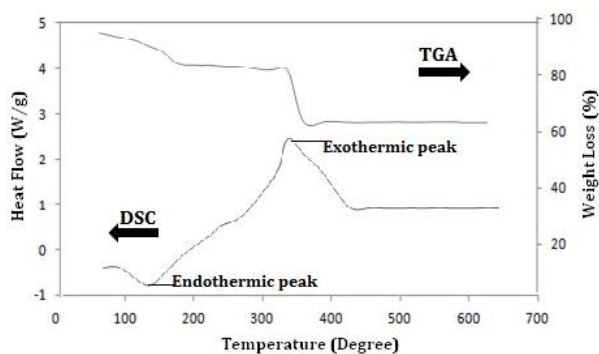


Fig. 4. DSC/TGA curves of cobalt ferrite nanopowder.

The X-ray diffraction pattern of CoFe_2O_4 nanoparticles prepared in the form of product a and b is presented in Fig.(5). All the characteristic peaks in both products at angles 18.29° , 30.08° , 35.44° , 37.06° , 43.06° , 53.45° , 56.98° and 62.59° are indexed as the reflection planes of (111), (220), (311), (222), (400), (422), (511) and (440) respectively. These peaks exactly match the JCPDS (22-1086) data and confirm the single phase inverse spinel structure of the CoFe_2O_4 nanocrystals [25,26]. However, product a shows an improvement of the crystalline phase of cobalt ferrite NPs as compared to product b which was prepared in the presence of the surfactant. The particle size has been determined by the Debye Sherrer equation ($D = 0.9\lambda/\beta\cos\theta$, where D is the crystalline size, λ is the wavelength of the X rays, β is the full width at half maximum of the diffraction peak and θ is Bragg's angle) which is 65 nm and 32 nm for product a and b respectively. In product b the presence of a broad diffraction plane (311) justifies the smaller CoFe_2O_4 NPs formed in the presence of a capping agent. This fact may be due to the performance of a monomeric surfactant in the reduction of clustering of the nanoparticles[15].

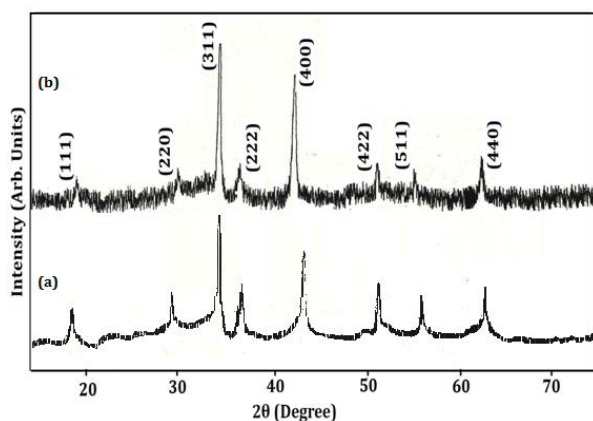


Fig. 5. X-ray diffraction pattern of CoFe_2O_4 nanoparticles prepared (a) without a surfactant (b) with an additional surfactant.

SEM analysis of the cobalt ferrite NPs prepared without and with a surfactant are shown in Fig.(6). The average size of the cobalt ferrite NPs was about 60 nm and 28 nm for products a and b respectively which nearly matches the crystallite sizes calculated by XRD. The morphology of the cobalt ferrite NPs in product a is comprised of spherical nanocrystallites and has a uniform distribution of nanoparticles which defines the effectiveness of the surfactant. However, a slight compactness and clustering of NPs were observed in the case of product b.

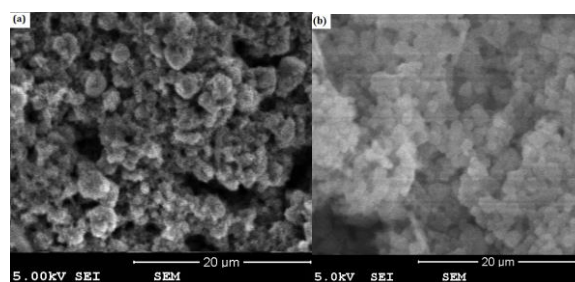


Fig. 6. (a) SEM images of Cobalt ferrite NPs prepared without a surfactant (b) with a surfactant.

The antibacterial potential of CoFe_2O_4 NPs prepared by the surfactant method (product b) was screened against two common bacterial pathogens, *Escherichia coli* and *Staphylococcus aureus*. Generally, it was found that Gram negative strain *E.coli* is more sensitive to CoFe_2O_4 as compared to Gram positive strain *S.aureus*[27] Fig.(7) and (8) demonstrate that with increasing the CoFe_2O_4 concentration, the zone of inhibition also increases. The zone of inhibition was also determined for tetracycline and streptomycin as reference antibiotics. The antibacterial activity of cobalt ferrite NPs is due to their particularly small size which makes a perfect attachment to the membrane of the micro-organism [28-30].

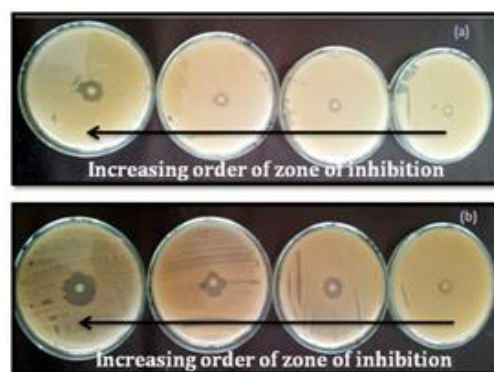


Fig. 7. Zone of inhibition measured for (a) *Staphylococcus aureus* (b) *Escherichia coli* in the presence of different concentrations of CoFe_2O_4 .

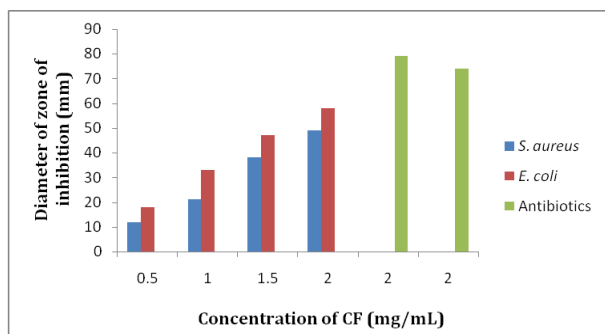


Fig. 8. Comparison of the zone of inhibition as measured in different concentrations of CoFe_2O_4 NPs and antibiotics.

The interaction behaviour of cobalt ferrite NPs (product b) with calf-thymus DNA was also investigated. The IR spectral features of pure CoFe_2O_4 NPs (product b), pure calf-thymus DNA and CoFe_2O_4 /calf-thymus DNA nanocomposites are shown in Fig.(9). In Fig.(9a), the spectrum shows an absorption at 585cm^{-1} for the M–O bond of CoFe_2O_4 [31]. Fig.(9b) presents the characteristics peaks of calf-thymus DNA with the interesting region $1800\text{--}700\text{ cm}^{-1}$ describing the deoxyribose stretching of DNA, oscillation of the groups in the heterocyclic nitrogenous bases and stretching vibrations (asymmetric and symmetric) of the phosphate group (PO_2^{-1}). Two feature bands at 1225 and 1085 cm^{-1} depict the asymmetric and symmetric vibrations of PO_2^{-1} respectively [32]. The absorption band at 1054 cm^{-1} appears as a sugar band in the IR spectrum. In Fig.(9c), the spectrum exhibits the presence of a (M–O) bond at 587 cm^{-1} confirming the formation of the CF/calf-thymus DNA nanocomposite. The changes in the intensity ratios of the symmetric and asymmetric vibrations (v_s/v_{as}) of the phosphate group PO_2^{-1} indicate the participation of the PO_2^{-1} group in the synthesis of the bio-nanocomposite [33,34]. The shifting of the guanine (G) band from 1717 to 1708 cm^{-1} and the increase in intensity of the thymine (T) band at 1667 cm^{-1} indicate that the heterocyclic bases are interacting with cobalt ferrite NPs. The shift of the asymmetric and symmetric peaks of the phosphate group (PO_2^{-1}) from 1225 to 1219cm^{-1} and 1085 to 1088cm^{-1} also indicate the interaction of the phosphate group (PO_2^{-1}) with the surface of the ferrites nanoparticles [35]. The interaction of the CF/DNA bio-nanocomposite occurs due to the formation of coordination bonds between cobalt and iron ions on the particle surface and the oxygen atoms in the DNA (phosphate group, O6 in guanine and O4 in thymine) as already explained in the literature [36].

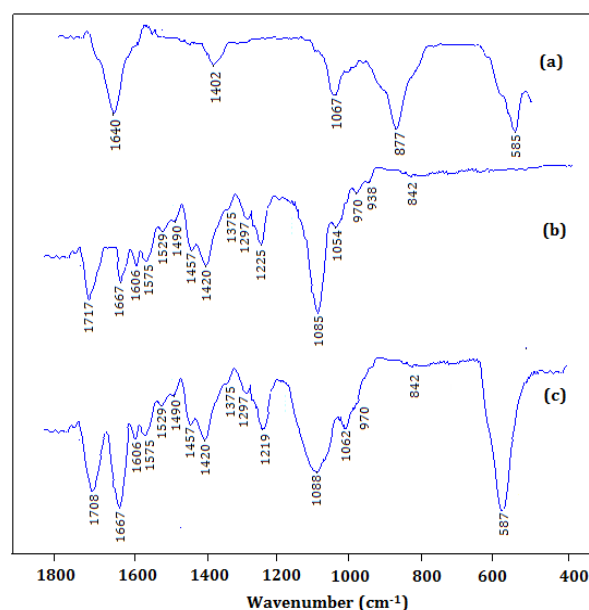


Fig. 9. (a) FT-IR spectra of pure CoFe_2O_4 nanopowder (b) Calf-thymus DNA (c) CF/DNA.

CONCLUSIONS

The present study demonstrates the synthesis of cobalt ferrite nanoparticles using a novel surfactant assisted co-precipitation method. The XRD pattern exhibits the presence of a cubic spinel phase in cobalt ferrite NPs. The size of the cobalt ferrite NPs was effectively reduced by applying a surfactant as measured by the XRD pattern which is in agreement with the SEM images. The outstanding magnetic response of cobalt ferrite NPs in the presence of an applied magnetic field may direct them as an efficient nanocarrier for targeted drug delivery. TGA/DSC studies are affirming the presence of a capping agent on the surface of cobalt ferrite NPs. The prepared cobalt ferrite nanoparticles also have an antibacterial potential against *E.coli* and *S.aureus* and are capable to develop interactions with nitrogenous bases of DNA. Finally, we can say that the cobalt ferrite NPs prepared by the surfactant assistant method have the potential to be applied as a biomaterial in numerous fields of material engineering, biomedical and biotechnology systems.

REFERENCES

1. O. Yamamoto, *Int. J. Inorg. Mater.*, **3**, 643 (2001).
2. L. Zhang, Y. Jiang, Y. Ding, M. Povey, D. York, *J. Nanopart. Res.*, **9**, 479 (2007).
3. O. Seven, B. Dindar, S. Aydemir, D. Metin, M.A. Ozinel and S. Icli, *J. Photochem. Photobiol. A: Chemistry*, **165**, 103 (2004).
4. R. Brayner, R. Ferrari-Iliou, N. Brivois, S. Djediat, M.F. Benedetti, F. Fiévet, *Nano Lett.*, **6**, 866 (2006).
5. J. Sawai, *J. Microbiol. Methods*, **54**, 177 (2003).

6. X. Meng, H. Li, J. Chen, L. Mei, K. Wang, X. Li, *J. Magn. Magn. Mater.*, **321**, 1155 (2009).
7. L. Phua, F. Xu, Y. Ma, C. Ong, *Thin Solid Films*, **517**, 5858 (2009).
8. S. Sun, H. Zeng and D.B. Robinson, *J. Am. Chem. Soc.*, **126**, 273 (2004).
9. D.N. Williams, S.H. Ehrman, T.R.P. Holoman, *J. Nanobiotechnol.*, **4**, 3, doi:10.1186/1477-3155-4-3 (2006).
10. P. Gong, H. Li, X. He, *Nanotechnology*, **18**, 285604, doi:10.1088/0957-4484/18/28/285604 (2007).
11. M. Banooee, S. Seif, Z.E. Nazari, *J. Biomed. Mater. Res. B: Appl. Biomater.*, **93**, 557 (2010).
12. P. Gajjar, B. Pettee, D.W. Britt, W. Huang, W.P. Johnson, A.J. Anderson, *J. Biol. Engg.*, **3**, 1 (2009).
13. R.L. Penn, K. Tanaka, J. Erbs, *J. Cryst. Growth*, **309**, 97 (2007).
14. M. Niederberger, H. Colfen, *Phys. Chem. Chem. Phys.*, **8**, 3271 (2006).
15. K. Nejati and R. Zabihi, *Chem. Cent. J.*, **6**, 1 (2012).
16. T.R. Bastami, M.H. Entezari, Q.H. Hu, S.B. Hartono, S.Z. Qiao, *Chem. Eng. J.*, **210**, 157 (2012).
17. Y. Zhang, G.K. Das, R. Xu, T.T.Y. Tan, *J. Mater. Chem.*, **19**, 3696 (2009).
18. R. Mehta, P. Goyal, B. Dasannacharya, R. Upadhyay, V. Aswal, G. Sutariya, *J. Magn. Magn. Mater.*, **149**, 47 (1995).
19. O. Ur Rahman, S.C. Mohapatra, S. Ahmad, *Mater. Chem. Phys.*, **132**, 196 (2012).
20. S. Kumar, V. Singh, S. Aggarwal, U.K. Mandal and R.K. Kotnala, *J. Phys. Chem. C*, **114**, 6272 (2010).
21. S. Ahmad, U. Riaz, A. Kaushik, *J. Alam, J. Inorg. Organomet. Polym. Mater.*, **19**, 355 (2009).
22. R. Raveendra, P. Prashanth, B. Daruka Prasad, *Int. J. Sci. Res.*, **1**, 543 (2012).
23. G. Allaedini, S.M. Tasirin, P. Aminayi, *Int. Nano Lett.*, doi:10.1007/S40089-015-0153-8 (2015).
24. A.C.F. Costa, M.R. Morelli, R.H. Kiminami, *J. Mater. Sci.*, **42**, 779 (2007).
25. K. Maaz, S. Karim, A. Mumtaz, S. Hasanain, J. Liu, J. Duan, *J. Magn. Magn. Mater.*, **321**, 1838 (2009).
26. N. Sanpo, J. Wang and C.C. Berndt, *J. Nano Res.*, **25**, 110 (2013).
27. S.S. Mukhopadhyay, *Nanotechnol. Sci. Appl.*, **7**, 63 (2014).
28. L.L. Radke, B.L. Hahn, D.K. Wagner, P.G. Sohnle, *Clin. Immun. Immunopathol.*, **73**, 344 (1994).
29. R.M. Wang, B.Y. Wang, Y.F. He, W.H. Lv, J.F. Wang, *Polym. Advan. Technol.*, **21**, 331 (2010).
30. A. Baykal, N. Kasapoglu, Y. Koseoglu, A. C. Basaran, H. Kavas, M.S. Toprak, *Cent. Eur. J. Chem.*, **6**, 125 (2008).
31. D.K. Jangir, G. Tyagi, R. Mehrotra, S. Kundu, *J. Mol. Struct.*, **969**, 126 (2010).
32. H. Tajmir-Riahi, R. Ahmad, M. Naoui, S. Diamantoglou, *Biopolymers*, **35**, 493 (1995).
33. A.U. Metzger, T. Schindler, D. Willbold, *FEBS Lett.*, **384**, 255 (1996).
34. H. Malonga, J. Neault, H. Arakawa, H. Tajmir-Riahi, *DNA Cell Biol.*, **25**, 63 (2006).
35. J. Anastassopoulou, *J. Mol. Struct.*, 651,19 (2003).
36. K. Maaz, A. Mumtaz, S. Hasanain, A. Ceylan, *J. Magn. Magn. Mater.*, **308**, 289 (2007).

СИНТЕЗА, СТРУКТУРНИ И БИОЛОГИЧНИ ИЗСЛЕДВАНИЯ НА НАНОЧАСТИЦИ ОТ КОБАЛТОВИ ФЕРИТИ

М.У. Муштак¹, М. Имран¹, С. Башир², Ф. Канвал¹, Л. Миту^{3*}

¹Институт по химия, Университет в Пунджаб, Лахор-54890, Пакистан

²Департамент по физика, Научен факултет, Университет в Малая-50603, Куала Лумпур, Малайзия

³Департамент по химия, Университет в Питещ, Питещ-110040, Румъния

Постъпила на 31 май 2015 г.; приета на 16 декември 2015 г.

(Резюме)

Синтезирани са наночастици от кобалтови ферити, CoFe_2O_4 (CF) по метода на съутаяване с използването на нов мономерен сърфактант (сорбитол). За охарактеризирането им са използвани Фуриерова инфрачервена спектроскопия (FTIR), прахов рентгеноструктурен анализ (XRD), магнетометър с вибрираща проба. Потвърдено е наличието на (M–O) - връзка по абсорбционната линия при 589 cm^{-1} в FTIR-спектъра. VSM-изследвания разкриват свръх-парамагнитни свойства на наночастиците от кобалтови ферити, имащи наситена магнетизация съответно 62.55 emu/g и 59.89 emu/g за кобалтовите ферити, приготвени без и със сърфактант. Хистерезисните контури показват пренебрежим хистерезис, остатъчен магнетизъм и коерцитивност при 300 K. Рентгеноструктурният анализ (XRD) потвърждава като единствена фаза шпинелна кубична структура. Електронно-микроскопски (SEM) микрографии са използвани за определянето на размерите на частиците като 28 nm с използването на сърфактант и 60 nm без сърфактант. Микрографиите са използвани и за анализ на разпределението по размери. Съдържанието на сърфактант е изследвано чрез термогравиметрични измервания. Направен е скрийнинг на приготвените частици за антибактериална активност срещу *Escherichia coli* and *Staphylococcus aureus*, който показва значителна активност. Освен това е изследвано взаимодействието на наночастиците с ДНК от телешки тимус.

The most stable transition state complexes of the aminotoluene molecule

B. Eren¹, Y. Y. Gurkan^{2*}

¹Namik Kemal University, Faculty of Agriculture, Tekirdag / Turkey

²Namik Kemal University, Department of Chemistry, Tekirdag / Turkey

Received January 15, 2015, Revised February 8, 2015

In this study the most probable reaction paths of ATnm, OATnm, MATnm, PATnm, NMATo and NMATm transition states with OH radicals have been analyzed. The optimized geometry was calculated via Gauss View 5. Subsequently, the lowest energy level was found by geometric optimization via the Gaussian 09 programme. The geometrical structure analysis and bond lengths were also calculated. This study aims to determine the most probable path for the product distribution of transition state complexes and OH radical interaction in the gas phase and aqueous media. Quantum mechanical methods were used to indicate the impact of the reaction rate over the primary intermediate, hydroxylated intermediate and finally the impact of water solvent. With the aim to determine the intermediates occurring at the reaction of transition state complexes degradation, the geometric optimization of the reactant and transition state complexes were realized through semiempirical AM1 and PM3, ab initio Hartree-Fock HF/3-21G, HF/6-31G* and Density Functional Theory (DFT) methods. Determining the most appropriate method and the reliability of the method are compared and evaluated theoretically. Based on the Quantum mechanical calculation, all the probable rate constants of reaction paths were calculated by using Transition State Theory (TST). In order to determine the transition state of the reaction, C-O bonds were taken as a reference. Activation energy for probable reaction paths of all transition state complexes, and their most stable state were calculated from the thermodynamic perspective for the gas phase and aqueous media. The impact of water solvent was investigated by using COSMO as the solvation model.

Keywords: Aminotoluene, AM1, PM3, HF, TST.

INTRODUCTION

Volatile aromatic compounds constitute a major part of air and water contaminants. They are mainly emitted into the environment from anthropogenic sources such as combustion processes, vehicle emissions and industrial sources, as well as from biogenic processes [1,2]. Organic contaminants exist at very low concentrations in the water [3]. Therefore, it is essential that the organic contaminants be removed from the drinking water [4]. Natural purification of water systems such as rivers, creeks, lakes, and pools is realized by the solar light falling on the earth. Sunbeams initiate the degradation reaction of big organic molecules into smaller and basic molecules, finally providing for the formation of CO₂, H₂O and other molecules [5,6].

In its reactions with organic molecules, OH behaves as an electrophile whereas O is a nucleophile. Thus, OH readily adds to unsaturated bonds while O does not. Both forms of the radical abstract H from C-H bonds and this can result in the formation of different products when the pH is raised to a range where O rather than OH is the reactant. For example, if an aromatic molecule

carries an aliphatic side chain, O attacks there by radical abstract H whilst OH adds preferentially to the aromatic ring [7]. The hydroxyl radical which is the most reactive type known in biological systems reacts with every biomolecule it encounters, including water. Potentially, every biomolecule is a hydroxyl radical scavenger at different speeds [8]. Aromatic compounds are good detectors since they hydroxylate. In addition, the position of attack to the ring depends on the electron withdrawal and the repulsion of previously present substituents. The attack of any hydroxyl radical to an aromatic compound results in the formation of a hydroxylated product [9]. Ortho-toluidine used as an intermediate in large volumes of herbicides can be solved little in water, yet can be solved in alcohol, ether, and diluted acids. Toluidine is a synthetic chemical that is normally a light yellow liquid, but turns to a reddish brown when exposed to air and light [10]. The chemical properties of toluidine are very similar to aniline and it has common features with other aromatic amines. It is a weak basic due to the amino group that is attached to the aromatic ring. At room temperature and pressure, ortho-and-meta-toluidines are viscous liquids; however the molecules in para-toluidine are more symmetrical and fit the crystal structures [11, 12].

* To whom all correspondence should be sent:

E-mail: yyalcin@nku.edu.tr

While an intermediate in aminotoluene herbicide synthesis is used in the production of more than 90 paints and pigments, rubber, chemicals and pesticides, it is also used as a hardening agent for epoxy resin systems, a reactive material for glucose analysis and fibre dyeing in clinical laboratories [13]. Due to the damaging effects of living organisms emitting resistant foul smell and because of their solubility, aminotoluenes and their derivatives constitute an important water contaminant group. Although many methods are available for the removal of these molecules from water, every method has its own inconvenience [13-18].

In the study of Eren et al.[18] the most probable reaction paths of the aminotoluene (o-toluidine) molecule with OH radicals have been analyzed. The optimized geometry was calculated via Gauss View 5. Subsequently, the lowest energy level was found through geometric optimization via the Gaussian 09 programme. The geometrical structure analysis and bond lengths were also calculated. According to the DFT method the constant k and the entropy were found to be the highest, the enthalpy and Gibbs free energy values were the lowest, the transition states of ATnm, OATnm, MATnm, PATnm, NMATo and NMATm were concluded to be the most stable and had the lowest energy transition complexes [18].

In this study, the kinetics of the degradation reaction of the transition states of ATnm, OATnm, MATnm, PATnm, NMATo and NMATm and the hydroxyl derivatives were analyzed theoretically. With the aim to determine the intermediates obtained from the reaction of aminotoluene degradation, geometric optimization of the reactant and the transition state complexes were realized through AM1 and PM3, HF/3-21G, HF/6-31G* and DFT methods. Based on the quantum mechanical calculation, all the probable rate constants of the reaction paths were calculated by using TST.

COMPUTATIONAL SET-UP AND METHODOLOGY

Computational models

The molecular models were created by using the mean bond distances, the geometric parameters of the benzene ring, the tetrahedral angles for sp³-hybridized carbon and oxygen atoms and 1200 for the sp²-hybridized carbon atoms. In the calculation of the hydroxylated radicals, the aromatic ring was left planar except for the position of attack. The attacking •OH radical was assumed to form a tetrahedral angle with the C–H bond due to the

change in the hybridization state of the carbon at the addition centre from sp² to sp³ [2,18].

Molecular Orbital Calculations

It is possible that in the photocatalytic degradation reactions of organic contaminants, more harmful products may occur than in the original material. Therefore, before experimentally realizing a photocatalytic degradation reaction, it is essential to know what the primary intermediate products are. The most reliable and accurate information is gathered through calculations carried out with quantum mechanical methods. Thus, since the yield produced is the same, the photocatalytic degradation reaction of transition state complexes and their hydroxy derivatives is based on the direct reaction of these molecules with the OH radical. With this aim, the kinetics of the reactions of the complexes and complexes derivatives with OH radicals was theoretically analyzed. The study was initiated with complexes and then exposed to an OH radical reaction and the reaction of the yield was modelled at the gas phase. The experimental findings in the scientific literature show that OH radicals detach a hydrogen atom from the saturated hydrocarbons and OH is added to the unsaturated hydrocarbons and materials of the aromatic structure [18,19]. For this purpose, all the possible reaction paths for the analyzed reactions were determined, for every reaction path molecular orbital calculations of the reactant, yield and transition state complexes were carried out with the AM1, PM3, HF and DFT methods, their molecular orbital calculations were realized and their geometries were optimized.

Kinetic Data Treatment

The aim of this study was to develop a model providing the outcome of the yield distribution of the photocatalytic degradation reactions. The vibration frequencies, the thermodynamic and electronic features of every structure were calculated using the obtained optimum geometric parameters. Afterwards, the rate constant and activation energy of every reaction was calculated using the Transition State Theory for a temperature of 25°C based on the quantum mechanical calculation results.

In order to find out the reaction rate, it is necessary to calculate the equilibrium constant. The equilibrium constant is calculated using the partition functions in accordance with the mechanical methods. If the equilibrium constant K_{\neq} is written in terms of partition functions, it is as follows:

$$K^\ddagger = \frac{q^\ddagger}{q_A' q_B'} \quad (1)$$

q^\ddagger , q_A , q_B : partition functions belonging to the transition state complex and reactants. The molecular partition function is as given below:

$$q' = q e^{-E_a(RT)^{-1}} \quad (2)$$

E_a represents the activation energy, the difference between the zero point energies of the transition state complex and the reactants [18,20].

$$k = \frac{k_B T}{h} \frac{q^\ddagger}{q_A q_B} e^{-E_a(RT)^{-1}} \quad (3)$$

k_B : Boltzmann constant

h : Planck constant

T : absolute temperature

In order to be able to calculate the rate constant, it is necessary to initially calculate the partition function of the activated complex. To realize this calculation, it is essential to know the geometry of the complex and moments of inertia. In addition, E_a should be known in order to find out the rate constant. The activation energy like the vibration frequency can only be calculated quantum mechanically.

The most probable reaction path and yield distribution of the OH radical of every molecule was determined by comparing the obtained results. The optimized geometric structures were drawn via GaussView 5 and the calculations were done via the Gaussian 09 packet programme [18,21].

Methodology

Experimental studies were carried out recently for oxidative degradation mechanisms of aromatic pollutants and monitoring the intermediate products formed during degradation. Rapidly evolving computer technology has entered into the workspace of the chemist and it has become inevitable to support the experimental results with theoretical calculations. Methods widely used today for chemical purposes can be made more practical utilizing calculations in package software. Both methods for calculating molecular and electronic structures use the same calculations; namely they calculate the energy of a particular molecular structure and make the geometric optimization (find the lowest energy molecular structure and equilibrium geometry). Geometry optimizations are fundamentally based on the energy gradient that is the first derivative of the energy according to its position [22].

The reaction system under consideration consists of \bullet OH radicals that are open-shell species. It is well-known that open-shell molecules pose

severe problems in quantum mechanical calculations. Therefore, the geometry optimization of the reactants, the product radicals, pre-reactive and transition state complexes were performed by the AM1, PM3, HF and DFT methods with the Gaussian 09 package [18,21].

Electronic structure methods use the laws of quantum mechanics rather than the laws of classical physics. These methods are characterized by different approaches to the mathematical methods. The electronic structure methods, semiempirical methods and ab-initio methods are parts of two main groups. The AM1 and PM3 method are semiempirical methods that we use in this study. Ab-initio methods do not use experimental data except for the basic physical constants (speed of light, Planck's constant, the mass of the electron, ... etc) of the molecules of interest unlike the molecular mechanics and the semiempirical method. Only the valence electrons are taken into account in the calculation and the basic functions are defined by Slater-type orbitals [23].

DFT methods use the exact electron density to calculate the molecular properties and energies, taking the electron correlation into account. They do not suffer from spin contamination and this feature makes them suitable for calculations involving open-shell systems. The DFT calculations were carried out by the hybrid B3LYP functional, which combines HF and Becke exchange terms with the Lee–Yang–Parr correlation functional.

The choice of the basis set is very important in such calculations. Based on these results, optimizations in the present study were performed at the B3LYP/6-31G(d) level. Forming C–O bonds in the addition paths and the H–O bond in the abstraction path were chosen as the reaction coordinates in the determination of the transition states. Ground-state and transition-state structures were confirmed by frequency analyses at the same level. Transition structures were characterized by having one imaginary frequency that belonged to the reaction coordinate, corresponding to a first-order saddle point. Zero-point vibrational energies (ZPEs) were calculated at the B3LYP/6-31G(d) level [2,18].

In recent years, the density functional theory (DFT) based on these methods has become very popular. The best DFT method requires less computing power than the conventional correlation method. This method is widely preferred for systems with too many atoms and makes calculations for a shorter time compared to other ab-initio methods. Generally, such ab-initio or DFT

is used to create the initial structure for the optimization in large systems. It used to obtain the qualitative information such as molecular orbitals, atomic loads and vibrational modes of a molecule and to predict the energy on conformation and substituent effects [22].

Solvent effect model

In aqueous media, water molecules affect the energetics of the degradation reactions of all organic compounds. Moreover, H₂O induces geometry relaxation on the solutes. The latter effect becomes more important when hydrogen-bonded complexes are present. However, the results obtained in earlier studies indicate that geometry changes have a negligible effect on the energy of the solute in water for both open- and closed-shell structures [18,24,25]. In this study, to take into account the effect of H₂O on the energetics and the kinetics of the aminotoluene + •OH reactions, DFT/B3LYP/6-31+G(d) calculations were carried out for the optimized structures of the reactants, the pre-reactive and the transition state complexes and the product radicals, by using COSMO (conductor-like screening solvation model) [18,25] as the solvation model, implemented in the Gaussian 09 package. The solvent was water at 25°C, with a dielectric constant $\epsilon = 78.39$ [18,22].

COSMO is one of the polarizable continuum methods (PCMs). In PCMs, the solute molecule is placed in a cavity surrounded by a polarizable continuum, whose reaction field modifies the energy and the properties of the solute [18,26]. The geometry of the cavity is determined by the shape of the solute. The reaction field is described in terms of the apparent polarization charges or reaction field factors included in the solute Hamiltonian, so that it is possible to perform iterative procedures leading to self-consistence between the solute wave-function and the solvent polarization. The COSMO method describes the solvent reaction field by means of apparent polarization charges distributed on the cavity surface, which are determined by assuming that the total electrostatic potential cancels out at the surface. This condition can describe the solvation in polar liquids. Hence, it is the method of choice in this study [2,18].

RESULTS AND DISCUSSION

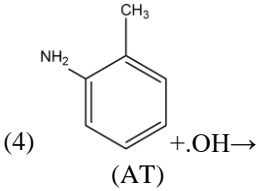
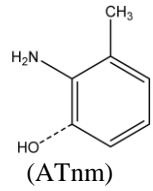
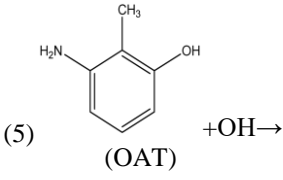
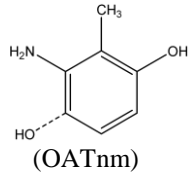
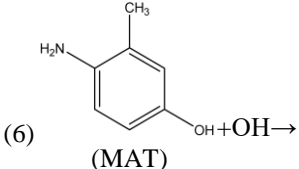
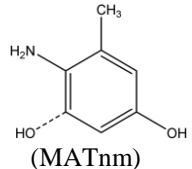
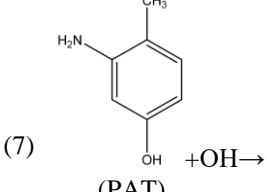
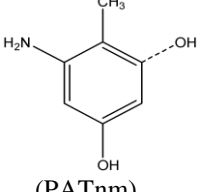
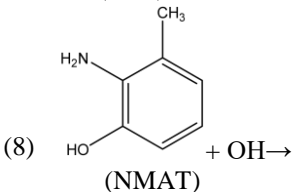
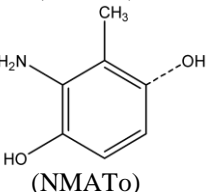
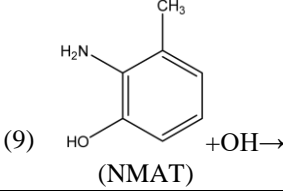
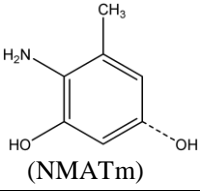
Computational modelling

Reaction paths

The hydroxyl radical is a very active species and has a strong electrophilic character. [18,27]. Once

formed, it can readily attack the aminotoluene molecule and produce the reaction intermediates. •OH radical reactions with aromatic compounds proceed through the following reaction pathway: H-atom abstraction from C–H bonds and addition to aromatic rings. [18,28] Based on previous results the 6,7,8,9,18,19,29 path for the reaction of aminotoluene(AT) with •OH was determined.

Table 1. The reaction paths of the most stable TST complexes of AT with •OH.

| OH addition | TST |
|--|--|
| (4)  (AT) + •OH → |  (ATnm) |
| (5)  (OAT) + •OH → |  (OATnm) |
| (6)  (MAT) + •OH → |  (MATnm) |
| (7)  (PAT) + •OH → |  (PATnm) |
| (8)  (NMAT) + •OH → |  (NMATo) |
| (9)  (NMAT) + •OH → |  (NMATm) |

The path m- addition to NH₂ (ATnm) with TS to the AT molecule is shown in table 1.[4]. Based on previous results the path for the reaction of 3-hydroxy-2- methyl aniline (OAT) with •OH was determined. The path m- addition to NH₂ (OATnm) with TS to a OAT molecule is shown

table 1.(5). Based on previous results the path for the reaction of 4-hydroxy-2- methyl aniline (MAT) with •OH was determined. The path m-addition to NH₂ (MATnm) with TS to a MAT molecule is shown in table 1.[6].

Based on previous results the path for the reaction of 5-hydroxy-2- methyl aniline (PAT) with •OH was determined. The path m- addition to NH₂ (PATnm) with TS to a PAT molecule is shown in table 1.(7). Based on previous results two different paths for the reaction of 2-hydroxy-6- methyl aniline (NMAT) with •OH were determined. The first two paths, o-addition (NMATo) and m-addition (NMATm) with TS to a NMAT molecule are shown in table 1. [8.9].

Transition State Complexes

In this study, reactants were used to find out the transition state complexes. An estimation of the initial geometry was done according to the type of reaction path using the optimum geometric parameters of the reactants. A C-O bond was chosen as the reaction coordinate while modelling the transition state complexes for the reactions realized with OH addition and the bond length was changed as 1.850-2.500 Å during calculation. The emerging OH bond length was chosen as the reaction path, and in order to determine the position of the OH radical according to the molecule, the dihedral angles belonging to this group were changed during the calculations. The activation energies and their most determined state in

thermodynamic terms for the gas phase and aqueous media were calculated for the probable reaction paths of all transition state complexes [18].

According to Fig.1, the C-O bond lengths at four probable transition states of the OH radical were taken as precise measurements. The bond lengths were calculated as (a) ATnm (3.63 Å), (b) OATnm (2.70 Å), (c) MATnm (2.64 Å), (d) PATnm (2.91 Å), (e) NMATo (2.06 Å), (f) NMATm (2.14 Å) relatively. The longest C-O bond belongs to the ATnm TS molecule and it is found that it occurs later compared to the others. Therefore, it is the most probable transition state.

CONCLUSIONS

It is possible that much more harmful intermediates than the ones at the beginning may occur given photocatalytic reactions of organic pollutants. The primary substances of such organic pollutants are polyaromatic substances. Thus, before realizing the photocatalytic degradation reaction experimentally, it is essential to know what the primary intermediates are. This information gives the most reliable and accurate calculations made by the quantum mechanical methods. Therefore, since the final product is the same, the photocatalytic degradation reaction of the transition state complexes and hydroxy derivatives are both based on the direct reaction with the OH radical of the transition state complexes.

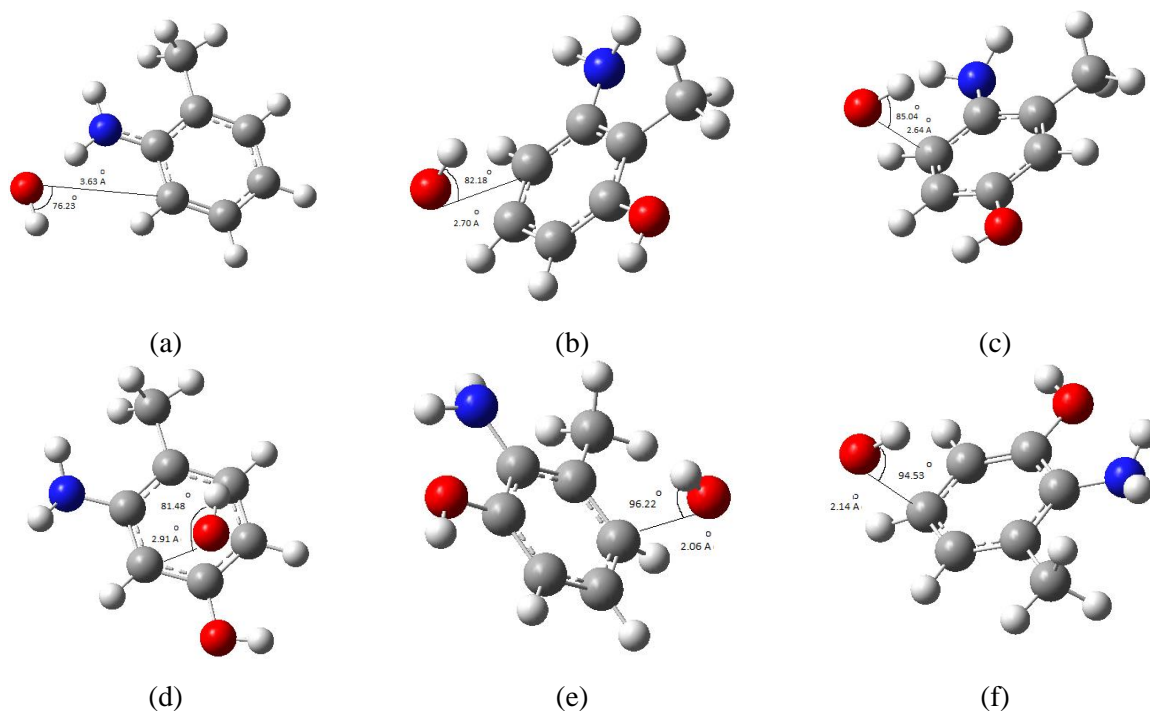


Fig. 1. Optimized structures of the transition state complexes of probable reaction paths (4-9): (a) ATnm, (b) OATnm, (c) MATnm, (d) PATnm, (e) NMATo, (f) NMATm

Table2. According to the DFT method the constant k, entropy, enthalpy and Gibbs free energy values.[18].

| DFT | $\Delta H(10^2)$ (kcal mol ⁻¹) | $\Delta G(10^2)$ (kcal mol ⁻¹) | ΔS (kcal mol ⁻¹ K ⁻¹) | k | $\Delta E (10^2)$ (kcal mol ⁻¹) |
|-------|---|---|---|------------------------|--|
| AT | 0.964 | 0.718 | 0.082 | ----- | 0.958 |
| ATo | 1.047 | 0.765 | 0.095 | 1.145x10 ¹¹ | 1.041 |
| ATm | 1.042 | 0.749 | 0.098 | 3.738x10 ⁸ | 1.036 |
| ATp | 1.046 | 0.764 | 0.094 | 1.568x10 ⁹ | 1.040 |
| ATnm | 1.033 | 0.747 | 0.096 | 2.257x10 ¹² | 1.028 |
| OAT | 0.998 | 0.735 | 0.088 | ----- | 0.992 |
| OATm | 1.084 | 0.798 | 0.096 | 6.028x10 ¹⁵ | 1.078 |
| OATp | 1.079 | 0.779 | 0.101 | 1.376x10 ⁹ | 1.073 |
| OATnm | 1.079 | 0.778 | 0.101 | 1.005x10 ⁹ | 1.073 |
| MAT | 0.997 | 0.733 | 0.089 | ----- | 0.991 |
| MATo | 1.078 | 0.777 | 0.101 | 2.386x10 ¹⁰ | 1.072 |
| MATp | 1.079 | 0.779 | 0.101 | 1.905x10 ¹⁰ | 1.073 |
| MATnm | 1.076 | 0.772 | 0.102 | 9.504x10 ⁴ | 1.070 |
| PAT | 0.997 | 0.735 | 0.088 | ----- | 0.991 |
| PATo | 1.072 | 0.775 | 0.100 | 0.000 | 1.066 |
| PATm | 1.083 | 0.798 | 0.096 | 4.015x10 ¹⁵ | 1.077 |
| PATnm | 1.075 | 0.769 | 0.103 | 1.139x10 ¹⁰ | 1.069 |
| NMAT | 0.998 | 0.735 | 0.088 | ----- | 0.992 |
| NMATo | 1.080 | 0.781 | 0.101 | 5.070x10 ¹⁰ | 1.074 |
| NMATm | 1.080 | 0.778 | 0.101 | 2.505x10 ¹¹ | 1.074 |

In Table 2, according to the DFT method, the constant k and entropy have the highest values, the enthalpy and Gibbs free energy values are the lowest, the transition state of ATnm, OATnm, MATnm, PATnm, NMATo and NMATm are concluded to be the most stable and have the lowest energy transition of the complexes [18].

In this study, the analysis of the reaction kinetics of the most stable transition state complexes of the aminotoluene molecule by the theoretical methods was calculated. The DFT method is the most appropriate method of the theoretical methods used. The basic principle of DFT, is that the total electronic energy of the molecule is formed in connection with the total electronic density. Compared to other methods, this gives more accurate results that account for all the properties of the nucleus and electrons.

In Table 3, the activation energy levels of Ea in the gas phase of the TS molecules having the lowest energy for the DFT method for every transition state complex are given below:

-7.404 kcal mol⁻¹ of ATnm for AT, -3.077 kcal mol⁻¹ of OATm for OAT, -5.131 kcal mol⁻¹ of MATnm for MAT, -4.049 kcal mol⁻¹ of PATnm for PAT, -5.402 kcal mol⁻¹ of NMATo for NMAT and -6.359 kcal mol⁻¹ of NMATm for NMAT are the transition state complexes with the lowest energy. These

reveal the most probable transition state complexes in the gas phase. The most rapid occurring transition state complex in the gas phase has the highest values of the k rate constant. Ea_{ecosmo} aqueous media activation energy levels for the DFT method at 1.927x10¹ kcal mol⁻¹ of ATnm for AT, 1.856x10² kcal mol⁻¹ of OATnm for OAT, 0.673x10¹ kcal mol⁻¹ of MATnm for MAT, 0.763x10¹ kcal mol⁻¹ of PATnm for PAT, 0.210x10¹ kcal mol⁻¹ of NMATo for NMAT and 0.607x10¹ kcal mol⁻¹ of NMATm for NMAT are the transition state complexes with the lowest energy.

This reveals that it is the most probable transition state at aqueous media. Hydroxyl radicals are used in order to remove the organic contaminants from water. In this study, the most probable reaction paths were determined to be OH radicals added to the aromatic ring.

Organic contaminants exist at very low concentrations in water [3,18]. Therefore, it is essential to remove the organic contaminants from the drinking water [4,18]. The hydroxyl radical, which is the most reactive type known in biological systems, reacts with every biomolecule it encounters including water. Potentially, every biomolecule is a hydroxyl radical scavenger at a different speed [8,18].

Table 3. Constant k, for gas phase and aqueous media activation energy levels calculated via AM1, PM3, HF, DFT methods

| ATnm | Ea(kcal mol ⁻¹) | k | Ea _{ecosmo} (kcal mol ⁻¹) |
|-------|-----------------------------|------------------------|--|
| AM1 | -1.671 | 1.280x10 ⁸ | 2.146x10 ¹ |
| PM3 | 1.634 | 2.729x10 ⁵ | 2.770x10 ¹ |
| HF3 | 5.833 | 1.227x10 ² | 3.749x10 ¹ |
| HF6 | 8.494 | 1.794 | 4.493x10 ¹ |
| DFT | -7.404 | 2.257x10 ¹² | 1.927x10 ¹ |
| OATnm | Ea(kcal mol ⁻¹) | k | Ea _{ecosmo} (kcal mol ⁻¹) |
| AM1 | 0.337 | 6.805x10 ⁶ | 2.165x10 ² |
| PM3 | 2.922 | 4.969x10 ⁴ | 1.835x10 ² |
| HF3 | 1.055x10 ¹ | 0.070 | 2.196x10 ² |
| HF6 | 1.251x10 ¹ | 2.687x10 ⁻³ | 2.140x10 ² |
| DFT | -3.077 | 1.005x10 ⁹ | 1.856x10 ² |
| MATnm | Ea(kcal mol ⁻¹) | k | Ea _{ecosmo} (kcal mol ⁻¹) |
| AM1 | 0.808 | 1.742x10 ⁶ | 0.864x10 ¹ |
| PM3 | 2.200 | 2.607x10 ⁵ | 1.039x10 ¹ |
| HF3 | 5.522 | 6.091x10 | 1.921x10 ¹ |
| HF6 | 9.463 | 0.401 | 2.499x10 ¹ |
| DFT | -5.131 | 9.504x10 ⁴ | 0.673x10 ¹ |
| PATnm | Ea(kcal mol ⁻¹) | k | Ea _{ecosmo} (kcal mol ⁻¹) |
| AM1 | -2.015 | 2.246x10 ⁸ | 0.962x10 ¹ |
| PM3 | 2.304 | 2.116x10 ⁵ | 1.132x10 ¹ |
| HF3 | 8.631 | 1.438 | 2.078x10 ¹ |
| HF6 | 1.016x10 ¹ | 0.117 | 2.634x10 ¹ |
| DFT | -4.049 | 1.139x10 ¹⁰ | 0.763x10 ¹ |
| NMATo | Ea(kcal mol ⁻¹) | k | Ea _{ecosmo} (kcal mol ⁻¹) |
| AM1 | -0.605 | 2.707x10 ⁷ | 0.731x10 ¹ |
| PM3 | 2.619 | 1.171x10 ⁵ | 0.702x10 ¹ |
| HF3 | -2.222 | 1.075x10 ⁹ | 1.298x10 ¹ |
| HF6 | 1.059x10 ¹ | 0.072 | 1.840x10 ¹ |
| DFT | -5.402 | 5.070x10 ¹⁰ | 0.210x10 ¹ |
| NMATm | Ea(kcal mol ⁻¹) | k | Ea _{ecosmo} (kcal mol ⁻¹) |
| AM1 | -1.698 | 1.954x10 ⁸ | 0.413x10 ¹ |
| PM3 | 2.475 | 1.744x10 ⁵ | 0.665x10 ¹ |
| HF3 | 7.262 | 1.165x10 ¹ | 1.867x10 ¹ |
| HF6 | 1.015x10 ¹ | 0.110 | 2.365x10 ¹ |
| DFT | -6.359 | 2.505x10 ¹¹ | 0.607x10 ¹ |

Table 4. Mulliken loads of the heavy atoms of the studied molecules.¹⁸

| AT | ATnm | OAT | OAT nm |
|----------------|----------------|----------------|----------------|
| 11 C -0.079158 | 11 C -0.063830 | 10 C -0.062126 | 10 C -0.041225 |
| 15 N -0.152651 | 15 N -0.068889 | 14 N -0.151131 | 14 N -0.145082 |
| | 18 O -0.231787 | 17 O -0.246327 | 17 O -0.240589 |
| | | | 19 O -0.211082 |
| MAT | MATnm | PAT | PATnm |
| 10 O -0.253210 | 10 O -0.243592 | 10 C -0.086504 | 10 C -0.074263 |
| 12 N -0.160178 | 12 N -0.150491 | 14 N -0.152124 | 14 N -0.144674 |
| 15 C -0.074152 | 15 C -0.063696 | 17 O -0.245155 | 17 O -0.229721 |
| | 19 O -0.097024 | | 19 O -0.097927 |
| NMAT | NMATo | NMATm | |
| 10 C -0.076104 | 10 C -0.050241 | 10 C -0.066739 | |
| 14 O -0.262806 | 14 O -0.239830 | 14 O -0.256092 | |
| 16 N -0.141021 | 16 N -0.133101 | 16 N -0.114022 | |
| | 19 O -0.220675 | 19 O -0.223159 | |

Aromatic compounds are good detectors since they hydroxylate. In addition, the position of attack to the ring depends on the electron withdrawal and repulsion of the previously present substituents [9,18]. When the Mulliken loads in table 4 are analyzed, the electronegativities of the N and O atoms yield information about the bonding state of the OH radical.

Acknowledgements: The authors greatly appreciate the financial support of the Namik Kemal University Research Foundation. Project number: NKUBAP.00.10.AR.12.05.

REFERENCES

1. B.J. Finlayson-Pitts, J.N. Pitts Jr., Chemistry of the Upper and Lower Atmosphere, Academic Press, San Diego, 2000.
2. A. Hatipoglu, D. Vione, Y. Yalçın, C. Minero, Z. Çınar, *Journal of Photochemistry and Photobiology A: Chemistry*, **215**, 59 (2010).
3. K. Verschuere, "Handbook of Environmental Data on Organic Chemicals" Second Ed., Van Nostrand Reinhold Company, New York, 1983.
4. J. C. English, V. S. Bhat, G. L. Ball, C. J. McLellan, *Original Research Article Regulatory Toxicology and Pharmacology*, **64**, 2, 269 (2012).
5. R.W. Matthews, D.F. Ollis, H. Al-Ekabi, Photocatalytic Purification and Treatment of Water and Air, Elsevier Science Publishers, 1993, p. 121.
6. A. Taicheng, L. Sun, G. Li, S. Wan, *Journal of Molecular Catalysis A: Chemical*, **333**(1–2), 128 (2010).
7. V.G. Buxton, L.C. Greenstock, P.W. Helman, B.A. Ross, *Journal of Physical and Chemical Reference Data*, **17**, 513 (1988).
8. M. Anbar, P. Neta, *Int. J. Radiat Isot*, **18**, 495 (1965).
9. B. Halliwell, M. Grootveld, J.M.C. Gutteridge, 1988, *Methods of Biochemical Analysis*, 33, 59. Laidler K.J and Meiser, J.H, Physical Chemistry, The Benjamin/Cummings Publishing Company Inc., California, 1982.
10. M. J. O'Neil, Whitehouse Station, NJ: Merck & Co. Inc.: The Merck Index, 14th ed.; Editor, O'Neil M J., 2006, p. 1639.
11. C. Alba-Simionesco, J. Fan, C.A. Angell, *J. Chem. Phys.* **110**, 5262, (1999).
12. G. Pratesi, P. Bartolini, D. Senatra, M. Ricci, R. Righini, F. Barocchi, R. Torre. *Physical Review E* : **67**, 021505 (2003).
13. *IARC Monogr Eval Carcinog Risks Hum*, **99**, 1 (2010). PMID:21528837
14. *IARC Monogr Eval Carcinog Risk Chem Man*, **16**, 1 (1978).
15. *IARC Monogr Eval Carcinog Risks Chem Hum*, **27**, 1 (1982). PMID:6955259
16. *IARC Monogr Eval Carcinog Risks Hum Suppl*, **7**, 1 (1987). PMID:3482203
17. *IARC Monogr Eval Carcinog Risks Hum*, **77**, 1 (2000). PMID:11236796
18. B. Eren, Y.Yalçın Gurkan, *Bulg. Chem. Commun.* **47**(3), 849, (2015).
19. P.W. Atkins, Physical Chemistry, 6th edition, Oxford University Press, 1998, P.W. Atkins, R.S. Friedman, Molecular Quantum Mechanics, 3rd Ed., Oxford University Press Inc., New York, 1997.
20. I.N. Levine Quantum Chemistry, Allyn and Bacon Inc., Boston 1983, I.N. Levine, Quantum Chemistry i, Allyn and Bacon, Boston MA, 1991, J.P. Lowe, Quantum Chemistry, 2nd Ed., Academic Press, USA 1993.
21. M.J. Frisch, G.W. Trucks, H.B. Schlegel, G.E. Scuseria, M.A. Robb, J.R. Cheeseman, J.A. Montgomery Jr., T. Vreven, K.N. Kudin, J.C. Burant, J.M. Millam, S.S. Iyengar, J. Tomasi, V. Barone, B. Mennucci, M. Cossi, G. Scalmani, N. Rega, G.A. Petersson, H. Nakatsuji, M. Hada, M. Ehara, K. Toyota, R. Fukuda, J. Hasegawa, M. Ishida, T. Nakajima, Y. Honda, O. Kitao, H. Nakai, M. Klene, X. Li, J.E. Knox, H.P. Hratchian, J.B. Cross, C. Adamo, J. Jaramillo, R. Gomperts, R.E. Stratmann, O. Yazyev, A.J. Austin, R. Cammi, C. Pomelli, J.W. Ochterski, P.Y. Ayala, K. Morokuma, G.A. Voth, P. Salvador, J.J. Dannenberg, V.G. Zakrzewski, S. Dapprich, A.D. Daniels, M.C. Strain, O. Farkas, D.K. Malick, A.D. Rabuck, K. Raghavachari, J.B. Foresman, J.V. Ortiz, Q. Cui, A.G. Baboul, S. Clifford, J. Cioslowski, B.B. Stefanov, G. Liu, A. Liashenko, P. Piskorz, I. Komaromi, R.L. Martin, D.J. Fox, T. Keith, M.A. Al-Laham, C.Y. Peng, A. Nanayakkara, M. Challacombe, P.M.W. Gill, B. Johnson, W. Chen, M.W. Wong, C. Gonzalez, J.A. Pople, Gaussian 09, Revision B.04, Gaussian, Inc., Pittsburgh, PA, 2009.
22. J.B. Foresman, M.J. Frisch, Exploring Chemistry with Electronic Structure Methods, Gaussian Inc., Pittsburgh, PA, 1996.
23. P. Popelier, Pearson Education: Atom in Molecules, USA, 2000.
24. J. Andzelm, C. Kölmel, A. Klamt, *J. Chem. Phys.* **103**, 9312 (1995).
25. V. Barone, M. Cossi, *J. Phys. Chem. A.*, **102**, 11 (1998).
26. N.S. Hush, J. Schamberger, G.B. Bacskay, *Coord. Chem. Rev.* **249**, 299, (2005).
27. V. Brezová, M. Ceppan, E. Brandsteterova, M. Breza, L. Lapcik, *J. Photochem. Photobiol. A: Chem.* **59**, 3 (1991).
28. M. Kılıç, G. Koçturk, N. San, Z. Çınar, *Chemosphere*, **69**, 9, 1396 (2007).
29. I. Suh, D. Zhang, R. Zhang, L.T. Molina, M.J. Molina, *Chem. Phys. Lett.* **364**, 454 (2002).

НАЙ-СТАБИЛНИТЕ ПРЕХОДНИ СЪСТОЯНИЯ НА МОЛЕКУЛАТА НА АМИНО-ТОЛУЕНА

Б. Ерен¹, Й.Й. Гуркан^{2*}

¹Университет „Намик Кемал“, Факултет по земеделие, Текирдаг, Турция

²Университет „Намик Кемал“, Департамент по химия, Текирдаг, Турция

Постъпила на 15 януари, 2016 г.; коригирана на 8 февруари, 2016 г.

(Резюме)

В тази работа са анализирани най-вероятните маршрути за преходните състояния АТ_{nm}, ОАТ_{nm}, МАТ_{nm}, РАТ_{nm}, NМАТ_o и NМАТ_m с ОН-радикали. Оптимизираната геометрия на комплексите е определена чрез геометрична оптимизация с помощта на софтуера Gaussian 09. Анализът на геометричната структура и дължината на връзките също са изчислени. Тази работа има за цел да се определят най-вероятните пътища за разпределението на преходните комплекси и взаимодействията с ОН-радикали в газова фаза и във водна среда. Използвани са квантово-механични методи за посочването на влиянието на скоростта на реакцията върху първичните, хидроксилираните междинни съединения и накрая – въздействието на разтворителя (водата). За определянето на междинните съединения при разлагането на преходните комплекси е използвана геометрична оптимизация с полу-емпирични методи (AM1 и PM3), *ab initio* Hartree-Fock HF/3-21G, HF/6-31G* и Density Functional Theory (DFT). Сравнени са и теоретично са оценени най-подходящия метод и неговата надеждност. Най-вероятните скоростни константи на реакционните пътища са изчислени с помощта на терията на преходните състояния (TST). За определянето на преходното състояние на реакцията е взета връзката С-О за база. Изчислена е активиращата енергия на вероятните реакции за всички преходни комплекси и най-стабилните им състояния от термодинамична гледна точка за газова фаза и течна среда. Изследвано е влиянието на водата като разтворител при използването на COSMO като солватационен модел.

BULGARIAN CHEMICAL COMMUNICATIONS

Instructions about Preparation of Manuscripts

General remarks: Manuscripts are submitted in English by e-mail or by mail (in duplicate). The text must be typed double-spaced, on A4 format paper using Times New Roman font size 12, normal character spacing. The manuscript should not exceed 15 pages (about 3500 words), including photographs, tables, drawings, formulae, etc. Authors are requested to use margins of 3 cm on all sides. For mail submission hard copies, made by a clearly legible duplication process, are requested. Manuscripts should be subdivided into labelled sections, e.g. **Introduction, Experimental, Results and Discussion**, etc.

The title page comprises headline, author's names and affiliations, abstract and key words.

Attention is drawn to the following:

a) **The title** of the manuscript should reflect concisely the purpose and findings of the work. Abbreviations, symbols, chemical formulas, references and footnotes should be avoided. If indispensable, abbreviations and formulas should be given in parentheses immediately after the respective full form.

b) **The author's** first and middle name initials, and family name in full should be given, followed by the address (or addresses) of the contributing laboratory (laboratories). **The affiliation** of the author(s) should be listed in detail (no abbreviations!). The author to whom correspondence and/or inquiries should be sent should be indicated by asterisk (*).

The abstract should be self-explanatory and intelligible without any references to the text and containing not more than 250 words. It should be followed by key words (not more than six).

References should be numbered sequentially in the order, in which they are cited in the text. The numbers in the text should be enclosed in brackets [2], [5, 6], [9–12], etc., set on the text line. References, typed with double spacing, are to be listed in numerical order on a separate sheet. All references are to be given in Latin letters. The names of the authors are given without inversion. Titles of journals must be abbreviated according to Chemical Abstracts and given in italics, the volume is typed in bold, the initial page is given and the year in parentheses. Attention is drawn to the following conventions:

a) The names of all authors of a certain publications should be given. The use of “*et al.*” in

the list of references is not acceptable.

b) Only the initials of the first and middle names should be given.

In the manuscripts, the reference to author(s) of cited works should be made without giving initials, e.g. “Bush and Smith [7] pioneered...”. If the reference carries the names of three or more authors it should be quoted as “Bush *et al.* [7]”, if Bush is the first author, or as “Bush and co-workers [7]”, if Bush is the senior author.

Footnotes should be reduced to a minimum. Each footnote should be typed double-spaced at the bottom of the page, on which its subject is first mentioned.

Tables are numbered with Arabic numerals on the left-hand top. Each table should be referred to in the text. Column headings should be as short as possible but they must define units unambiguously. The units are to be separated from the preceding symbols by a comma or brackets.

Note: The following format should be used when figures, equations, etc. are referred to the text (followed by the respective numbers): Fig., Eqns., Table, Scheme.

Schemes and figures. Each manuscript (hard copy) should contain or be accompanied by the respective illustrative material as well as by the respective figure captions in a separate file (sheet). As far as presentation of units is concerned, SI units are to be used. However, some non-SI units are also acceptable, such as °C, ml, l, etc.

The author(s) name(s), the title of the manuscript, the number of drawings, photographs, diagrams, etc., should be written in black pencil on the back of the illustrative material (hard copies) in accordance with the list enclosed. Avoid using more than 6 (12 for reviews, respectively) figures in the manuscript. Since most of the illustrative materials are to be presented as 8-cm wide pictures, attention should be paid that all axis titles, numerals, legend(s) and texts are legible.

The authors are asked to submit **the final text** (after the manuscript has been accepted for publication) in electronic form either by e-mail or mail on a 3.5” diskette (CD) using a PC Word-processor. The main text, list of references, tables and figure captions should be saved in separate files (as *.rtf or *.doc) with clearly identifiable file names. It is essential that the name and version of

the word-processing program and the format of the text files is clearly indicated. It is recommended that the pictures are presented in *.tif, *.jpg, *.cdr or *.bmp format, the equations are written using "Equation Editor" and chemical reaction schemes are written using ISIS Draw or ChemDraw programme.

The authors are required to submit the final text with a list of three individuals and their e-mail addresses that can be considered by the Editors as potential reviewers. Please, note that the reviewers should be outside the authors' own institution or organization. The Editorial Board of the journal is not obliged to accept these proposals.

EXAMPLES FOR PRESENTATION OF REFERENCES

REFERENCES

1. D. S. Newsome, *Catal. Rev.–Sci. Eng.*, **21**, 275 (1980).
2. C.-H. Lin, C.-Y. Hsu, *J. Chem. Soc. Chem. Commun.*, 1479 (1992).
3. R. G. Parr, W. Yang, *Density Functional Theory of Atoms and Molecules*, Oxford Univ. Press, New York, 1989.
4. V. Ponec, G. C. Bond, *Catalysis by Metals and Alloys* (Stud. Surf. Sci. Catal., vol. 95), Elsevier, Amsterdam, 1995.
5. G. Kadinov, S. Todorova, A. Palazov, in: *New Frontiers in Catalysis* (Proc. 10th Int. Congr. Catal., Budapest, 1992), L. Guzzi, F. Solymosi, P. Tetenyi (eds.), Akademiai Kiado, Budapest, 1993, Part C, p. 2817.
6. G. L. C. Maire, F. Garin, in: *Catalysis. Science and Technology*, J. R. Anderson, M. Boudart (eds), vol. 6, Springer-Verlag, Berlin, 1984, p. 161.
7. D. Pocknell, *GB Patent 2 207 355* (1949).
8. G. Angelov, PhD Thesis, UCTM, Sofia, 2001.
9. JCPDS International Center for Diffraction Data, Power Diffraction File, Swarthmore, PA, 1991.
10. *CA* **127**, 184 762q (1998).
11. P. Hou, H. Wise, *J. Catal.*, in press.
12. M. Sinev, private communication.
13. <http://www.chemweb.com/alchem/articles/1051611477211.html>.

CONTENTS

| | |
|--|-----|
| S. Zhou, H. Kuai, Y. Gu, W. Zhou, A. Li, Mechanism of hydrogen transfer from 1-methylbutyl peroxide to hydroxyl radical | 359 |
| S. Salahi, M. T. Maghsoodlou, N. Hazeri, M. Lashkari, R. Doostmohammadi, A. Kanipour, F. Farhadpour, A. Shojaei, Two ammonium ionic liquids as efficient catalysts for the one-pot green synthesis of 3,4,5-substituted furan-2(5H)-ones | 364 |
| M. T. Maghsoodlou, M. Karima, M. Lashkari, B. Adrom, N. Hazeri, Convenient approach for the one-pot, three-component synthesis of 1-(benzothiazolylamino)methyl-2-naphthol using fumaric acid as a green catalyst | 369 |
| M. Alikarami, M. Ghasemian, BTPPC-catalyzed one-pot synthesis of 1,4-dihydropyridine derivatives via Hantzsch condensation under solvent-free conditions | 373 |
| F. Kanwal, R. Rehman, S. Rasul, K. Liaqat, Chromium(VI) removal from water by using polyaniline biocomposites with <i>Madhuca longifolia</i> and <i>Szygium cumini</i> leaves | 379 |
| M. L. Valcheva-Traykova, G. S. Bocheva, Effect of ultraviolet radiation on the free radicals formation in hypothyroid rat's liver | 384 |
| R. Fazaeli, H ₃ PW ₁₂ O ₄₀ (PW ₁₂) encapsulated on cotton-like mesoporous (CLM) silica as an efficient, reusable nano photocatalyst for the decolorization of Rhodamine B..... | 389 |
| A. M. Amani, H. Sepehrian, A novel eco-friendly method for the synthesis of 2,3-dihydroquinazolin-4(1H)-ones in aqueous media under ultrasonication using ZrOCl ₂ -MCM-41 as a highly efficient nanocatalyst/nanoreactor | 395 |
| N. Singh, A. Ahmad, Spectroscopic studies of charge-transfer complexes of 2,3-dichloro-5,6-dicyano-p-benzoquinone with p-nitroaniline..... | 403 |
| M. Shoaib, S. W. A. Shah, N. Ali, I. Shah, M. N. Umar, Shafiullah, M. N. Tahir, M. Ghias, Synthetic flavone derivatives. An antibacterial evaluation and structure-activity relationship study | 414 |
| M. Bordbar, F. Khodaie, M. Tabatabaee, A.Y. Faal, Z. Mehrilighvan, S. M. Ganji, Interaction studies of DNA binding with a new Cu(II) complex by spectrophotometric, spectrofluorometric, voltammetric and circular dichroism techniques | 422 |
| A. Gholizadeh, A. Malekzadeh, M. Ghiasi, Structural, magnetic and catalytic properties of Co substituted manganite nano-perovskites | 430 |
| S. R. Hassan, N. Q. Zaman, I. Dahlan, Performance study of compartment-wise behaviour of modified anaerobic hybrid baffled (MAHB) reactor..... | 440 |
| D.A. Baiseitov, M.I. Tulepov, L.R. Sassykova, Sh.E. Gabdrashova, G.A. Essen, K.K. Kudaibergenov, Z.A. Mansurov, Sorption capacity of oil sorbent for the removal of thin films of oil | 446 |
| I. K. Mihailova, S. V. Dimitrova, D. D. Stoyanova, D. R. Mehandjiev, Influence of the carrier phase composition on the catalytic activity of copper-cobalt oxides deposited on slag glass-ceramics..... | 451 |
| S. Ivanova, D. Tsvetkova, Validation of a TLC-densitometric method for quality control in drug combinations | 456 |
| P. A. Gateva, V. T. Angelova, R. T. Georgieva-Nikolova, T. R. Veselinov, V. H. Nankova, M. M. Nikolova ⁵ , R. K. Hadjiolova, M. P. Slavova, Synthetic cannabimimetics detected in smoking blends on the Bulgarian territory – toxicological significance..... | 461 |
| Á. Révész, C. Szilágyi, T. Spassov, Hydrogen sorption of magnesium plates deformed by surface mechanical attrition treatment | 469 |
| M. Lefahal, M. Benahmed, L. Djarri, N. Zaabat, E. H. Anne, M. Kamel, M.-G. D. Franca, H. Laouer, S. Akkal, Chemical composition of <i>Limonium thouinii</i> (viv.) kuntze (plumbaginaceae) and the DPPH free radical scavenging activity | 476 |
| O. İsmail, Ö. G. Kocabay, Evaluation of the drying methods and conditions with respect to drying kinetics, colour quality and specific energy consumption of thin layer pumpkins | 480 |
| Z.-L. Yao, Y.-P. Pei, Z.-Y. Luo, R.-H. Hu, Y.-X. Yang, Wen-Tong Chen, Preparation, characterization and fluorescence of two cadmium compounds with different extended structures | 492 |
| W. Abbas, Hazem Ali Attia, Mostafa A. M. Abdeen, Non-darcy effect on non-newtonian Bingham fluid with heat transfer between two parallel plates | 497 |
| T. Mahmood ¹ , J. Ahmed ^{2*} , A. Shahzad ² , R. Ali ³ , Z. Iqbal, Convective heat transfer of viscous fluid over a stretching sheet embedded in a thermally stratified medium..... | 506 |
| E. A. Velcheva, Z. I. Glavcheva, B.A. Stamboliyska, IR spectral and structural changes caused by the conversion of acetanilide into azanion | 514 |
| A.I. Gisbrecht, M.M. Asimov, Kinetics of laser-induced photodissociation of oxyhemoglobin and its biomedical applications | 521 |
| A. Mirabi, M. R. Jamali, Q. Kazemi, Determination of trace amounts of manganese in water samples by flame atomic absorption spectrometry after dispersive liquid-liquid microextraction | 525 |
| Q.-W. Chang, J. Li, C.-X. Yan, J. Jiang, J.-L. Chen, Q.-S. Ye, J. Yu, W.-P. Liu, A new synthesis method and photophysical properties of Ir(C ^N) ₃ cyclometalated iridium phosphorescent complexes..... | 532 |

| | |
|--|-----|
| <i>Y. G. Wang, Y. J. Jing, Q. W. Wei, H. Ma, Y. L. Wang, X. L. Wang, F. F. Leng, Preparation and modification of peanut shells and their application for heavy metals adsorption</i> | 535 |
| <i>W. Gao, W. F. Wang, M. K. Jamil, R. Farooq, M. R. Farahani, Generalized atom-bond connectivity analysis of several chemical molecular graphs</i> | 543 |
| <i>W.L. Xu, Y.N. Yang, J.Wang, M. Tang, Y.Jian, X.J. Pei, Organic matter removal performance and mechanism in the Constructed Rapid Infiltration System.....</i> | 550 |
| <i>Y. B. Huang, Q. Qiu, C. Y. Niu, H. Q. Gao, C. Huang, S. X. Tu, Performance, synthesis and removal of Vanadium on Ferruginous Manganese composite material</i> | 558 |
| <i>M.W. Mushtaq, M. Imran, S. Bashir, F. Kanwal, L. Mitu, Synthesis, structural and biological studies of cobalt ferrite nanoparticles.....</i> | 565 |
| <i>B. Eren, Y. Y. Gurkan, The most stable transition state complexes of the aminotoluene molecule</i> | 571 |
| <i>INSTRUCTIONS TO THE AUTHORS</i> | 580 |

СЪДЪРЖАНИЕ

| | |
|---|-----|
| С.К. Жоу, Х.В. Куай, И.Х. Гу, В. Зоу, А.Р. Ли, Механизъм на преноса на водород от 1-метил-бутилов пероксид към хидроксилен радикал | 363 |
| С. Салахи, М.Т. Максудлу, Н. Хазери, М. Лашкари, Р. Дустмохамади, А. Канитур, Ф. Фархадпур, А. Шоджаеи, Две амониесви йонни течности като ефективни катализатори за едностадийна зелена синтеза на 3,4,5-заместени фуран-2(5h)-они | 368 |
| М.Т. Максудлу, М. Карима, М. Лашкари, Б. Адром, Н. Хазери, Удобен подход за едностадийна трикомпонентна синтеза на 1-(бензотиазоламино) метил-2-нафтол с фумарова киселина като зелен катализатор | 372 |
| М. Аликарими, М. Гасемян, ВТРС- катализирана едностадийна синтеза на 1,4-дихидропиридинови производни чрез кондензация на hantzsh без разтворител | 378 |
| Ф. Канвал, Р. Рехман, С. Расул, К. Лиакат, Отстраняване на хром (VI) от води с използването на полианилинови биокомпозици с листа от <i>Madhuca longifolia</i> и <i>Syzygium cumini</i> | 383 |
| М. Л. Вълчева-Трайкова, Г. С. Бочева, Ефект на ултравиолетовото облучване върху образуването на свободни радикали в черен дроб на плъхове с хипотиреоидизъм | 388 |
| Р. Фазаели, $\text{H}_3\text{PW}_{12}\text{O}_{40}$ (PW_{12}) капсулиран в памуко-подобен мезопорьозен силициев диоксид (CLM) като ефективен и многократно употребяван нано-фотокатализатор за обезцветяването на Rhodamine B..... | 394 |
| А.М. Аmani, Ю. Гасеми, А. Савардацаки, К. Зоморудиан, Е. Мирзаеи, Б. Заре, Х. Сеферман, Нов екологично съвместим метод за синтеза на 2,3-дихидрохиназолин-4(1h)-они във водна среда при ултразвуково въздействие, използвайки ZrOCl_2 -MCM-41 като високоефективен нанокатализатор/нанореактор | 402 |
| Н. Сингх, А. Ахмад, Спектроскопски изследвания на комплекси с пренос на заряда от 2,3-дихлоро-5,6-дициано-р-бензохинон с р-нитроанили..... | 413 |
| М. Шоахиб, С.У.А. Шах, Н. Али, И. Шах, М.Н. Умар, Шафиула, М.Н. Тахр, М. Гуас, Синтетични флавонови производни. антибактериални свойства и връзка между активност и структура | 421 |
| М. Бордбар, Ф. Ходайе, М. Табатабаеи, А. И. Фаал, З. Мехрилуван, С. Мохамед-Ганджи, Изследване на взаимодействието на ДНК с нов Cu(II) комплекс чрез спектроскопски, спектрофлуометрични, волтаперометрични методи и с кръгов дихроизъм | 429 |
| А. Голизаде, А. Малекзаде, М. Гуаси, Структурни, магнитни и каталитични свойства на кобалт-заместени мангантини перовскити | 439 |
| С.Р. Хасан, Н.К. Заман, И. Дахлан, Изследване на секционното поведение на модифициран анаеробен хибриден реактор с прегради (МАНВ)..... | 445 |
| Д.А. Байсейтов, М.И. Тулепов, Л.Р. Сасикова, Ш.Е. Габдрашова, Г.А. Есен, К.К. Кудайбергенов, З.А. Мансуров, Сорбционен капацитет на сорбенти за отстраняване на тънки слоеве от нефт | 450 |
| И.К. Михайлова, С.В. Димитрова, Д. Д. Стоянова, Д. Р. Механджиев, Влияние на фазовия състав на носителя върху каталитичната активност на медно-кобалтови оксиди нанесени върху шлакоситаги..... | 455 |
| С. Иванова, Д. Цветкова, Валидиране на TLC-дензитометричен метод за контрол на качеството на estradiol valerate в лекарствени комбинации..... | 460 |
| П. А. Гатева, В. Т. Ангелова, Р. Т. Георгиева-Николова, Ц. Р. Веселинов, В. Х. Нанкова, М. М. Николова, Р. К. Хаджиолова, М. П. Славова, Синтетични канабимиметици, установявани в смески за пушене на територията на България– токсикологично значение | 468 |
| А. Ревеш, Ц. Силаги, Т. Спасов, Сорбция на водород в магнезиеви пластини деформирани чрез повърхностно механично изтриване | 475 |
| М. Лефахал, М. Бенахмед, Л. Джари, Н. Заабат, А.Е. Хай, М. Камел, М.-Г. Дижу Франка, Х. Лауе, С. Аккал, Химичен състав на <i>Limonium thouinii</i> (viv.) kuntze (Plumbaginaceae) и DPPH-активността за отстраняване на свободни радикали..... | 479 |
| О. Исмаил, Й.Г. Коджабай, Оценяване на методите и условията на сушене според кинетиката, качествата на цветовете и специфичната енергия на сушене на тънки слоеве от тиква | 491 |
| Ж.-Л. Яо, И.-П. Пей, Ж.-И. Луо, Р.-Х. Ху, И.-С. Яанг, Уен-Тонг Чен, Приготвяне, охарактеризиране и флуоресценция на две кадмиеви съединения с различни разгънати структури | 496 |
| У. Аббас, Х. Али Атия, М.А.М. Абдийн, Отклонения от закона на дарси при ненютонови бингамови флуиди с топлопренасяне между две успоредни плоскости | 505 |
| Т. Махмуд, Дж. Ахмед, А. Шахзад, Р. Али, З. Икбал, Конвективно топлопренасяне във вискозен флуид над разтегнат лист, поставен в термично еднородна среда..... | 513 |
| Е. А. Велчева, З. И. Главчева, Б. А. Стамболийска, ИЧ спектрални и структурни промени причинени от превръщането на ацетанилида в азанион | 520 |
| А.И. Гизбрехт, М.М. Асимов, Кинетика на лазерно-индуцираната фотодисоциация на оксигемоглобина в кръвта за биомедицински приложения | 524 |

| | |
|--|-----|
| <i>А. Мираби, М.Р. Джамали, К. Каземи</i> , Определяне на следи от манган във водни проби чрез пламъкова атомно-абсорбционна спектрофотометрия след дисперсионна течно-течна микро-екстракция | 531 |
| <i>К.-У. Чанг, Дж. Ли, Ц.-С. Ян, Дж. Джуанг, Дж.-Л. Чен, К.-С. Йе, Дж. Ю, У.-П. Лю</i> , Нов метод за синтеза и фото-физични свойства на $\text{Ir}(\text{C}^{\wedge}\text{N})_3$ циклометалирани иридиеви фосфоресцентни комплекси..... | 534 |
| <i>З. Янг, И.Г. Уанг, И.Дж. Джинг, К.У. Уей, Ф.Ф. Ленг, Х. Ма, И.Л. Уанг, Дж. Кс. Чен</i> , Модифициране на шлюпки от фъстъци и тяхното приложение за адсорбция на тежки метали | 542 |
| <i>У. Гао, У.Ф. Уанг, М.К. Джамил, Р. Фарук, М.Р. Фарахани</i> , Обобщен анализ на свързаната атомна връзка с няколко молекулни графи | 549 |
| <i>У.Л. Ксу, И.Н. Янг, Дж. Уанг, М. Танг, И. Джуан, С.Дж. Пей</i> , Отстраняване на органична материя и механизъм на действие на системата за бърза инфилтрация..... | 557 |
| <i>И.В. Хуанг, К. Кю, К.И. Ню, Х.К. Гао, К. Хуанг, С.С. Ту</i> , Свойства, синтеза и отстраняване на ванадий от феро-манганови композитни материали | 564 |
| <i>М.У. Муцак, М. Имран, С. Башир, Ф. Канвал, Л. Миту</i> , Синтеза, структурни и биологични изследвания на наночастици от кобалтови ферити | 570 |
| <i>Б. Ерен, Й.Й. Гуркан</i> , Най-стабилните преходни състояния на молекулата на аминок-толуена | 579 |
| ИНСТРУКЦИЯ ЗА АВТОРИТЕ | 580 |